# POLITECNICO DI MILANO

Faculty of Information Engineering

Laurea Magistrale (MSc) in Electronics Engineering

## Development of Integrated Optical Components for a Quantum Teleportation Experiment

*Supervisor:*     **Dr. Roberto Osellame**
*Co-supervisor:*  **Dr. Andrea Crespi**

*Thesis of:*
**Farid Samara**
**Student ID: 801572**

*Academic Year 2015/16*

*"Poets say science takes away from the beauty of the stars - mere globs of gas atoms. I, too, can see the stars on a desert night, and feel them. But do I see less or more? " by Richard P. Feynman*

# Abstract

Quantum teleportation is a quantum communication protocol that can perform the reliable transfer of quantum information using a classical communication channel. An integrated optics circuit for quantum teleportation is advantageous in terms of footprint and components stability. Consequently, an on-chip quantum teleportation experiment will give a clear proof of the potentiality of such protocol. This thesis deals with the development of integrated optics components to manipulate polarisation entangled photons at the telecom wavelength, in order to build the sender unit in a quantum teleportation protocol. Using the femtosecond laser micromachining technique, a Polarising Beam Splitter (PBS) with extinction ratio up to 29 dB, and proper behaviour in a $\Delta\lambda = 15$ nm wavelength range was developed. A polarisation insensitive beam splitter was also developed. The polarisation insensitive beam splitters were based on a new two-dimensional geometry, and they demonstrated an excellent insensitivity to any arbitrary light polarisation. A combination of the above components, integrated on the same glass chip, constituted the core of one of the two nodes in the teleportation protocol. In addition, a path-encoded state preparation chip was developed using a thermally reconfigurable Mach-Zehnder interferometer. Simulations of the single-photons experiment were performed by considering the effect of components non-idealities on the quantum teleportation fidelity.

# Sommario

La teoria dell'informazione quantistica (quantum information) è una moderna area di ricerca interdisciplinare. Il suo obiettivo è quello di combinare i principi della fisica quantistica con quelli della teoria dell'informazione al fine di rendere affrontabili compiti che sarebbero insolvibili nei limiti dettati dalla teoria classica dell'informazione. Una caratteristica interessante della teoria quantistica dell'informazione è la sua duplice natura: da un lato è orientata alla profonda comprensione dei concetti fisici fondamentali e teorici, dall'altro si volge nella direzione delle applicazioni più propriamente tecnologiche che potrebbero portare a nuove forme di comunicazione e calcolo. Gli sviluppi del campo nascente della teoria quantistica dell'informazione autorizzano ad un ripensamento dei vari aspetti della teoria dell'informazione classica e all'invenzione di nuovi paradigmi. Un esempio di tali aspetti è l'effettivo trasferimento di informazione quantistica attraverso un classico canale di comunicazione con il protocollo del cosiddetto teletrasporto quantistico.

Il teletrasporto quantistico è un protocollo di comunicazione quantistica nato nel 1993 in seguito al lavoro di Bennet et al. [1]. Tale protocollo si basa sul fenomeno dell'entanglement quantistico per trasmettere l'unità fondamentale di informazione quantistica, il qubit o quantum bit, tra due punti distanti senza uno scambio diretto di sistemi quantistici tra mittente e destinatario. L'importanza di ciò risiede nel fatto che il qubit è considerata una entità delicata, facilmente alterabile o cancellabile durante la trasmissione. Alla formulazione teorica del teletrasporto quantistico del 1993 seguirono una serie di dimostrazioni sperimentali che portarono all'effettiva comunicazione tra due punti con distanze fino a 143 Km [2]. La gran parte degli esperimenti sul teletrasporto quantistico, seppur interessanti dal punto di vista della dimostrazione di principio, sono stati effet-

tuati con componenti ottici bulk, con evidenti svantaggi in termini di footprint e stabilità. Lo scopo del lavoro di tesi è lo sviluppo di componenti ottici integrati per il controllo della polarizzazione di fotoni entagled a lunghezze d'onda tipiche delle telecomunicazioni. Questi componenti andranno a formare l'unità del mittente nel protocollo di teletrasporto quantistico.

Per raggiungere questo obiettivo abbiamo utilizzato tecniche di microfabbricazione con laser a femtosecondi. Questa tecnica si è dimostrata molto efficiente per lo sviluppo e la fabbricazione di componenti ottici innovativi per applicazioni quantistiche poichè permette di inscrivere delle guide d'onda ad alta qualità in substrati vetrosi in una maniera diretta ed economica, senza l'impegno di maschere fotolitografiche. Tali caratteristiche rendono questa tecnica ideale per il prototipo di circuiti con un innovativo design tridimensionale.

# Contents

# List of Figures

# List of Tables

# Introduction

Quantum information has emerged as a relatively modern area of interdisciplinary study. It aims at combining the principles of quantum physics with those of information theory for the sake of rendering tractable some important tasks that were thought intractable under the constraints of classical information theory. An attractive feature of quantum information is that it is oriented towards two main directions at the same time, namely, toward a deeper understanding of fundamental physical concepts and theories, and, at the same time, toward real-world applications that may lead to new forms of communication and computation. The advancement of the infant field of quantum information entitles a rethinking of various aspects of information theory and the invention of new ones. An example of such aspects is the reliable transfer of quantum information using a classical communication channel which can be addressed by the so-called Quantum Teleportation protocol.

Quantum teleportation is a quantum communication protocol that was proposed in 1993 by Bennet et al. [1]. It relies on the phenomenon of quantum entanglement in order to transmit quantum information's basic unit of information; i.e. the qubit, between two points without any direct qubit exchange between the sender and the receiver. This is important because a qubit is considered a fragile entity that can be easily altered or destroyed during its transmission. Quantum teleportation theoretical formulation in 1993 was followed by a series of experimental demonstrations achieving quantum communication between distances up to 143 Km [2]. Most of the quantum teleportation experiments, although interesting from a proof-of-principle point of view, where done with bulk optics which meant clear disadvantages in term of footprint and components stability. Our aim in this thesis is to develop integrated optics components to manipulate polarisa-

tion entangled photons at the telecom wavelength, in order to build the sender unit in a quantum teleportation protocol.

To achieve our aim, we employ the femtosecond laser micromachining technique. Such technique has demonstrated to be extremely powerful for the design and the development of innovative optical circuits for quantum applications. In fact, it permits to inscribe high-quality optical waveguides in glass substrates in a direct and cost effective fashion, with no need for photolithographic masks, ideal for the prototyping of circuits with an innovative three-dimensional design.

This thesis is structured in the following way: Chapter 1 introduces some basic concepts in quantum optics together with the quantum teleportation scheme. Chapter 2 is dedicated to basic concepts in integrated optics and the femtosecond laser micromachining fabrication technique. Chapter 3 describes our experimental setup. Theoretical matters regarding our on-chip quantum teleportation experiment are discussed in Chapter 4, while the development and fabrication of the components are described in Chapter 5 and 6.

# Chapter 1

# Quantum optics

## 1.1 Quantum information

Quantum Information Science (QIS) shares the same aim of Classical Information Science (CIS), i.e. the study of acquisition, storage, transmission and processing of information, with the sole difference that QIS does so by relying on the laws of quantum mechanics. In QIS new features do emerge which have no classical counterpart. This fact is not surprising since the underlying theory of QIS represents a more accurate description of the world compared to classical mechanics. By exploiting those new features, not only we can improve the performances of already existing classical information chores, but also to conceive new ones which are not possible in the classical view.

Quantum effects are inevitable in the modern nanoscale classical devices; Indeed, device engineers do take them into account and even use them in designing new ones (e.g. Flash Memories which uses the quantum tunnelling effect in their operational principle). Nevertheless, information at the input and output of those devices can be considered classical, i.e. at a certain time, each input and output have a certain deterministic value plus a stochastic part due to noise, as required by classical physics. QIS instead requires a new set of devices in which the classical approximation would fail, and quantum nature of the information must be considered.

In the following, a brief explanation is given for some fundamental topics es-

sential to QIS, namely quantum superposition, the qubit, quantum entanglement, indistinguishability, Bell states and Bell-state measurement. A brief review of QIS applications is also given.

### 1.1.1 Quantum superposition

The superposition principle lies at the heart of QIS. The prime example of quantum superposition is the double slit experiment [1], consisting of a single-particle [2] source, a double-slit and an observation screen as in Figure 1.1. The astonishing result is that if the experimenter has no way to know which slit did the particle go through, then an interference pattern is observed. This behaviour is in contradiction with the intuitive view of how a particle should behave, and can be explained only if a wave-like nature is attributed to the particle. Quantum mechanics finds a solution to the problem by associating a wavefunction that represents the probability amplitudes for the event of the particle going through one slit or the other. The interference pattern on the screen can be explained by the interference between the two probability amplitude wave functions:

$$\Psi(X) = \frac{1}{\sqrt{2}}(\Psi_1(X) + \Psi_2(X)), \tag{1.1}$$

where the probability amplitude of finding the particle at some position $X$ when both slits are present is $\Psi(X)$, and when only slit 1 or 2 is present is $\Psi_1(X)$ and $\Psi_2(X)$ respectively. The interference pattern is obtained when the probability density $P_{12}(X)$ of finding the particle at some position $X$ is calculated:

$$P_{12}(X) = |\Psi(X)|^2 = \frac{1}{2}|\Psi_1(X) + \Psi_2(X)|^2. \tag{1.2}$$

Another astonishing result is that if the experimenter has a way to know which slit did the particle choose, then the interference pattern is destroyed.

---

[1] Richard Feynman said that the interferometric behaviour in such experiment, "In reality. . . contains the only mystery" of quantum mechanics and "We cannot make the mystery go away by 'explaining' how it works. We will just tell you how it works. In telling you how it works, we will have told you about the basic peculiarities of all quantum mechanics" [3].

[2] Double-slit experiment has been implemented with many kinds of particles, including photons, electrons, neutrons and atoms.
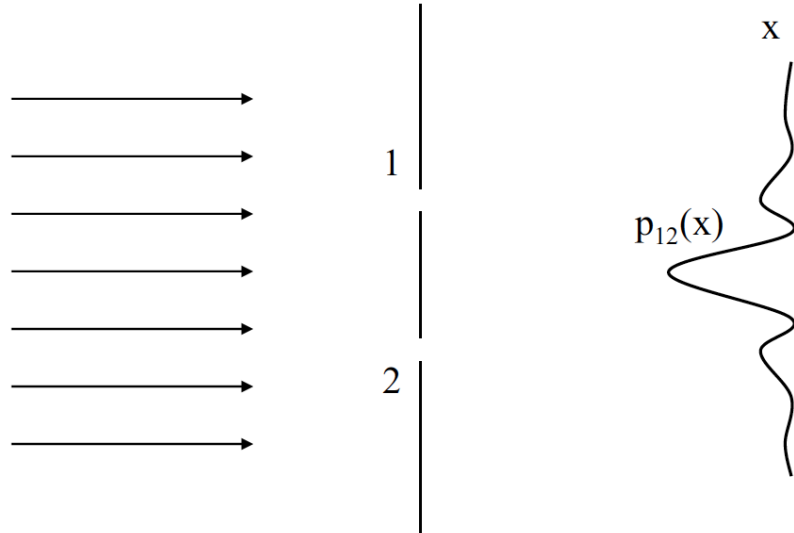
Figure 1.1: The double-slit experiment, represented by the passage of a particle through slit 1 and/or slit 2, followed by detection at points $X$ with single-particle interference on a screen. The interference pattern represents the probability density $P_{12}(X)$ of finding the particle at some position $X$.

This happens because in this case the experimenter would be observing $P_1(X) = |\Psi_1(X)|^2$ and $P_2(X) = |\Psi_2(X)|^2$, where $P_1(X)$ and $P_2(X)$ is the probability density of finding the particle at some position $X$ knowing that it went through slit 1 or 2 respectively. Quantum mechanics explains this by stating that if any apparatus is used, no matter how well-designed this apparatus is, it will inevitably interact with the wavefunction $\Psi(X)$ forcing it to "collapse" in $\Psi_1(X)$ or $\Psi_2(X)$ state.

## 1.1.2 The Bit and Qubit

The basic unit of information in CIS is the bit. The term bit is a portmanteau word which comes from binary digit. Hence, a bit can assume only two logical values which are represented by 0 and 1.

In QIS, the basic unit of information is the qubit. A qubit, like the bit, is a two-state system where the two states are called $|0\rangle$ and $|1\rangle$. To implement the

qubit, any quantum system which has at least two states can be used. The most peculiar property of the qubit is that it can exist in a quantum superposition state, indeed a general qubit state is represented by:

$$|Qubit\rangle = \alpha |0\rangle + \beta |1\rangle, \tag{1.3}$$

where $|\alpha|^2 + |\beta|^2 = 1$, and $\alpha$ and $\beta$ are the probability amplitudes of finding the qubit in the $|0\rangle$ and $|1\rangle$ state respectively. Note that Eq. 1.3 does not say that the qubit can assume any value between $|0\rangle$ and $|1\rangle$. Indeed, if measured, the qubit will collapse in the state $|0\rangle$ or $|1\rangle$ with the following probabilities:

$$P("\,|0\rangle\,") = |\alpha|^2, \quad P("\,|1\rangle\,") = |\beta|^2. \tag{1.4}$$

In fact, upon measurement, the bit and the qubit behave in the same way, i.e. the outcome of the measurement can only be one of the two possible values 1 or 0. However, while the bit had a certain value also before the measurement; the question of which value did the qubit have before the measurement does not make any sense as a result of quantum superposition.

This quantum superposition property can be harnessed to make tractable some important computational tasks that are thought intractable under the constraints of computing realised in systems describable by classical physics. In fact, the introduction of the qubit is justified by the existence of a few quantum algorithms that uses the qubit to perform some specific tasks much more efficiently than any known classical algorithm.

### 1.1.3 Quantum entanglement

Quantum entanglement is one of the most counter-intuitive aspects of quantum mechanics. It came to light in 1935 by a paper published by Einstein, Podolsky and Rosen commonly known as the EPR paper [4]. The entanglement of two (or more) quantum mechanical objects (e.g. two or more particles, two or more different degrees of freedom of the same particle, etc.) describes situations where the states of these systems exhibit quantum correlations such that they must necessarily be described with reference to each other, even though they can be in

different locations. Formally, a multi-particle system is in an entangled state, if the state of the entire system can not be written as the product of the individual particle states. To explain better the idea, we take the following state as an example:

$$|\psi\rangle = \frac{1}{\sqrt{2}}(|1\rangle_1 |1\rangle_2 + |0\rangle_1 |0\rangle_2), \qquad (1.5)$$

where the subscripts 1 and 2 refer to two different qubits. This system is an example of an entangled state since it can not be factorised into the product of two states one with the subscript 1 and another with the subscript 2. If we measure $|1\rangle$ for one qubit, this implies that we will measure $|1\rangle$ also for the second qubit. This is not due to a normal *classical correlation*, indeed Eq. 1.5 does not say that a certain source has generated the two qubits in the same state, where due to lack of knowledge about the inner mechanism of the source, we do not know if they were generated in the $|1\rangle_1 |1\rangle_2$ or $|0\rangle_1 |0\rangle_2$ state. Instead, and as experimentally confirmed in many experiments, the right way to interpret Eq. 1.5 is to say that the two qubits were generated in a particular state such that they have not decided yet if they both want to be $|1\rangle$ or $|0\rangle$, the decision is taken only upon measurement. If we measure only one qubit, it will collapse in a certain state, consequently, also the other qubit will instantaneously collapse in the same state, even if we have not measured it yet. This interpretation implies an even stronger kind of correlation, the *quantum non-local correlation*, where the non-locality [3] is due to the fact that the particles influence one the other even if they are not found inside the same light cone.

### 1.1.4 Indistinguishability

As the name suggests, two particles are called indistinguishable if they can not be distinguished one from the other on all degrees of freedom, such as energy, momentum and arrival time, or in other words, if they have the same set of quantum numbers. A system of two particles labelled 1 and 2, is described by the wavefunction $\Psi_{12}$. Exchanging (swapping) the two particles the wavefunction becomes $\Psi_{21}$. If the two particles are indistinguishable, then, apart from the sign,

---

[3]This interpretation has baffled Einstein who famously called the phenomena "the spooky action at a distance".

the wavefunction does not change under the exchange operation. However, two cases must be considered; the first case is when $\Psi_{12} = \Psi_{21}$. In this case, the two indistinguishable particles are called to be in the *symmetric state*. All Bosons (such as photons) in a product, i.e. not entangled, state are also in a symmetric state. The second case is when $\Psi_{12} = -\Psi_{21}$. In this case, the two indistinguishable particles are called to be in the *antisymmetric state*. All Fermions (such as electrons) in a product state are also in an antisymmetric state.

A way to verify the indistinguishability of two photons is to use a beam splitter. Indeed, beam splitters behave remarkably different if they are treated classically or with quantum mechanics. For instance, if two indistinguishable photons in a symmetric (antisymmetric) state are incident on the two inputs of a balanced beam splitter (i.e. with 50/50 splitting ratio) then quantum mechanics predict that these two photons will always emerge on the same (different) output (outputs) as illustrates in Figure 1.2. The reason for this behaviour is because the possibility for each photon to emerge on a certain output of the beam splitter is given by a probability amplitude. The probability amplitudes of the two photons can interfere constructively or destructively on the beam splitter, leading to enhancement or cancelling of the possibility of emerging on a certain output [5].

### 1.1.5 The Bell states and Bell-state measurement

**The Bell states** The Bell states are an important concept in quantum information theory. They are named after John S. Bell because they were used in his famous Bell inequality [6]. The Bell states represent the most simple example of entanglement states. They are four maximally entangled two-qubit system states which are very useful for quantum information science since they form a complete
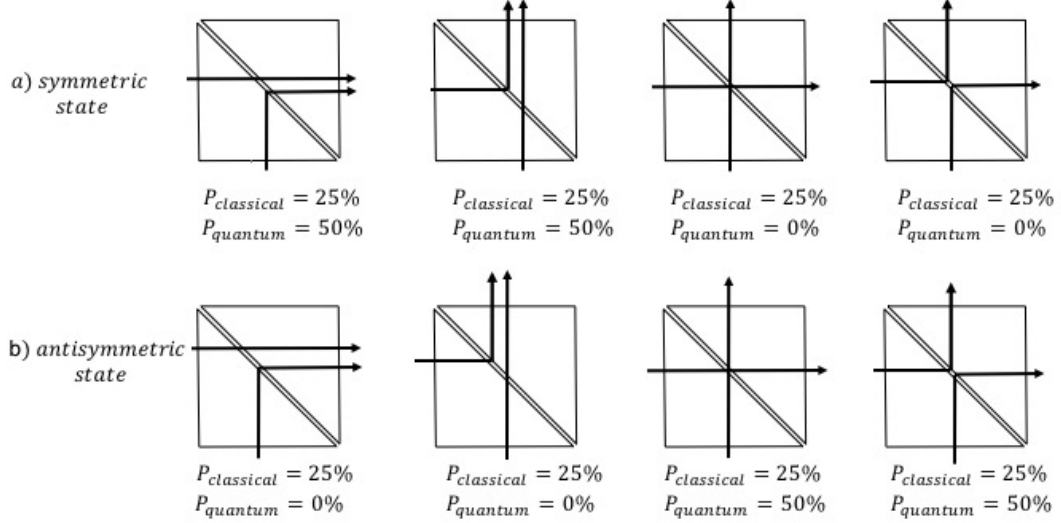
Figure 1.2: Two indistinguishable photons in a symmetric (a) and antisymmetric (b) state incident on a balanced beam splitter. The arrows represent the photon paths. The probability of each event to happen is given for the case where the beam splitter is treated classically $P_{classical}$, or quantum mechanically $P_{quantum}$.

and convenient basis for any two-qubit system. The four Bell states are:

$$
\begin{aligned}
|\Phi^+\rangle &= \frac{1}{\sqrt{2}} \big( |0\rangle_1 |0\rangle_2 + |1\rangle_1 |1\rangle_2 \big), \\
|\Phi^-\rangle &= \frac{1}{\sqrt{2}} \big( |0\rangle_1 |0\rangle_2 - |1\rangle_1 |1\rangle_2 \big), \\
|\Psi^+\rangle &= \frac{1}{\sqrt{2}} \big( |0\rangle_1 |1\rangle_2 + |1\rangle_1 |0\rangle_2 \big), \\
|\Psi^-\rangle &= \frac{1}{\sqrt{2}} \big( |0\rangle_1 |1\rangle_2 - |1\rangle_1 |0\rangle_2 \big).
\end{aligned}
\tag{1.6}
$$

**The Bell-state measurement**   Bell-State Measurement (BSM) is another important concept in quantum information science. A BSM is a joint measurement on a two-qubit system to determine in which Bell state the qubits are in. If the qubits were not in any of the four Bell states, then they get projected on one of the Bell states. Since Bell states are entangled states, the BSM is an entangling operation.

### 1.1.6 Quantum information sub-branches

QIS uses the principles of quantum mechanics not only to permit the experimental verification of fundamental principles of the quantum world, but also to produce new and useful applications in several fields. Quantum information technologies includes several sub-branches such as quantum computing, quantum cryptography, quantum sensing, quantum simulation, quantum metrology and quantum imaging.

**Quantum simulation and computing** In 1982 Richard Feynman [7] has debated that certain problems are easier to run on a computer that runs according to quantum mechanical principles rather than classical mechanical ones. This is especially true for complex quantum mechanical simulation problem. For instance, if certain quantum mechanical system consisting from N interacting spins needs to be simulated, it would require the simulation of vectors of $2^N$ dimensions; any additional spin added to the problem would imply an exponential increase in the complexity of the problem. If on the other hand, the problem is simulated on a quantum computer with N interacting qubits and an appropriate algorithm, then the simulation would require only one run to complete, significantly outperforming any classical computer. In this way, quantum computers can be described as complex quantum interferometric devices that can rely on quantum superposition principle to provide a unique sort of parallelism.

The superposition principle and the non-local correlations that arise from entanglement have been exploited as key ingredients in the theoretical development of algorithms that allow solving several computational problems more efficiently than any classical algorithm [8]. The two most notable examples are the Shor's algorithm for the factorisation of integers in prime numbers [9], and Grover's algorithm for searching an item in an unstructured database [10].

**Quantum communication** The aim of quantum communication is the reliable transfer of arbitrary quantum states between a sender, usually named Alice, and a receiver, Bob. This leads to various applications, such as the emerging technology of quantum key distribution (quantum cryptography) that permits secure communications which are protected by fundamental physical laws, rather than

relying on hard to solve computational problems like today's classical key distribution (classical cryptography) [11]. The idea on which quantum cryptography is based is that an intrusion in a quantum communication link by an eavesdropper would result in alteration of the qubit state. Measuring the error rate of the data transmission, the sender and the receiver can always detect the presence or absence of an eavesdropping [12].

Other applications of quantum communication are considered futuristic, such as the connection of spatially separated quantum computers for distributed quantum computing and a kind of quantum internet [13]. Quantum communication is also important at the microscopic distances; for instances, it would permit the connection of several quantum processors achieving a higher computing capability [14].

The transmission of the qubit over a certain channel is much more a challenging task than that of the classical bits. The main reasons for this are two. First, due to qubit decoherence; i.e. qubits state rapidly degrades by interacting with the environment, resulting in lower data transmission fidelity. Second, quantum mechanics prohibits the copying of a generic unknown qubit state; this is formalised in the so-called *quantum no-cloning theorem* [15].

## 1.2 Quantum teleportation

Quantum teleportation is a protocol that relies on the quantum non-locality concept (see Section 1.1.3) to transmit an unknown qubit state from Alice to Bob without having them directly exchanging any quantum information.

The word teleportation comes from science fiction, and it means an instantaneous transportation across space. However, this is not what we are dealing with here. Indeed, Einstein theory of relativity teaches us that superluminal signalling is prohibited; consequently, no instant transport of matter or information can happen. The reason for the terminology that was invented by Bennet et al. in 1993 [1] is that their protocol resembles the science fiction concept in that it results in the disassembly of a qubit at one location and its later reconstruction at another distant location by relying on quantum entanglement.

In the following, first, the telecommunication problem that quantum telepor-

11

tation can address is presented in Section 1.2.1. The protocol is then described conceptually (Section 1.2.2) and mathematically (Section 1.2.3). Some complementary materials are provided in Section 1.1.5 and 1.2.4. Finally, experimental realisations of the of the teleportation protocol are presented in Section 1.2.5.

## 1.2.1 The problem

To better understand the problem let us imagine the following example: Alice has a quantum computer which has performed some calculation and produced the following qubit:

$$|\psi\rangle = \alpha |1\rangle + \beta |0\rangle . \tag{1.7}$$

She now wants to transmit this qubit to Bob. This obviously can be achieved by transmitting the qubit directly to Bob. However, this requires the establishment of a quantum channel between Alice and Bob, whereby quantum channel we mean any channel that does not destroy the qubit, or in other words, that can preserve the quantum coherence of the qubit [4]. While this is a valid solution, it has the disadvantage of relying on the fragile quantum channel in which the qubit state may be altered due to decoherence, or worst; the qubit carrier may be destroyed due to unavoidable losses across any real channel. In this case, the quantum computer needs to regenerate the qubit $|\psi\rangle$ by re-performing the calculation.

A more efficient way of qubit telecommunication need to be invented. An example of such solution may be to try transmitting the information encoded in the qubit by relying on a classical channel, such as a conventional internet or phone connection. Such a classical channel solution is not a trivial one, this because:

- Alice can not measure her qubit, obtaining all the encoded information that can then be communicated to Bob over a classical channel. Indeed, a quantum state can not be fully determined by measurement; when Alice tries to measure her qubit, she will get either $|1\rangle$ or $|0\rangle$ with $|\alpha|^2$ and $|\beta|^2$ probability respectively, and the information stored in the complex coefficients $\alpha$ and $\beta$ is lost forever.

---

[4]In the special case in which the qubits are implemented with photons, the quantum channel can be fibre optic or free space.

- It is not possible to enhance the communication by making several copies of the same qubit and successively transmitting all the copies, thus achieving a bigger probability of transmitting at least one copy successfully. This because the *quantum no-cloning theorem* which prohibits the possibility of copying a generic unknown qubit [15].

As anticipated above, a solution to the problem is given by the quantum teleportation protocol.

### 1.2.2 The concept

The idea was first proposed by Bennet et al. in 1993 [1]. Where a possible way to physically disassemble the information associated with a general unknown quantum state, and later reconstruct it at a different location from a classical component and a quantum one was shown. The unknown generic qubit can be encoded in any physical system. However, since this will be the case in this thesis, in the following, we will be referring to the special case where the qubit is implemented with a photon.

Figure 1.3 illustrate the required scheme for teleporting the generic unknown quantum state $|\psi\rangle$. Three photons are required, which are labelled from 1 to 3. Photon 1 is used to encode the state $|\psi\rangle$. Photos 2 and 3 are an entangled pair which can be in any of the four Bell states. The teleportation protocol proceeds by sending photon 1 and 2 to Alice, and photon 3 to Bob. Having shared the entangled pair (photon 2 and 3) a quantum non-local channel is established between Alice and Bob. The idea at this point is the following: Alice performs some sort of joint measurement on photon 1 and 2 which does not reveal any information about the photons individually. In particular, the measurement that Alice has to perform is a Bell-State Measurement (BSM) which was briefly introduced in Section 1.1.5. Once the BSM is done, Alice communicates the result of the measurement to Bob, who will apply a certain unitary operation $U$ on photon 3 accordingly depending on the BSM's result. The strong correlation between photon 1 and 2 will make photon 3 emerge exactly in the state in which photon 1 was at the beginning, i.e. the state $|\psi\rangle$, and the teleportation protocol is completed.
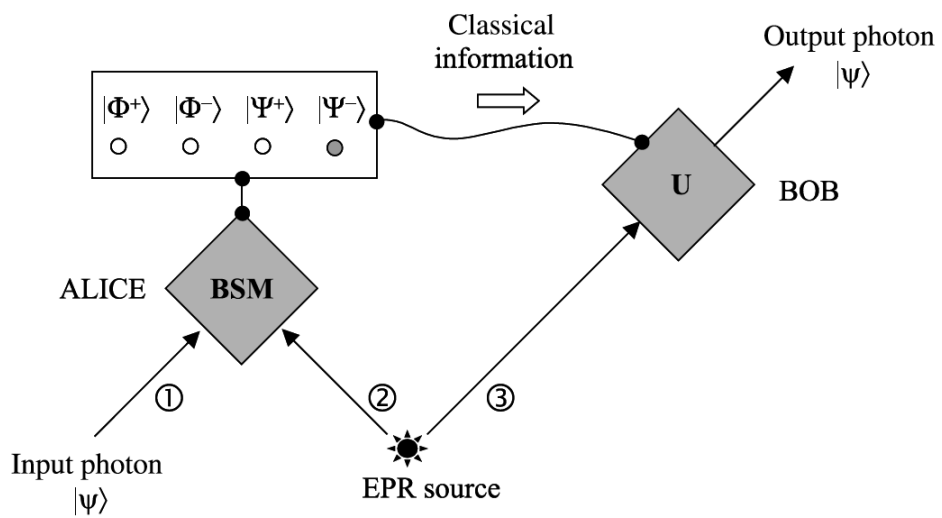
Figure 1.3: Schematic illustration of the concept of quantum teleportation implemented with photons. The qubit to be teleported $|\psi\rangle$ is encoded on photon 1. Photons 2 and 3 form a correlated pair in quantum entanglement state. Having received photon 1 and 2, Alice performs a Bell-State Measurement (BSM) on them and communicates the results to Bob over a classical channel. Depending on Alice's result, Bob performs a unitary transformation on photon 3 after which it emerges in the same quantum state $|\psi\rangle$ in which photon 1 was at the beginning [15].

The reason why the above protocol is possible and the state $|\psi\rangle$ is not lost may be described conceptually in the following way. As explained in Section 1.1.5, a BSM on photon 1 and 2 will also entangle them, but since photon 2 and 3 were generated in an entangled state themselves, it is then reasonable to think that photon 2 can function as an intermediary, through which photon 1 can influence photon 3 over the non-local channel. After the BSM, photon 1 get entangled with photon 2; thus it loses its identity, and the information about the quantum state $|\psi\rangle$ is temporary lost, or in other words, is decomposed into a quantum component which is transmitted to Bob over the non-local channel. Alice then informs Bob about her BSM result over a classical channel, therefore giving him an additional component, of a classical nature this time. In this way, the unknown quantum state $|\psi\rangle$ was disassembled into a quantum component and a classical one. Alone neither of these two components give any information about the quantum state $|\psi\rangle$, therefore the state is not lost, but when put together they determine the state $|\psi\rangle$ completely.

### 1.2.3 Mathematical description

Photon 1 carries the unknown qubit state $|\psi\rangle$ to be teleported, therefore we write:

$$|\psi\rangle_1 = \alpha \, |1\rangle_1 + \beta \, |0\rangle_1 \,, \tag{1.8}$$

where the subscripts indicate the label of the corresponding photon, while $|1\rangle$ and $|0\rangle$ refer to two states of a generic photon degree of freedom on which the qubit is encoded (e.g. the polarisation or the path of the photon). Photon 2 and 3 are in an entangled state; thus we write[5]:

$$|\Psi^-\rangle_{23} = \frac{1}{\sqrt{2}} \big( |0\rangle_2 \, |1\rangle_3 - |1\rangle_2 \, |0\rangle_3 \big). \tag{1.9}$$

The full state of the three photons is given by:

$$|\Psi\rangle_{123} = |\psi\rangle_1 \, |\Psi^-\rangle_{23} = \frac{1}{\sqrt{2}} \big( \alpha \, |1\rangle_1 + \beta \, |0\rangle_1 \big) \big( |0\rangle_2 \, |1\rangle_3 - |1\rangle_2 \, |0\rangle_3 \big). \tag{1.10}$$

---

[5]This is the entangled state that is typically used in an experiment with photons because it can be easily generated by type-II parametric down-conversion.

As discussed in Section 1.1.5, the four Bell states are a complete basis for any two-qubit state, so it is eligible to try to describe the combined state of photon 1 and 2 as a linear combination of the following four Bell states:

$$
\begin{aligned}
|\Phi^+\rangle_{12} &= \frac{1}{\sqrt{2}} \big( |0\rangle_1 |0\rangle_2 + |1\rangle_1 |1\rangle_2 \big), \\
|\Phi^-\rangle_{12} &= \frac{1}{\sqrt{2}} \big( |0\rangle_1 |0\rangle_2 - |1\rangle_1 |1\rangle_2 \big), \\
|\Psi^+\rangle_{12} &= \frac{1}{\sqrt{2}} \big( |0\rangle_1 |1\rangle_2 + |1\rangle_1 |0\rangle_2 \big), \\
|\Psi^-\rangle_{12} &= \frac{1}{\sqrt{2}} \big( |0\rangle_1 |1\rangle_2 - |1\rangle_1 |0\rangle_2 \big).
\end{aligned}
\tag{1.11}
$$

By elaborating Eq. 1.10 we can re-write it in the four Bell states basis given in Eq. 1.11:

$$
\begin{aligned}
|\Psi\rangle_{123} = \frac{1}{2} \Big( &|\mathbf{\Phi^+}\rangle_{\mathbf{12}} \big( \quad \alpha |1\rangle_3 - \beta |0\rangle_3 \big) \\
+ &|\mathbf{\Phi^-}\rangle_{\mathbf{12}} \big( \quad \alpha |1\rangle_3 + \beta |0\rangle_3 \big) \\
+ &|\mathbf{\Psi^+}\rangle_{\mathbf{12}} \big( -\alpha |0\rangle_3 + \beta |1\rangle_3 \big) \\
+ &|\mathbf{\Psi^-}\rangle_{\mathbf{12}} \big( -\alpha |0\rangle_3 - \beta |1\rangle_3 \big) \Big).
\end{aligned}
\tag{1.12}
$$

A BSM applied on a generic state $|\Psi\rangle_{123}$ will project it on one of the Bell states. From Eq. 1.11 one notes that a BSM forces $|\Psi\rangle_{123}$ to collapse without destroying the coefficients $\alpha$ and $\beta$ which are instantaneously transferred to photon 3 due to the strong quantum correlation between photon 2 and 3. Thus, for example, if the BSM at Alice's part produces the result $|\Psi^-\rangle_{12}$, this means that the total state $|\Psi\rangle_{123}$ collapses in:

$$
|\Psi\rangle_{123} \xrightarrow{BSM} |\Psi\rangle_3 = \big( -\alpha |0\rangle_3 - \beta |1\rangle_3 \big),
\tag{1.13}
$$

where the subscripts 1 and 2 have disappeared because photon 1 and 2 were destroyed upon the measurement, and what is left is photon 3 in the state given by Eq. 1.13. Although Bob does not know the state of his photon; namely photon 3, after receiving the classical information about the BSM result, he does

know which unitary transformation he needs to apply on his photon in order to get the required state; i.e. $\alpha \left|0\right\rangle_3 + \beta \left|1\right\rangle_3$. In the above example, this unitary transformation is the identity since the global phase does not count.

### 1.2.4 Important remarks

In the following we highlight some important remarks to clarify some eventual doubts that may arise from the above-described protocol:

- Alice needs to transfer her BSM result to Bob for the protocol to work. This is an important detail since it ensures that no information has been transferred faster than the speed of light.

- Photon 1, which initially encoded the qubit state $\left|\psi\right\rangle$, has been destroyed upon measurement; therefore, no two photons with the same unknown state $\left|\psi\right\rangle$ were created, which would be in contradiction with the quantum no-cloning theorem.

- Even though the creation of quantum channel between Alice and Bob was avoided, other two quantum channels for photon 2 and 3 were introduced. Thus, the actual utility of quantum teleportation as a telecommunication protocol may be questioned. The full potential of the above protocol as a telecommunication solution can be better appreciated if we think about a future network of quantum computers. In this situation, Alice and Bob are only two nodes of a big network of quantum computers, and the EPR source is a central server which is connected to all the nodes. In this way, all the nodes can be connected with each other using conventional classical channels, while quantum channels are established only between the nodes and the central server.

### 1.2.5 Experimental realisations

After the quantum teleportation proposal by Bennet et al. in 1993 [1], several experimental demonstrations were followed. In the following, we review the first two experimental demonstrations that were performed with photons. One of which

was based on Bennet's original three-photons scheme which was completed in 1997 by Bouwmeester et al. [16]. The other was based on a two-particle scheme which was proposed in 1995 by S. Popescu [17], and implemented in 1998 by Boschi et al. [18]. However, before discussing these experimental demonstrations, we first explain how to implement a BSM in the case of polarisation encoded qubits.

#### 1.2.5.1   Bell-state measurement with polarisation encoded qubits

The implementation of a BSM depends on how the qubit is realised. In the following we refer to the special case where the qubit is encoded over the polarisation degree of freedom of a photon; i.e. $|0\rangle$ and $|1\rangle$ are substituted by the vertical (V) and horizontal (H) polarisations. A key element in the polarisation encoded qubit case is the balanced Beam Splitter (BS). We start by observing that the four Bell states $|\Phi^{\pm}\rangle$, $|\Psi^{\pm}\rangle$ are a special case of non-product states; thus, we can not say that two indistinguishable photons in one of the four Bell states are also in a symmetric state just because photons are Bosons (see Section 1.1.4). To determine if such photons are in the symmetric or antisymmetric state, we need to apply the exchange operator. As seen by their definition in Eq. 1.6, the $|\Phi^{\pm}\rangle$ and $|\Psi^{+}\rangle$ are symmetric states because they do not acquire a minus sign if we exchange the subscripts 1 and 2; while $|\Psi^{-}\rangle$ is an antisymmetric state because it does acquire a minus sign under the exchange operator. Knowing this, we can predict the behaviour of the Bell states when impinged on a balanced BS. As seen in Figure 1.4, the two Bell states $|\Phi^{\pm}\rangle$ behaves exactly in the same manner; therefore, there is no way to distinguish between them. The Bell state $|\Psi^{+}\rangle$ behaves like $|\Phi^{\pm}\rangle$ because they are all symmetric states; however, they differ in the fact that in $|\Psi^{+}\rangle$ the two photons are always of an opposite polarisation while they are of the same polarisation in $|\Phi^{\pm}\rangle$. To distinguish $|\Psi^{+}\rangle$ from $|\Phi^{\pm}\rangle$, it is enough to put two polarising beam splitters (PBS) one each output of the normal beam splitter and observe if the photons emerge on different PBS outputs ($|\Psi^{+}\rangle$) or the same PBS output ($|\Phi^{\pm}\rangle$). Finally, the Bell state $|\Psi^{-}\rangle$ is easily distinguishable from all the other since only in this case the two photons emerge on different outputs of the balanced BS; indeed $|\Psi^{-}\rangle$ is the only antisymmetric Bell state.
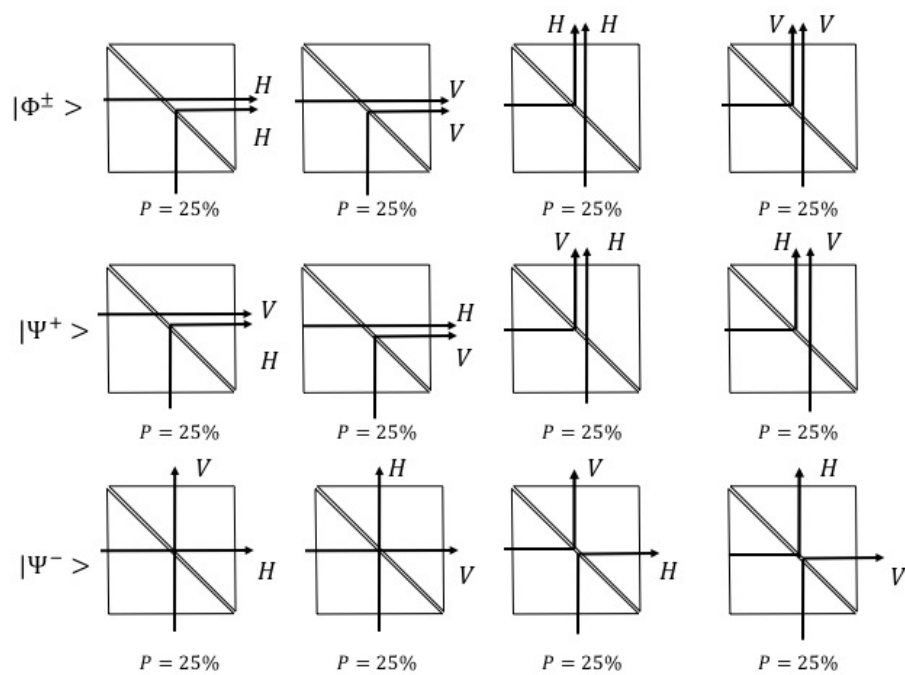
Figure 1.4: Two photons in a certain Bell state incident on a balanced beam splitter. The Bell states $|\Phi^\pm\rangle$ and $|\Psi^+\rangle_{12}$ are symmetric states, therefore the photons emerge on the same output. The Bell state $|\Psi^-\rangle_{12}$ is antisymmetric, and the photons emerge on different outputs.
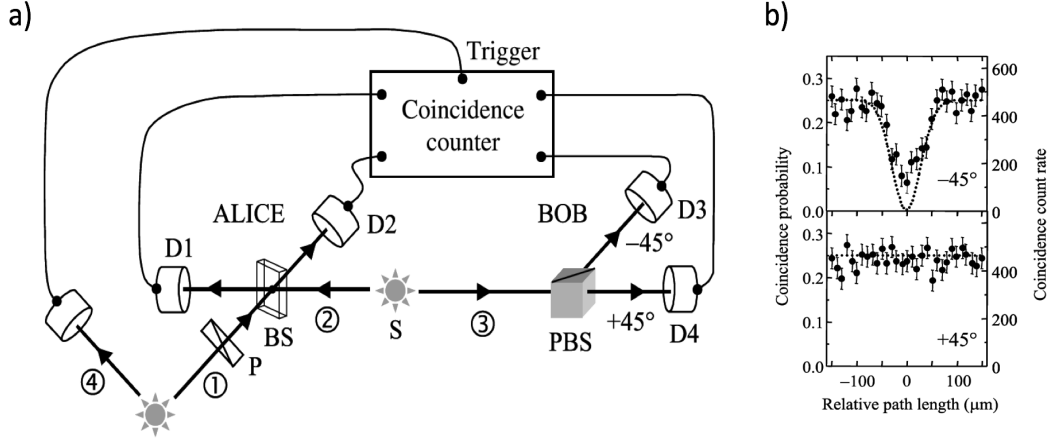
Figure 1.5: Schematic representation of Bouwmeester et al. experimental setup. Two pairs of photons are generated in two polarisation entangled states by two EPR sources. Photon 1 is the qubit encoder; its is prepared in the +45° or −45° state by a linear polariser (P). Photon 4 is used only to herald the arrival of photon 1. A beam splitter (BS) is used to perform a BSM: $|\Psi^-\rangle_{12}$ is detected when a both D1 and D2 photodetectors fire simultaneously, in this case, Bob checks if the teleportation was successful by analysing the polarisation state of photon 3 on a polarising beam splitter (PBS). (b) Experimental results for the case P= +45°. The upper graph indicates the D1D2D3 coincidence (−45°), while the lower graph indicates the D1D2D3 coincidence (+45°). Theoretical predictions are given by the dotted lines [16].

### 1.2.5.2 Original three-particle scheme

A schematic representation of Bouwmeester's experiment is given in Figure 1.5a, where the polarisation degree of freedom is used both for encoding the state to be teleported and to generate the entangled state.

As seen in Figure 1.5a, two EPR sources produce four photons by type-II parametric down-conversion. The first source simultaneously produces photon 1 and 4. Photon 1 was prepared in either the −45° or +45° state by a linear polariser P. While photon 4 was used only to herald the arrival of photon 1. The second source produces photon 2 and 3 in a quantum entanglement state.

To experimentally demonstrate that any unknown state can be teleported, first, one has to prove that the teleportation work for a complete set of states,

which serves as a set of known states onto which any other state can be decomposed [16]. A complete basis for the polarisation degree of freedom can be any two perpendicular linear polarisations. In this work, the $-45°$ and $+45°$ linear polarisation basis is chosen. Second, one has to show that teleportation works for superpositions of these base states [16]. Therefore the authors have also demonstrated teleportation for circular polarisation. Nevertheless, for the sake of the discussion in this section, we will refer only to the linear polarisations.

As seen in Section 1.1.5, only the Bell states $|\Psi^{\pm}\rangle_{12}$ can be identified, in particular, the $|\Psi^-\rangle_{12}$ can be easily identified by using only one beam splitter while $|\Psi^+\rangle_{12}$ identification requires additional two polarising beam splitters (PBSs). For simplicity, the authors decided to post-select only the cases in which $|\Psi^-\rangle_{12}$ is measured. This post-selection can be done by bringing both photon 1 and 2 on the beam splitter and looking for a coincidence detection on both photodetectors D1 and D2 placed at the output of the beam splitter.

As seen in Eq. 1.12, if Alice detects the $|\Psi^-\rangle_{12}$ Bell state, then Bob gets the state $(-\alpha|0\rangle_3 - \beta|1\rangle_3)$ which is equal to the state to be teleported apart from the global minus sign which does not count. Therefore, Bob part is rather easy; if Alice detects the $|\Psi^-\rangle_{12}$ Bell state, then Bob needs to do nothing. However, to experimentally demonstrate the successful teleportation, Bob needs to check the polarisation of his photon by using a PBS aligned with $\pm 45°$, and two photodetectors D3 and D4.

As mentioned in Section 1.1.5, the peculiar quantum interference on the beam splitter, and therefore the possibility to implement a quantum teleportation protocol, can be observed only if the two incident photons are indistinguishable. Where indistinguishability means that photon 1 and 2 need to arrive on the beam splitter at the same time or otherwise, they will behave classically, and no quantum teleportation can occur. This fact was verified experimentally by changing the relative path between photon 1 and 2 and observing the coincidence detection on D1D2. If the relative path is zero, the D1D2 coincidence happens with 25% probability, which corresponds to one Bell state out of four (the state $|\Psi^-\rangle_{12}$). While if the relative path is different from zero, no quantum interference can occur and the D1D2 coincidence happens with 50% probability (see Figure 1.2).

The experiment was done by setting P to $+45°$ or $-45°$ and looking at the

D1D2D4 and D1D2D3 coincidences. In the following, we refer to the particular case of P= +45°. If the relative path difference is zero, interference at the beam splitter occurs, and D1D2 coincidence happens with 25% probability. In this case, D4 and D3 click with 100% and 0% probability respectively making the overall D1D2D4 and D1D2D3 coincidence probability 25% and 0% respectively. If the relative path is different from zero, no interference can occur at the beam splitter, and the D1D2 coincidence happens with 50% probability, in this case, D4 and D3 click with 50% probability and the overall D1D2D4 and D1D2D3 coincidence probability is 25%. Therefore, theoretically, the D1D2D4 coincidence is always 25%, while the D1D2D3 is 25% when no teleportation occurs, but goes to 0% when the teleportation occurs. The experimental results are reported Figure 1.5b where the upper and lower graph refers to the D1D2D3 and D1D2D4 coincidence respectively, and the dotted line gives the theoretical prediction. Good agreement between theory and experiment was obtained with a dip visibility in the D1D2D3 coincidences of $0.64 \pm 0.02$.

### 1.2.5.3   Two-particle scheme

The original teleportation scheme as proposed by Bennet et al. involves three particles. A limitation of this scheme is that Alice can not perform a full Bell-state discrimination, which reduces the efficiency of quantum state teleportation. In this section, we describe a two-photon scheme which was proposed in 1995 by S. Popescu [17] and experimentally demonstrated in 1998 by Boschi et al. [18]. This scheme allows full Bell-state discrimination (100% efficiency of quantum state teleportation) but places a restriction on the quantum state that can be teleported.

In the original Bennet scheme, the first particle is initially in the state $|\Psi\rangle$, which Alice wants to transmit to Bob over a classical channel. One might think that this particle was given to Alice by a third party, the Preparer. The other two particles, one sent to Alice and one sent to Bob, are in an entangled state and constitute the non-local communication channel. In the two-photon scheme, on the other hand, only two photons are present (in an entangled state), but two degrees of freedom are exploited. The Prepared has to help Alice by encoding $|\Psi\rangle$
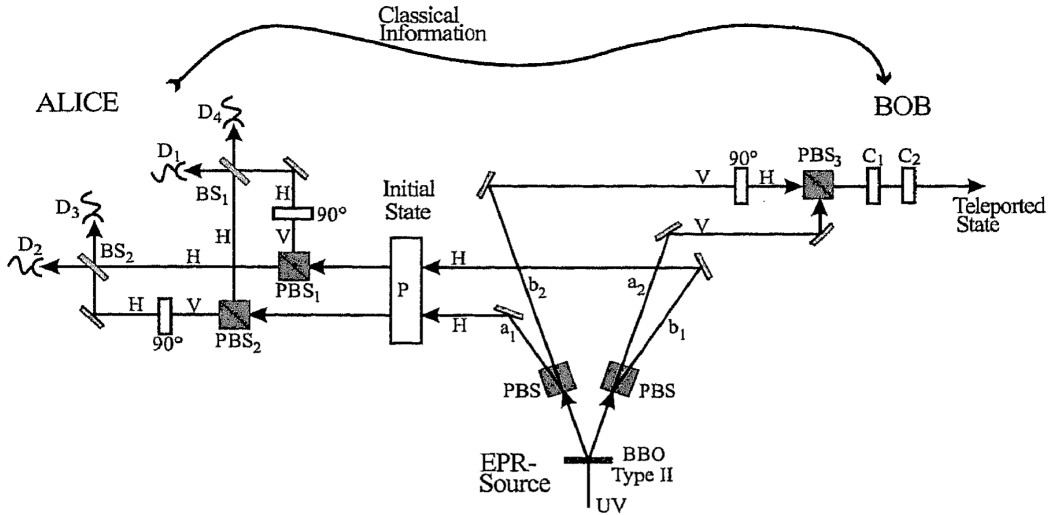
Figure 1.6: Experimental scheme for two-particle quantum teleportation protocol. The setup consists of a BBO crystal to generate two polarisation entangled photons by type-II parametric down-conversion. Polarising beam splitters (PBS). 50/50 beam splitters (BS). Single-photon detectors (D). Half waveplates (90°). The Preparer (P) of the initial quantum state, and polarisation transformers (C) [19].

directly into her member of the entangled pair instead of encoding it into a third particle. Thus, this scheme places a restriction on the teleported state which can not come to Alice directly from a third party, but must be encoded directly into her part of the entangled photon pair.

The problem facing Alice does not change; Alice has no way to find out the state $|\Psi\rangle$, so there is no way to transfer $|\Psi\rangle$ to Bob over a classical channel without the help of the quantum non-local channel (the entangled state) as in the original protocol.

Figure 1.6 describes the experimental scheme for two-particle quantum teleportation. The first step is to create a non-local channel between Alice and Bob by generating a pair of path entangled photons, but with a well-defined polarisation. To this purpose, a pair of polarisation entangled photons is produced by

type-II parametric down-conversion (EPR Source), therefore creating the state:

$$|\Psi^+\rangle_{12} = \frac{1}{\sqrt{2}}\big(\,|H\rangle_1\,|V\rangle_2 + |V\rangle_1\,|H\rangle_2\,\big). \tag{1.14}$$

The two photons pass through a polarising beam splitter (PBS) which transmits the vertical polarisation (V) and deflects the horizontal polarisation (H), leading to the transformation of the polarisation entanglement into path entanglement:

$$\frac{1}{\sqrt{2}}\big(\,|a_1\rangle\,|a_2\rangle + |b_1\rangle\,|b_2\rangle\,\big)\,|H\rangle_1\,|V\rangle_2\,, \tag{1.15}$$

where everything with the subscript 1 is related to Alice, and with the subscript 2 is related to Bob. The letters $a$ and $b$ indicates the two possible paths that both Alice and Bob can have. As seen by Eq. 1.15, Alice's photon is always H while Bob's photon is always V.

On its way to Alice, photon 1 encounters the Preparer (P), who creates an arbitrary quantum state by changing the photon polarisation from H to an arbitrary quantum superposition:

$$|\Psi\rangle_1 = \frac{1}{\sqrt{2}}\big(\alpha\,|H\rangle_1 + \beta\,|V\rangle_1\,\big). \tag{1.16}$$

This can be achieved by using polarisers that work in the same way on path $a$ and $b$. The state $|\Psi\rangle_1$ is the state that Alice wants to transmit to Bob.

Photon 1 is a part of an entangled pair; therefore the whole state of both photons must be considered:

$$|\Phi\rangle = \frac{1}{\sqrt{2}}\big(\,|a_1\rangle\,|a_2\rangle + |b_1\rangle\,|b_2\rangle\,\big)\,|\Psi\rangle_1\,|V\rangle_2\,, \tag{1.17}$$

which is the analogue for $|\Psi\rangle_{123}$ in the original scheme (Eq. 1.10). At this point, Alice performs a BSM on $|\Psi\rangle_1$ and her part of the path entangled pair. Here, we

can define the following Bell states:

$$
\begin{aligned}
|\Phi^+\rangle &= \frac{1}{\sqrt{2}}\big(\,|a_1\rangle\,|V\rangle_1 + |b_1\rangle\,|H\rangle_1\,\big), \\
|\Phi^-\rangle &= \frac{1}{\sqrt{2}}\big(\,|a_1\rangle\,|V\rangle_1 - |b_1\rangle\,|H\rangle_1\,\big), \\
|\Psi^+\rangle &= \frac{1}{\sqrt{2}}\big(\,|a_1\rangle\,|H\rangle_1 + |b_1\rangle\,|V\rangle_1\,\big), \\
|\Psi^-\rangle &= \frac{1}{\sqrt{2}}\big(\,|a_1\rangle\,|H\rangle_1 - |b_1\rangle\,|V\rangle_1\,\big).
\end{aligned}
\tag{1.18}
$$

Hence, the state $|\Phi\rangle$ can be rewritten using this Bell state basis:

$$
\begin{aligned}
|\Phi\rangle =\frac{1}{2}\Big(&|\boldsymbol{\Phi}^+\rangle\big(\beta\,|a_2\rangle + \alpha\,|b_2\rangle\,\big)\,|V\rangle_2 \\
&+ |\boldsymbol{\Phi}^-\rangle\big(\beta\,|a_2\rangle - \alpha\,|b_2\rangle\,\big)\,|V\rangle_2 \\
&+ |\boldsymbol{\Psi}^+\rangle\big(\alpha\,|a_2\rangle + \beta\,|b_2\rangle\,\big)\,|V\rangle_2 \\
&+ |\boldsymbol{\Psi}^-\rangle\big(\alpha\,|a_2\rangle - \beta\,|b_2\rangle\,\big)\,|V\rangle_2\Big).
\end{aligned}
\tag{1.19}
$$

To perform a BSM, Alice needs to entangle the path degree of freedom of photon 1 with its polarisation degree of freedom. This can be done by first splitting the H and V polarisation using a polarisation beam splitter in both path $a$ (PBS$_1$) and $b$ (PBS$_2$). Then the H polarisation coming from path $a_1$ ($b_1$) is made to interfere with the V polarisation coming from path $b_1$ ($a_1$) using the beam splitter BS$_1$ (BS$_2$), this is possible by turning the V into H using a 45° half waveplates. It can be shown, by propagating Eq. 1.18 through the PBS, HWP and BS, that in this way a photon detection by $D_1$, $D_2$, $D_3$, or $D_4$ corresponds directly to one of the four Bell states. Hence all the four Bell states can be distinguished, and 100% teleportation efficiency is made possible.

To complete the protocol, Alice needs to inform Bob about her BSM result (which detector has clicked) who needs to apply a unitary transformation to photon 2 to recover the state $|\Psi\rangle$. First, Bob transforms the path superposition of photon 2 into a polarisation superposition by using 45° half waveplate in path

$b_2$ and combining the two paths on a PBS (PBS$_3$). This will result in:

$$
\begin{aligned}
|\Phi\rangle = \frac{1}{2}\Big(&|\boldsymbol{\Phi}^+\rangle\big(\beta\,|V\rangle_2 + \alpha\,|H\rangle_2\big)\\
&+ |\boldsymbol{\Phi}^-\rangle\big(\beta\,|V\rangle_2 - \alpha\,|H\rangle_2\big)\\
&+ |\boldsymbol{\Psi}^+\rangle\big(\alpha\,|V\rangle_2 + \beta\,|H\rangle_2\big)\\
&+ |\boldsymbol{\Psi}^-\rangle\big(\alpha\,|V\rangle_2 - \beta\,|H\rangle_2\big)\Big).
\end{aligned}
\tag{1.20}
$$

Depending on Alice BSM result, Bob can finally reconstruct $|\Psi\rangle$ by using two optical elements $C_1$ and $C_2$ to rotate V into H or vice versa, and to apply a $\pi$ shift.

## 1.3  Integrated quantum photonics

The sub-brach of quantum technologies that uses photons to realise the quantum systems is called quantum photonics. Photons offer several degrees of freedom that can be used for qubit encoding, e.g. the polarisation, path, phase and angular momentum. The intrinsic physical characteristics of light make it the natural solution for today's long distance classical communication, likewise, photons would be the natural choice for tomorrow's long-distance quantum communications. Photons can be easily manipulated by standard bulk optics, and their detection can be performed rather efficiently over a wide wavelength range.

A typical photonics quantum circuit consists of several optical paths, mixed in a linear optical network composed of nested interferometers. A bulk optics implementation of such quantum circuits implies free space photon propagation and the use of mirrors and beam splitters to construct the optical circuits. Being based on interferometry these circuits require a sub-wavelength stability of optical path lengths. Additionally, high visibility quantum interference calls for an excellent mode overlap at the beam splitters [20]. Such path stability and mode overlap are hard to achieve in bulk optics, especially when numerous optical elements are involved, therefore imposing severe limitations on the complexity of the experiments that can be accomplished with this approach.

The above-mentioned drawbacks can be overcome with an integrated optics

approach. Indeed, integrated optics can realise monolithically integrated devices with advantageous in term of mechanical stability and the ability to control the phase of the light to an extent that is not possible with bulk elements. Spatial modes overlapping can be realised straightforwardly using directional couplers. Additionally, optical confinement in few micrometer-sized optical waveguide implies a significant field enhancement, therefore improving the non-linear interactions. This can be advantageous, for example, for the realisation of efficient integrated photon sources [21] or frequency converters [22].

First integrated quantum optics demonstration dates back to 2008 were high-fidelity silica-on-silicon integrated optical realisations of key quantum photonics circuits was demonstrated, including two-photon quantum interference, a controlled-NOT gate, and a path-entangled state of two photons [23]. Since then, much work has been done to bring integrated circuits closer to a point where their utilisation in quantum technologies, and ultimately commercialisation, can become a reality through further miniaturisation and development of high-performance components [24].

Although photonics experiments were the first to realise quantum teleportation, the demonstration of this protocol in integrated optics experiment is not trivial. Indeed the realisation of both three-photon and two-photon schemes is made difficult by the difficulty of realising three photonic qubits on a sufficiently complex circuit [25], and polarisation management difficulties respectively. Up to date, there is only one demonstration of integrated optics circuit for quantum teleportation, and it is due to Metcalf et al. [26]. Metcalf's experiment was based on the three-photon scheme. All the essential component for the protocol; i.e. state preparation, Bell-state measurement and a verification stage were monolithically integrated on one chip. The optical circuit was directly written with UV beam on a silica-on-silicon substrate. All the three qubits were path encoded. A generic path-encoded state was realised by using a thermally reconfigurable Mach-Zehnder interferometer. The non-idealities of the circuit were characterised using a classical light, and were taken into account in the verification process to maximise the teleportation fidelity. By teleporting three different states, the average teleportation fidelity obtained was $89\% \pm 3\%$, surpassing the average classical limit of $2/3$ by more than six standard deviations [27].

# Chapter 2

# Integrated Optics

The term integrated optics was first coined by S.E Miller in 1969 [28], with a clear inspiration from the well-developed field of micro-electronics. Miller has the idea of creating integrated optical circuits by using the planar integrated electronics lithographic process to fabricate basic optical components that are connected via optical lines called waveguides. In synthesis, with the sole difference of substituting electrons with photons, integrated optics tries to repeat the successful story of electronics, aiming at commercialisation by first achieving miniaturisation and cost reduction, which in turns will generate enough economic revenue to auto-sustain its innovative research.

In Section 2.1 we describe the most basic concepts and components in integrated optics. In Section 2.2 we introduce some conventional integrated optics lithographic technologies. Femtosecond Laser Micromachining (FLM) fabrication technique is presented in Section 2.3 since it is the technique used to fabricate all the waveguides that are used in this thesis. Finally, Section 2.4 is dedicated to polarisation handling in integrated optics since the polarisation degree of freedom plays a central part in our teleportation experiment.

## 2.1 Basic concepts and components

### 2.1.1 The dielectric optical waveguide

The term optical waveguide indicates any structure, typically made from dielectric material, that can confine and guide the electromagnetic radiation in the optical bandwidth. The most known example of dielectric optical waveguides is the optical fibre, typically used for high capacity data transfer. A cross-sectional view of several examples of integrated dielectric optical waveguides is provided in Figure 2.1. The concept behind these different waveguides is the same: a *core* with $n_w$ refractive index is surrounded by the *cladding* with $n_s$ refractive index, where $n_w > n_s$ must be satisfied to achieve a confining structure. For technological reasons, sometimes there is not one, but two cladding materials with two different refractive indexes $n_c$ and $n_w$. In this case, what is important is that these refractive indexes are both smaller than the core refractive index.
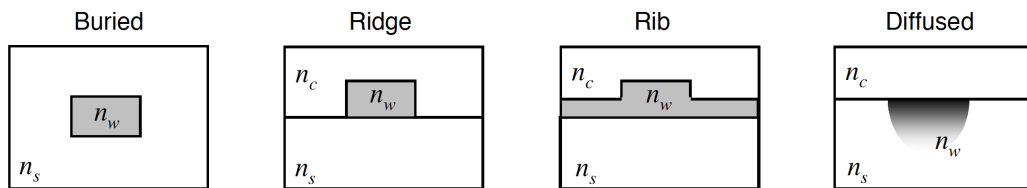


Figure 2.1: Cross-sectional view of several dielectric optical waveguide. $n_w$ is the refractive index of the core, while $n_c$ and $n_s$ are the refractive indexes of the cladding. $n_w > n_c, n_s$ must be satisfied in order to achieve a confining structure.

#### 2.1.1.1 Formal treatment of light propagation in optical waveguide

The proper and rigorous way to solve the guiding structure is to start from Maxwell equations, from which the wave equation can be derived. To make the problem more accessible, it is useful to introduce the following simplifications:

- *linearity*, i.e. the electric permittivity $\epsilon$ and magnetic permittivity $\mu$ does not depend on the field intensity.

- *isotropy*, i.e. the electric permittivity $\epsilon$ and magnetic permittivity $\mu$ does not depend on the field direction.

- *absence of sources*, i.e. no current or free charge in the material.

- *peacewise homogeneity*, i.e the waveguide cross-section is divided in homogeneous sub-regions. The wave equation is solved in each sub-region, and then the solutions are combined by applying the proper boundary conditions and the fields continuity on the interfaces.

- *z-invariant*, i.e the structure is homogeneous in the propagation direction, therefore the refractive index can be written as $n(x, y)$.

under the above simplifying hypothesis, the electric field can be written as:

$$\boldsymbol{\varepsilon}(x, y, z) = \mathbf{E}(x, y)e^{-j\beta z}, \tag{2.1}$$

where $\boldsymbol{\varepsilon}(x, y, z)$ is the electric field vector, $\beta$ is the propagation constant and $\mathbf{E}(x, y)$ is the electric field profile in the plane perpendicular to the propagation direction. The equation that governs the field propagation is recovered by substituting Eq. 2.1 in the wave equation, obtaining:

$$\bigtriangledown_t^2 \mathbf{E}(x, y) + [k_0^2 n^2(x, y) - \beta^2]\mathbf{E}(x, y) = 0, \tag{2.2}$$

where

$$\bigtriangledown_t^2 = (\partial^2/\partial x^2, \partial^2/\partial y^2, 0) \tag{2.3}$$

is the Laplacian operator and $k_0 = 2\pi/\lambda$ is the wavenumber. Eq. 2.2 is an eigenvalue equation; the values that $\beta$ can assume are the eigenvalues, and the associated field profiles $\mathbf{E}(x, y)$ are the eigensolutions. We call these eigensolutions the "modes" of the waveguide. Once the dielectric waveguide geometry is defined, i.e. the $n(x, y)$ profile, and the wavelength is fixed, Eq. 2.2 produces, in general, a number of solutions. In other words, the waveguide supports a number of modes, each with its field distribution $\mathbf{E}(x, y)$ and propagation constant $\beta$.

An analytical solution for Eq. 2.2 is, generally, not obtainable, but it is necessary to adopt numerical methods. It is also worth mentioning that an equation

similar to Eq. 2.2 can be written for the magnetic field **H**.

Depends on the waveguide properties, the modes can have field components purely transversal (TEM modes), only the electric field can be transversal (TE modes), only the magnetic field can be transversal (TM modes) or they can be hybrid modes with longitudinal component mainly magnetic (HM modes) or mainly electric (HE modes). In dielectric waveguides, the pure TE and TM modes do not exist, but only the hybrid modes. Nevertheless, because one of the longitudinal components is always much smaller than the other, the modes are given the names of quasi-TE and quasi-TM.

### 2.1.1.2 Mode properties

All the solutions of Eq. 2.2 are called modes; however, they can be divided into two categories: the guided modes and the radiative modes:

- The guided modes are those solutions that are confined in the waveguide, in other words, the mode profile $E(x, y)$ can be normalised, and it decays to zero far away from the core. The guided modes propagate without changing their shape nor their intensity (in an ideal lossless waveguide).

- The radiative modes are those solutions that are not spatially confined in the waveguide, but they have a transversal propagation component that progressively subtract power from the propagation component in the z direction.

In the following, we give the most important properties of the modes of a dielectric optical waveguide, keeping in mind that these properties are of a general nature and are valid for any guiding structure:

- The modes are orthogonal in space and time; therefore, no transfer of power can occur between any two modes. This orthogonality is also valid for the radiative modes.

- The propagation constant $\beta$ can also be written as $\beta = \frac{2\pi}{\lambda} n_{eff}$. Where $n_{eff}$ is called the effective refractive index and is the refractive index that is "seen" by the propagating mode.

31

- Each mode has its own speed of propagation given by $v_p = \omega/\beta$. where $\omega = c/n_{eff}$ is the angular frequency, and $c$ is the speed of light in vacuum.

- In a real waveguide, even in a non-absorbing material, the z-invariant condition is broken by the roughness of the waveguide. This causes a power scattering from the fundamental mode to the radiative modes or to other guided modes. Such scattering results in losses in the waveguide, which we call *propagation losses* PL. The PL can be modelled as $e^{-\alpha z}$, where $\alpha$ is called the *loss coefficient* and $z$ is the propagation direction.

### 2.1.2   Coupled mode theory

Power exchange occurs between waveguides that are brought sufficiently together. Describing this situation is crucial since it frequently occurs in integrated optics (see Section 2.1.3 and Section 2.1.4). Finding the analytical solution for every particular design is a tedious task, even the numerical approach may be heavy and time-consuming. However, generally, the size of the structure is on the order of several hundred or several thousands of wavelengths, which means that the fields evolve in a slow adiabatic way, and a perturbative approach may be applied. It is then possible to consider that, in every small section of the optical device, the modes are those of the unperturbed structure and to consider a perturbative part that couples the modes of the unperturbed structure, therefore accounting for the reciprocal influence of each waveguide on the other.

A complete treatment of coupled mode theory, can be easily found in the literature (e.g. [29]). In the following, we give directly the solution provided by coupled-mode theory for the structure that is reported in Figure 2.2. With $I_1$ and $I_2$ we indicate the complex amplitude of the input fields in the two waveguides of Figure 2.2, while with $O_1$ and $O_2$ we indicate the fields in their outputs, then:

$$\begin{bmatrix} O_1 \\ O_2 \end{bmatrix} = T_c \begin{bmatrix} I_1 \\ I_2 \end{bmatrix},$$

(2.4)

where $T_c$ is called the transmission matrix and is given by:

$$T_c = e^{-i\bar{\beta}z} \begin{bmatrix} \cos\delta z - iR\sin\delta z & -iS\sin\delta z \\ -iS\sin\delta z & \cos\delta z + iR\sin\delta z \end{bmatrix}, \qquad (2.5)$$

where $R = \frac{\Delta\beta}{2\delta}$, $S = \frac{k}{\delta}$, $\Delta\beta = \beta_1 - \beta_2$, $\bar{\beta} = \frac{\beta_1 + \beta_2}{2}$ and $\delta = \sqrt{\frac{\Delta\beta^2}{4} + k^2}$.
$\beta_1$ and $\beta_2$ are the propagation constants of the two waveguides when they are considered separately. The $R$ and $S$ coefficients measure the degree of asymmetry of the structure, in the special case of $\beta_1 = \beta_2$ they become $R = 0$ and $S = 1$. $k$ is called the *coupling coefficient*, it measures the degree of power coupling from one waveguide to the other. In the case of two identical waveguides, $k$ is given by the following overlap integral:

$$k = \frac{k_0^2}{2\beta} \frac{\int \int_{\infty}^{-\infty} E(x,y)(n^2(x,y))E(x,y)^* dxdy}{\int \int_{\infty}^{-\infty} E(x,y)E(x,y)^* dxdy}, \qquad (2.6)$$

where $E(x,y)$ is the single mode electric field profile of the unperturbed waveguides.

The transmission matrix given in Eq. 2.4 is an extremely powerful instrument for analysing and designing a wide variety of optical structures. Any general structure can be divided in small pieces of coupled waveguides like the ones depicted in Figure 2.2, to calculate the transfer function of the device, it is enough to cascade several transmission matrixes given by Eq. 2.5 and calculate the product.
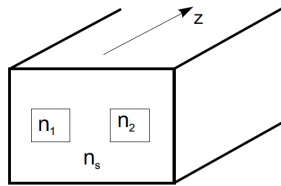


Figure 2.2: Coupled modes theory. An example of two waveguides that are brought close together in a way to reciprocally influence one the other.

### 2.1.3 The directional coupler
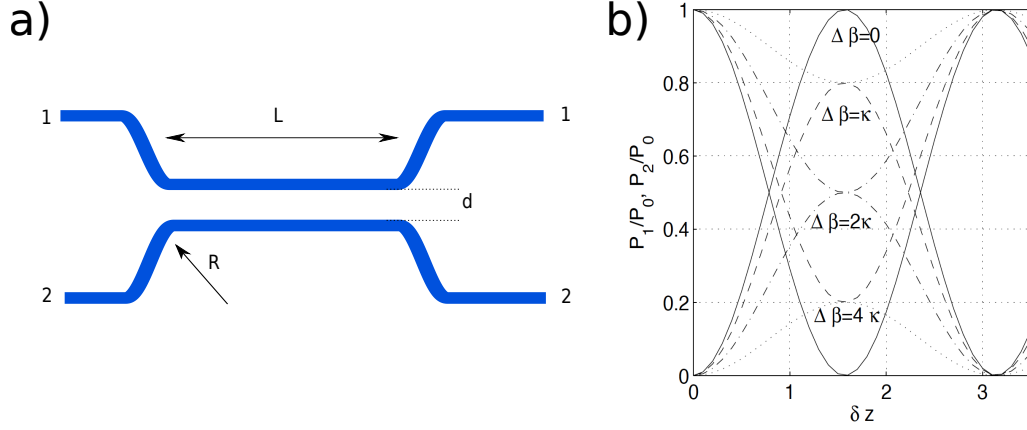


Figure 2.3: (a) Schematic representation of the directional coupler structure. Two waveguides 1 and 2 are brought close together by mean of an S-bend of radius R, resulting in two coupled straight waveguides with a length L and coupling distance d. (b) Asymmetric directional coupler behaviour. The curves with maxima (minima) in the middle represent the splitting ratio on the cross (bar) port.

A crucial component in integrated optics is the directional couplers, whose most typical design is shown in Figure 2.3a. It is the integrated optics analogue of the bulk beam splitter. A directional coupler has four ports, and it is made from two inputs and two outputs regions in which the waveguides are completely decoupled, while in the central part of length L the waveguides are brought close together achieving light transfer by evanescent field coupling. Usually, power is injected only in one of the two input ports, in this case, the output port of the same waveguide in which power was injected is termed *bar* or *reflection* port, while the other output is termed *cross* or *transmission* port.

The transmission matrix of the directional coupler can be obtained by dividing the structure in Figure 2.3a into small pieces, each of which is described by a transmission matrix like the one in Eq. 2.5, and making the product to obtain the overall transfer function of the device. Another easier approach is to consider the directional coupler only as two coupled straight waveguides like the ones in Figure 2.2, with a length $z = L + L_{eff}$, where L is the length of the two

straight waveguides in the coupling region and $L_{eff}$ is an empirical value that accounts for the bending effects. In this simple case, the transfer function of the directional coupler is exactly the one of Eq. 2.5. In the special case of two symmetric waveguides, i.e. $\Delta\beta = 0$, the transmission matrix is given by:

$$T_c = \begin{bmatrix} \cos(kz) & -i\sin(kz) \\ -i\sin(kz) & \cos(kz) \end{bmatrix}, \tag{2.7}$$

where the common phase factor was neglected. By entering with all the power $P_0$ on port 1, the periodical exchange of power between the two waveguides can be obtained by squaring Eq. 2.4:

$$
\begin{aligned}
P_1(z) &= P_0 \cos^2(kz), \\
P_2(z) &= P_0 \sin^2(kz),
\end{aligned}
\tag{2.8}
$$

where $P_1$ is the power on the bar, and $P_2$ is the power on the cross. In the general case of $\Delta\beta \neq 0$:

$$
\begin{aligned}
P_1(z) &= P_0(1 - \frac{k^2}{\delta^2}\sin^2(\delta z)), \\
P_2(z) &= P_0 \frac{k^2}{\delta^2}\sin^2(\delta z).
\end{aligned}
\tag{2.9}
$$

The splitting ratios of the directional coupler can be defined with the following notations:

$$R = Reflection = P_1/P_0, \tag{2.10}$$

$$T = Transmission = P_2/P_0. \tag{2.11}$$

Another interesting observation is the directional coupler behaviour when $\Delta\beta \neq 0$. From the general transfer function given by Eq. 2.5 it is easy to show that in this case the power/splitting-ratio on the cross port can reach 0, but not 1 (the curves with a maxima in the middle in Figure 2.3b), while the power/splitting-ratio on the bar port can reach 1, but not 0 (the curves with a minima in the middle in Figure 2.3b).

Finally, a frequently used component is the balanced coupler, i.e. a coupler with 50/50 splitting ratio, also called 3 dB coupler. The transmission matrix of

a symmetric ($\Delta\beta = 0$) balanced coupler can be easily obtained from Eq. 2.7:

$$T_c = \frac{1}{\sqrt{2}} \begin{bmatrix} 1 & -i \\ -i & 1 \end{bmatrix}. \tag{2.12}$$

### 2.1.4 The Mach-Zehnder interferometer

A typical integrated Mach-Zehnder Interferometer (MZI) is reported in Figure 2.4. It is made out of two 3 dB directional couplers, where the two couplers are connected with two decoupled waveguides with different length introducing a phase term between them.

To calculate the transmission matrix, it is convenient to divide the MZI into its primary elements, i.e. the couplers and the phase shifter, writing the transmission matrix for each and recovering the overall transmission matrix by a simple matrix product. Using symmetric balanced couplers, the transmission matrix of each coupler, $T_{c1}$ and $T_{c2}$, is given by Eq. 2.12, while the transmission matrix of the phase shifter is given by:

$$T_L = \begin{bmatrix} \exp(-i\varphi_{L1}) & 0 \\ 0 & \exp(-i\varphi_{L2}) \end{bmatrix} = \exp(-i\varphi_{L1}) \begin{bmatrix} 1 & 0 \\ 0 & \exp(-i\Delta\varphi_L) \end{bmatrix}, \tag{2.13}$$

where $\varphi_{L1}$ and $\varphi_{L2}$ are the phases that the light acquire by propagating in $L_1$ and $L_2$ respectively, and $\Delta\varphi_L$ is their difference which can be written as:

$$\Delta\varphi_L = \varphi_{L1} - \varphi_{L2} \simeq \beta_1 L_1 - \beta_2 L_2 = \frac{2\pi}{\lambda}(n_{eff1}L_1 - n_{eff2}L_2) = \frac{2\pi}{\lambda}\Delta L_{eff} \tag{2.14}$$

where the effective imbalance $\Delta L_{eff}$ can be obtained by a different geometrical length between $L_1$ and $L_2$, i.e. $\Delta L_{eff} = n_{eff}\Delta L$, or from equally long waveguides but with different effective refractive index, i.e. $\Delta L_{eff} = \Delta n_{eff}L$. Varying $\Delta n_{eff}$ can also be obtained dynamically, e.g. by placing a resistive heater over one of the two arms and by exploiting the thermo-optic effect.

By following the same procedure and terminology as in Section 2.1.3, it is
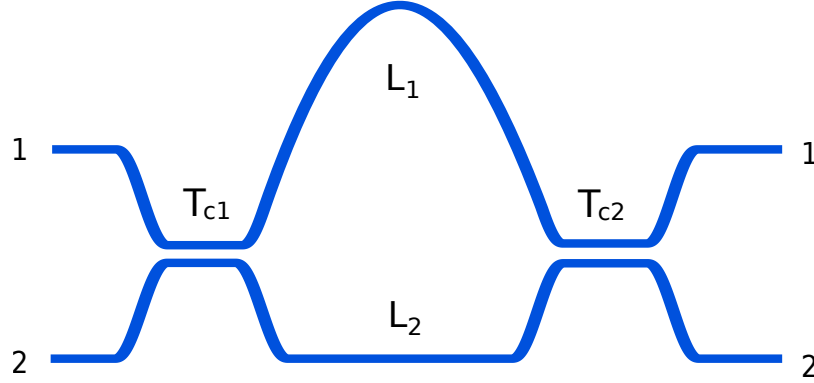
Figure 2.4: The Mach-Zehnder interferometer. Two 3 dB directional couplers ($T_{c1}$ and $T_{c1}$), are connected with two decoupled waveguides (1 and 2) with different length ($L_1$ and $L_2$) introducing a phase term between the two waveguides. An alternative approach for introducing the phase shift is to keep the same length ($L_1 = L_2$), but with different refractive indexes ($n_{eff1} \neq n_{eff2}$).

then possible to derive the following:

$$
\begin{aligned}
P_{bar} &= P_0 \sin^2(\frac{\Delta\varphi_L}{2}), \\
P_{cross} &= P_0 \cos^2(\frac{\Delta\varphi_L}{2}).
\end{aligned}
\tag{2.15}
$$

From Eq. 2.8 and Eq. 2.15 it is possible to appreciate the similarity between the MZI and the directional coupler behaviours. However, while the splitting ratio of a directional coupler is proportional to $kL_c$, the splitting ratio of a MZI is proportional to $\Delta L_{eff}$. This makes the MZI a much more robust structure since, in contrast to $k$, $\Delta L_{eff}$ can be easily controlled with the very important additional possibility of using the active control.

## 2.2 Lithographic technologies

The most conventional technologies to fabricate integrated optical devices are based on lithographic process. Several substrates may be used, in the following, we will introduce briefly the ones that are most commonly used.

### 2.2.1    Silica-on-Silicon technology

As seen in Figure 2.5a and as the name suggests, the waveguides in glass on silicon technology are made out of silica ($SiO_2$) grown on a Si substrate. The cladding is made out of pure $SiO_2$, while the refractive index of the core is increased by doping the $SiO_2$ with ions such as Germanium, Phosphorus or Titanium. The process is CMOS compatible: starting from a Si wafer, a $SiO_2$ is grown by *Chemical Vapour Deposition* (CVD) [30], a polymeric resist layer is deposited and then washed selectively by first developing the resist using a custom made mask and a proper light source. Finally, the exposed regions are doped, and the process is completed. In this way the air acts as an upper cladding, however, if enhanced device stability is needed, an upper cladding made from $SiO_2$ can be deposited.

The waveguides in this technology are characterised by a low birefringence and propagation losses (0.01 dB/cm), while the achieved index-contrast $\Delta n$ [1] is about 0.3%.
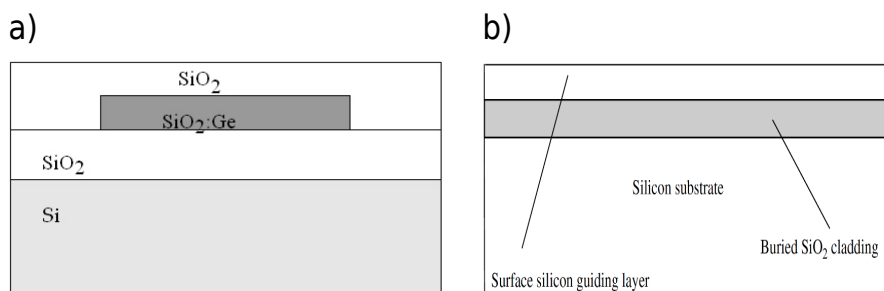


Figure 2.5: (a) Cross-sectional representation of Silica-on-Silicon waveguide. The Silicon (Si) is used as a supporting substrate, the cladding is realised in Silicon dioxide ($SiO_2$), while the core is realised with Silicon dioxide doped with Germanium ($SiO_2$:Ge), alternatively, Phosphorus or Titanium may be used instead of Germanium. (b) Silicon-On-Oxide (SOI) wafer for silicon photonics. Silicon is used as substrate, the buried $SiO_2$ and the air are used as lower and upper cladding respectively, and the surface silicon is used as a guiding layer.

---

[1]The index-contrast $\Delta n = (n_{core} - n_{cladding})/n_{core}$ is the most important parameter that defines the behaviour of the dielectric optical waveguide. $\Delta n$ directly influences the waveguide dimensions, bending radius, losses and birefringence. In particular, the higher is the index-contrast, the smaller is the feature size of the waveguide, allowing more functions per chip.

### 2.2.2 Silicon photonics

Silicon photonics is a high index-contrast ( $\sim 60\%$) technology, allowing not only the prospect of integrating photonics with electronics but also the realisation of very compact devices and even conceive new ones, such as dense WDM systems where aggressive bending are required. In this technology, propagation losses between 0.1 dB/cm and 0.5 dB/cm are typically achieved.

Silicon is transparent at 1550 nm which makes it a good candidate as an optical medium for passive optical devices (such as waveguides and directional couplers) that work in the telecommunication band. However, the possibility of combining both passive optical devices with active optical devices (such as optical amplifiers and photodiodes) is hindered by the fact that silicon is an indirect band-gap material.

The most direct way to produce waveguides in Silicon is to use the already well developed Silicon-On-Oxide wafers, originally conceived for high-performance CMOS devices. The arrangement of SOI wafer is shown in Figure 2.5b. The purpose of the surface silicon layer ($n = 3.5$) is to acts as a guiding layer, while the purpose of the buried oxide layer ($n = 1.5$) is to serve as the lower cladding layer. It prevents the field of the optical modes from penetrating the silicon substrate below. Therefore, the oxide thickness will be satisfactory, as long as it is thicker than the evanescent fields associated with the modes. The air ($n = 1$) is used as an upper cladding. Sometimes a surface oxide layer is also introduced as a passivation layer. There are several patented processes for SOI-wafer fabrication; one example is the SIMOX process [31].

### 2.2.3 Indium phosphide

Indium phosphide (InP) platform permits the realisation of passive components and active devices like lasers and optical amplifiers on the same substrate. The broad spectrum of InP components includes passive components, phase modulators, optical amplifiers, polarisation converters [32], optical modulators, optical switches, tunable lasers, flip-flops, picosecond lasers and fast wavelength converters [33]

Passive components in InP are characterised by a rather high propagation

39

losses, about one order of magnitude larger than the ones in Silicon photonics. This fact makes InP very efficient for the realisation of small and very high-density optical circuit, but not for the realisation of long connections.

A significant effort is made to develop a hybrid solution, where active components that are made in InP are integrated with passive components that are made in Silicon photonics. The major difficulties to overcome are that Si and InP have a different lattice constant, and different thermal expansion coefficients, which make it almost impossible to apply the traditional high-temperature bondings technics.

## 2.3 Femtosecond laser writing

Besides the conventional lithographic techniques, direct waveguide writing techniques also exist. In direct waveguide writing techniques the optical circuit is "written" by translating the substrate under a laser beam or an accelerated particles beam [34]. In this thesis, Femtosecond Laser Micromachining (FLM) was employed to fabricate the waveguide circuits.

FLM was first demonstrated in 1994 when a femtosecond laser was used for surface ablation of fused silica glass [35] and silver [36]. This technique allows direct waveguide writing by exploiting the non-linear phenomenon that can be induced in the substrate using a focused femtosecond laser beam. A wide range of substrates, such as different glasses and polymers, can be employed. By properly tailoring the irradiation parameters, a different kind of modification such as ablation and refractive index change can be obtained. In particular, the refractive index modification was exploited to fabricate high-quality waveguide with FLM technique as demonstrated for the first by Davis et al. in 1996 [37].

FLM advantages over lithographic techniques can be summarised as following:

- speed-up in prototyping and cost reduction: maskless and single-step fabrication requires a relatively simple setup that does not need expensive tools and the use of clean room facilities.

- flexibility: the same laser source and fabrication setup can be used to fabricate on a wide range of substrates. Indeed, the substrate modification

is based on non-linear absorption in the focal volume of the laser, which is, in first approximation, independent of the chemical composition of the material.

- 3D writing capability: the substrate modification occurs only in the focal volume where the intensity is high enough to induce the non-linear absorption. Thus, circuits with arbitrary 3D design can be inscribed in the bulk.

### 2.3.1 Laser-substrate interaction

When a femtosecond laser pulse is focused in a transparent material, it can induce a non-linear absorption phenomena in the focal volume thanks to the high peak intensity of the femtosecond pulses ($\sim$10 TW/cm$^2$). After few picoseconds, the laser excited-electrons transfers their energy to the lattice leading to a permanent material modification. The process can be divided into three main phases: the initial generation of a free electron plasma followed by energy relaxation and modification of the material.

#### 2.3.1.1 Free electron plasma formation

Outside the focal volume, the intensity is not high enough to induce the non-linear absorption, while linear absorption is avoided by properly choosing the laser frequency within the transparent window of the material. Depending on the laser frequency and intensity, the nonlinear absorption is given by multiphoton ionisation and/or tunnelling photoionisation [38]. Non-linear absorption forms a seed of electrons permitting the phenomena of avalanche photoionisation to start. In the following, each of the above photoionisation mechanism is briefly discussed:

1. **Multiphoton absorption**: involves the simultaneous absorption of $m$ photons of energy $h\nu$ (see Figure 2.6a) by an electron in the valence band, where $\nu$ is the laser frequency, $h$ is the Planck constant and $m$ is a minimum integer that satisfies $mh\nu > E_g$ ($E_g$ is the material band-gap). This effect dominates at low laser intensities and high laser frequencies (under the frequency needed for single photon absorption).
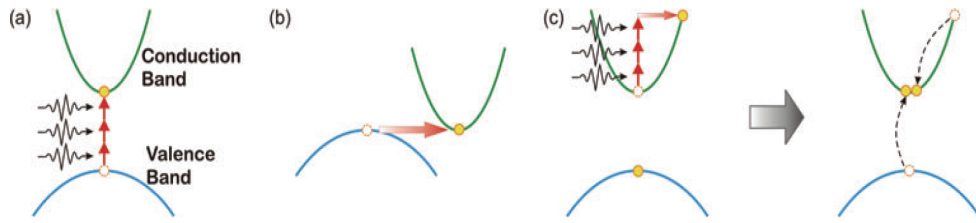
Figure 2.6: Photoionisation in femtosecond laser machining. (a) Multiphoton ionisation, (b) tunnelling ionisation, and (c) Avalanche ionisation [39].

2. **Tunnelling ionisation**: This phenomenon is prevalent at high laser intensity and low frequency, where an electron transit directly from the valence to the conduction band by quantum tunnelling (Figure 2.6b). This happens due to the strong field which reduces the potential barrier between the valence and conduction band by distorting the band structure of the material.

3. **Avalanche ionisation**: a free electron in the conduction band is accelerated by sequential linear absorption of photons (Figure 2.6c), when the excess kinetic energy acquired by this free electron is high enough to cover the band-gap energy jump, the hot electron can impact ionise a bound electron in the valence band, with the net result of two electrons at the bottom of the conduction band. These two electrons can repeat the process by impact-ionising another two electrons, leading to 4 electrons in the conduction band. The process can repeat itself as long as an enough strong laser field is present, resulting in an avalanche of ionisations.

The processes of multiphoton and tunnelling ionisation both require very high pulse peak intensities, which can be achieved only in the focal volume of the focused femtosecond laser pulse. For sub-picosecond laser pulses absorption occurs on a faster timescale than energy transfer to the material, decoupling the absorption and the material heating process [40]. The fact that non-linear absorption occurs only in the small focal volume, together with the absorption-heating temporal decoupling characteristic, results in the creation of a highly localised and controlled seed of free electrons. From this seed, the free electron density can

quickly grow by avalanche ionisation until the plasma frequency approaches the laser frequency, at which point the plasma becomes strongly absorbing.

Femtosecond laser pulses provide a reproducibility that is not otherwise obtainable with longer pulses (several picoseconds or nanosecond duration). Indeed, if the total pulse energy is maintained constant but longer pulses are used, the peak intensity will not be sufficiently high to initiate the multiphoton and tunnelling ionisation. In this condition, the only possible mechanism of absorption is the avalanche ionisation. The free electron seed of this avalanche ionisation is originated from thermally excited impurities and defect states [35]. Since impurities and defects are not homogeneously distributed throughout the material; consequently, the pulse absorption process will not be well reproducible.

### 2.3.1.2 Relaxation and modification

The free-electron plasma formation is followed by its relaxation, transferring the excess energy to the material and leading to its modification. The physical mechanisms responsible for the material modification in the phase of plasma relaxation are not entirely understood yet. Nevertheless, depending on the irradiation parameters (energy, pulse duration, repetition rate, wavelength, polarisation, focal length, scan speed, and others). Two different modifications regimes can be identified; these regimes are also observable by merely changing the laser energy [41]:

1. **void formation**: if very high pulse energy is used, then material damage will occur, leading to the formation of micro-explosions and void like structures. These voids are not suitable for optical waveguides; nevertheless, useful applications have been studied, such as three-dimensional optical storage [42] and photonic band-gap materials [43].

2. **permanent refractive index change**: for lower pulse energy the plasma relaxation phase does not introduce any damage in the material, but the material maintains its good optical qualities and acquires a permanent refractive index change. Several mechanisms concur to produce the refractive index modification, including material densification caused by rapid quenching of the melted glass in the focal volume [44], colour centre formation [45], ion migration effects [46], and pulse-induced shock waves [47]. The relative

role of each mechanism has not been completely clarified; it depends anyway on the material and the exposure conditions.

## 2.3.2 Fabrication parameters

### 2.3.2.1 Focusing conditions

To achieve a micro-metric sized focal volume that efficiently drives the non-linear absorption, focusing optics focuses the incident femtosecond laser pulse in the substrate: microscope objectives are a typical choice. For a Gaussian beam, the diffraction-limited minimum waist radius $w_0$ is given by:

$$w_0 = \frac{M^2 \lambda}{NA\pi}, \tag{2.16}$$

where $M^2$ is the Gaussian beam quality factor, NA is the numerical aperture of the focusing objective and $\lambda$ is the free space wavelength. While the Rayleigh range $z_0$ (1/2 the depth of focus) is given by:

$$z_0 = \frac{M^2 n \lambda}{\pi NA^2}, \tag{2.17}$$

where $n$ is the refractive index of the glass. Eq. 2.16 and Eq. 2.17 underline the importance of a high NA for achieving a tight and less elongated focusing.

Additional spherical aberration may be introduced by the glass-air index mismatch, resulting in a dependence of the written structures on the depth [48]. This depth dependence is more pronounced for higher NA objectives [40]. Oil immersion objectives can present a solution to this problem [40]; however, this kind of objectives have a limited working distance, reducing the processing depth range.

### 2.3.2.2 Fabrication geometry

Figure 2.7 reports the two possible waveguide writing configurations, namely the longitudinal and transversal configurations. In the longitudinal configuration, the sample is translated parallel to the incident laser beam. Due to the transverse symmetry the Gaussian profile of the laser beam, the waveguides exhibit a cylindrical symmetry. The main disadvantage of this configuration is that waveguide
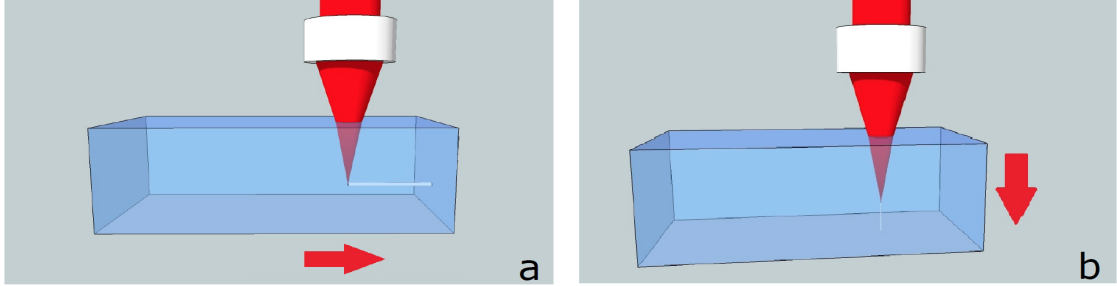
Figure 2.7: Schematic of the possible writing configurations; transversal writing (a), longitudinal writing (b). The red arrows indicate the sample translation direction [52].

length is limited by the working distance of the objective, which is hardly longer than several millimetres. An additional disadvantage of this geometry is that the degree of spherical aberration induced on the laser beam by the substrate changes significantly with the depth, resulting in changes in the shape of the incident laser pulse, which in turn changes the shape of the induced modification. Adaptive optics technics can be employed to compensate this effect [49]; however, this will significantly complicate the experimental setup.

In the transverse writing configuration, the sample is translated orthogonally about the incoming laser beam. The working distance of the objective does not impose any limit on the waveguide length, and 3D structure may be written over a depth range of several millimetres. The disadvantage of this configuration is that waveguide cross section is not circular anymore, but it is elliptical, leading to elliptical guided modes which may not perfectly couple to optical fibres. Besides this asymmetry leads to intrinsic waveguide birefringence which, depending on the application, may or may not be desired. Compensating those effects require some special techniques, like beam shaping techniques to obtain a round focal spot [50], or a multi-scan writing approaches [51].

### 2.3.2.3 Repetition rate and pulse energy

The repetition rate is a crucial parameter which has a strong influence on the waveguide characteristics. Changing the repetition rate determines completely

different regimes [53].

In low repetition rate regime (1 ÷ 200 kHz), the time interval between two consecutive pulses is long enough to permit a complete thermal relaxation of the material before the next pulse arrives. In this way the modification is mainly determined by the individual pulses and waveguides written in the transverse geometry exhibits a highly asymmetric cross section [54]. For this reason, beam shaping techniques are required to obtain a circular waveguide cross section.

By increasing the repetition rate to several MHz, the time interval between two consecutive pulses is short compared to the heat diffusion time (about 1 $\mu$s in glass), and strong cumulative effects take place [44]. In this regime, typically femtosecond laser oscillators without amplification stage are used, with low energy pulses that require a tight focusing by high NA objectives to trigger the non-linear absorption. Although tight focusing will result in a small focal volume, thermal accumulation and heat diffusion effects generate a significant isotropic modification volume around the focal region, generating a waveguide with circular cross section without the use of beam shaping techniques [55].

An interesting regime is observed in the intermediate repetition rate regime (hundreds of kHz to few MHz) [54][53], where a gradual appearance of thermal accumulation effects occur. This regime can combine the benefits of the low and high repetition rate regime: a strong modification is given by more energetic pulses, while the thermal accumulation effects still guarantee uniformity of waveguide cross section. Yb-based femtosecond oscillators are typically used in this regime, with pulse energies up to some $\mu$J. Those pulses are energetic enough to induce the non-linear absorption without special tight focusing requirements, permitting the use of objectives with moderate NA, exploiting the full 3D capability of femtosecond micromachining technique.

#### 2.3.2.4 Other parameters

In addition to pulse energy, focal length and repetition rate, other irradiation parameters may influence the waveguides written with femtosecond laser micromachining technique. The incident laser polarisation and the pulse duration have a big influence on the properties of waveguides that are written in fused silica

[56]. In contrast, no detectable differences were found in EAGLE2000 borosilicate glass [53]. The substrate transition speed affects the amount of energy deposited per unit of volume and can be used to finely tune the waveguide properties. The wavelength of the writing laser determines the order of the nonlinear multiphoton absorption, in some material the employment of certain wavelength is desired. The direction of writing was also found to influence the laser material interaction, this can be explained due to pulse front tilt in the ultrafast laser beam [57].

### 2.3.3   Example of components

Since the discovery of femtosecond laser fabrication of waveguides by Davis et al. in 1996 [37], various optical devices have been demonstrated. For the scope of this thesis, we only review the directional coupler and the Mach-Zehnder interferometer.

#### 2.3.3.1   Directional coupler

The behaviour of the directional coupler is very sensitive to even slight imperfections or variations in the circuit design or waveguide properties. Thus, the successful realisation of a directional coupler in new technology is a clear benchmark for its integrated optics fabrication capability.

Streltsov and Borrelli demonstrated the first directional coupler with FLM technique in 2001 [58]. Their directional coupler was done in borosilicate glass and by employing the second harmonic of high repetition rate Ti:sapphire oscillator.

The first femtosecond laser written directional coupler that works at 1550 nm is due to Osellame et al. [59]. The authors have exploited the 3D fabrication capability to fabricate an X-coupler as shown in Figure 2.8a. The intersection angle $\alpha$ sets the interaction length of the coupler and the depth displacement h influences the coupling strength.

Figure 2.8b shows another example of 3D device which functions as 3 x 3 directional coupler [60]. The structure consists of 3 waveguides that are fabricated on the edges of an equilateral triangle. The device IL was 6.6 dB and the difference between the vertical and horizontal polarisation was 11%.
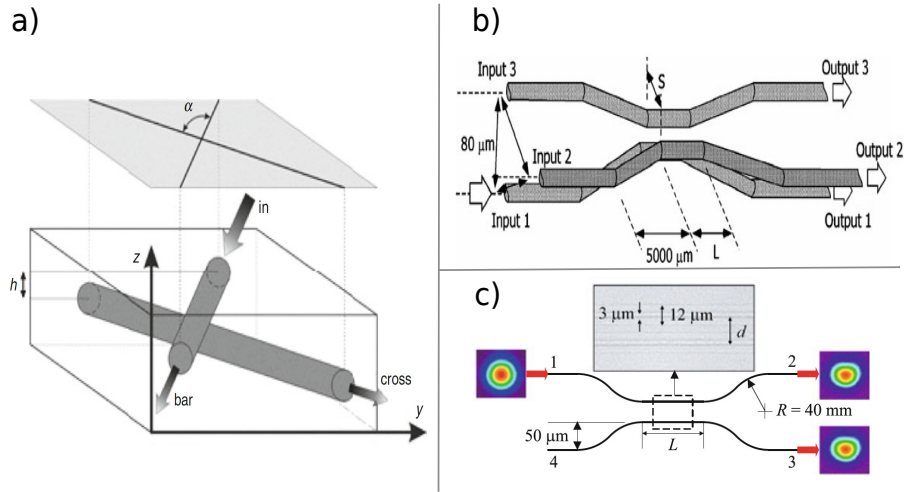
Figure 2.8: (a) Schematic representation of 3D X-coupler that works in the telecom range [59]. (b) Schematic configuration of a 3 x 3 directional coupler [60]. (c) Schematic of a 3 dB directional coupler and optical microscope image of waveguides in the coupling region (top) together with mode profiles of 1550 nm laser light [61]

2D directional couplers were also fabricated in borosilicate glass and characterised at 1550 nm by Eaton et al. [61]. The coupler was designed as in Figure 2.8c, with symmetric double S-bend waveguides with a 40 mm radius of curvature. Coupling distances d from 7.5 to 22.5 $\mu$m and interaction lengths L from 2 to 30 mm were investigated. 50/50 splitting was demonstrated for $d = 10$ $\mu$m and $L = 20.6$ mm. The IL of the directional couplers at 1550 nm was 2.5 dB. The authors have also found that the coupling performance is not hindered if $d = 7.5$ $\mu$m was used, despite a slight overlap of the outer cladding of the two waveguides.

### 2.3.3.2 Mach-Zehnder interferometer

The first demonstrated MZI written with FLM consisted of two X-couplers crossing at 2° as represented in Figure 2.9a [62]. Wavelength filtering behaviour is achieved by the geometrically unbalanced design. By injecting broadband infrared light, interference fringes were observed in the transmission spectrum, whose periodicity fits for a 9.3 $\mu$m path imbalance. This showed good agreement with the

design path length difference of 10 $\mu$m.

MZI electro-optic modulator in fused silica was demonstrated by Li et al. [63]. The substrate region in which the two interferometer's arms are fabricated by laser pulses is thermally treated so to induce an electro-optic coefficient. Gold electrodes, subsequently deposited on the surface of the sample, allow to impose an external electric field and thus modulate the refractive index seen by the light travelling in the two arms, generating a phase difference between them.

A thermally reconfigurable MZI was demonstrated in 2015 by Flamini et al. [64] where an FLM written thermally-controlled MZI that works at 1550 nm was realised. The MZI structure was written in borosilicate glass, followed by gold deposition and patterning, achieving resistive heaters on the chip surface. Figure 2.9c reports a schematic representation of the process. The two balanced couplers of the MZI were inscribed at 70 $\mu$m depth with 14 $\mu$m coupling distance and 200 $\mu$m interaction length. One of the arms was brought to 25 $\mu$m depth and the other to 115 $\mu$m depth permitting a different heat-induced active $n_{eff}$ modulation for each arm. A 50 nm gold layer was sputtered, and the resistors patterns were laser-ablated. The transmission in the cross-arm in function of the power dissipated on the resistors is reported in the graph of Figure 2.9c, fitting a curve with $0.964 \pm 0.003$ fringes visibility.

## 2.4 Managing polarisation in integrated optics

Light polarisation degree of freedom sometimes is adopted as information carrier in photonics technologies; one example is the polarisation division multiplexing for increasing the bandwidth capability of optical communications. As mentioned in the previous chapter, the polarisation degree of freedom is also crucial in quantum information where it is often used to encode the qubits. However controlling and manipulating the polarisation of light in an optical waveguide is not trivial, especially for waveguides produced with lithographic techniques because it requires an accurate control of the waveguide cross-section. In contraries, tailoring the irradiation parameter of FLM, low birefringence waveguides are possible to obtain, paving the way for optical devices that can work with the polarisation degree of freedom.
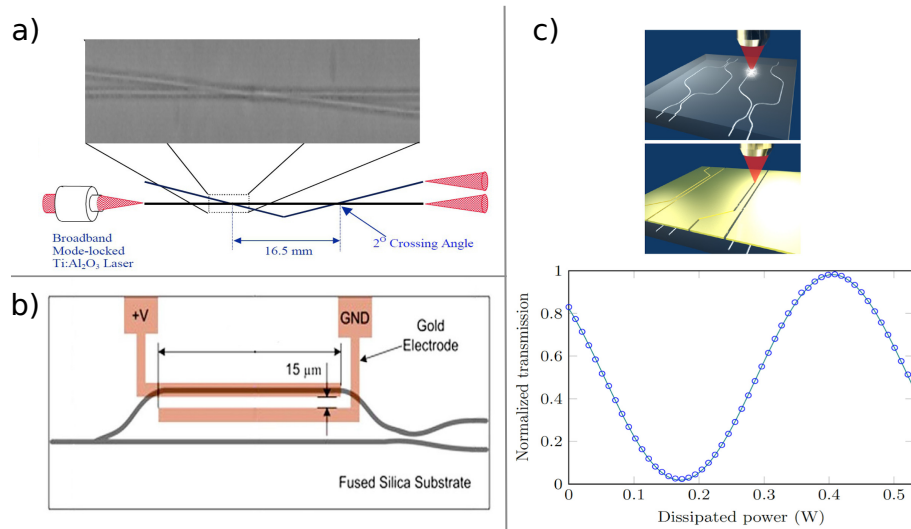
Figure 2.9: (a) Schematic representation of MZI with phase-contrast microscope images [62]. (b) Schematic of the MZI electro-optic modulator realised in fused silica substrate [63]. (c) Thermally-Reconfigurable MZI. A schematic representation of the process of 3D MZI writing (top picture) and gold coating and patterning (bottom picture). The graph reports the experimental characterisation of the device with 1550 nm light. The transmission of the interferometer in the cross-arm is plotted as a function of the thermal power dissipated by the resistor [64].

### 2.4.1 Origin of polarisation dependent behaviour

In Section 2.1.1 we have shown that the mode shape $E(x,y)$ is given by resolving the eigenvalue Eq. 2.2. Any asymmetry in the waveguide cross-section (i.e. in $n(x,y)$) would result in an asymmetry in the field distribution. Besides, asymmetrical cross-section induces a form birefringence (effective refractive index anisotropy due to shape). In single mode waveguides, form birefringence breaks the degeneracy of the orthogonally polarised fundamental modes, leading to different field distribution and propagation constant for each polarisation. In particular, when an evanescent-field coupling is involved, birefringence and mode shape differences lead to a different coupling coefficient for the two polarisations as seen in Eq. 2.6. Since most devices in integrated optics rely on the evanescent-field coupling, the break of degeneracy causes optical devices to behave significantly different for the two orthogonal polarisations. Finally, fibre-waveguide coupling losses and propagation losses are dependent on the spatial properties of the guided modes; consequently, they are also polarisation dependent.

### 2.4.2 Managing polarisation in femtosecond laser written circuits

Dissimilarity in the two orthogonal field distributions and form birefringence are present in waveguides written with femtosecond micromachining. This fact is partly attributed to the elliptical cross-section of the waveguides, especially if transversal writing configuration is used. Besides, birefringence can also arise from intrinsic material anisotropy and mechanical stress accumulated in the substrate [65]. In the following, we will introduce different FLM fabricated devices that are used to manipulate the light polarisation.

FLM written directional couplers can manifest a slight difference in the coupling coefficients between the vertical and horizontal polarisations. By exploiting this phenomenon, Crespi et al. [66] have demonstrated a Partially Polarising integrated Beam Splitter (PPBS) that were fabricated in borosilicate substrate and worked at 806 nm. The coupling distance d was at 7 $\mu$m, while a coupling length L was varied first from 0 to 2 mm, allowing to evaluate the beating length difference between the two polarisations, and second from 5.6 to 8.6 mm were the

required PPBC region was estimated. Figure 2.10a reports the splitting ratios on the transmission port. At $L = 7$ mm a splitting ratios of $T_H = 0$ and $T_V = \frac{2}{3}$ were achieved, while at $L = 7.4$ mm a splitting ratios of $T_H = \frac{1}{3}$ and $T_V = 1$ were achieved.

In fused silica, strong birefringence effects can be observed when fabricating waveguides with FLM due to laser-induced nanogratings [67]. Fernandes et al. exploited this birefringence to fabricate integrated polarising beam splitter [68]. In particular, they have fabricated a directional coupler with ∼20 mm long interaction region and 8 $\mu$m waveguide separation that can split the vertical and horizontal polarisation by having one component on the bar and the other on the cross. At 1484 nm, moderately high extinction ratios of 19 dB and 24 dB were observed (see Figure 2.10b), where the extinction ratios were defined as the residual component on the wrong arm calculated in dB.

The 3D fabrication capability of the present technique was exploited by Sansoni et al. [69] to tailor the polarisation behaviour of the directional coupler. The device is shown in Figure 2.11 where the two waveguides in the coupling region were fabricated on a tilted plane with an angle $\theta$ with respect to the horizontal. The ratio between the vertical and horizontal coupling coefficient $C_V/C_H$ in function of the angle $\theta$ is shown in the graph of Figure 2.11. In particular, there exists an angle for which the ratio $C_V/C_H$ equal to 1, i.e. the coupler becomes polarisation insensitive.

An FLM written waveguide is prone to the stress field created in the substrate by a nearby written second waveguide. Heilmann et al. [70] have demonstrated that such stress field can also cause a reorientation of the waveguide optical axis depending on the relative position of the two waveguide. In their study, Heilmann et al. exploited this phenomenon to realise an arbitrary FLM written waveplates by tailoring the length and orientation of a line defects fabricated close to the waveguide itself. The line defects were written slightly above the destruction threshold to avoid light coupling between the waveguide and the defect. Fabricating an arbitrary waveplate means fabricating an arbitrary optical axis and an arbitrary waveguide length. By changing the position of the defect line with respect to the waveguide, optical axes rotation from 0° up to 90° were demonstrated (see Figure 2.12a). The defect length was varied to prove any arbitrary waveplate

with an optical axis at 22.5° and 45° (see Figure 2.12b).

Another technique to obtain integrated waveplated was developed by Corrielli et al. [71]. In this work, the authors use high-NA oil-immersion objective and a writing laser beam with a diameter smaller than the objective aperture (Figure 2.12d). If the laser beam impinges on the objective aperture in an off-centre position, the focus position is not altered, but the beam propagates in the substrate at an angle $\theta$ that depends on the offset distance on the objective (Figure 2.12e). The fabricated waveguide will then have a tilted cross-section, resulting in a rotated birefringence axis. Microscope images of the waveguides and the near-field profile of the modes are reported in Figure 2.12f and Figure 2.12g respectively. The maximum obtained optical axis rotation about the vertical axis was 27°. By exploiting the waveguide birefringence, the possibility to fabricate a tilted optical axis and to fabricate any desired waveguide length, integrated waveplates with arbitrary optical axis can be obtained.
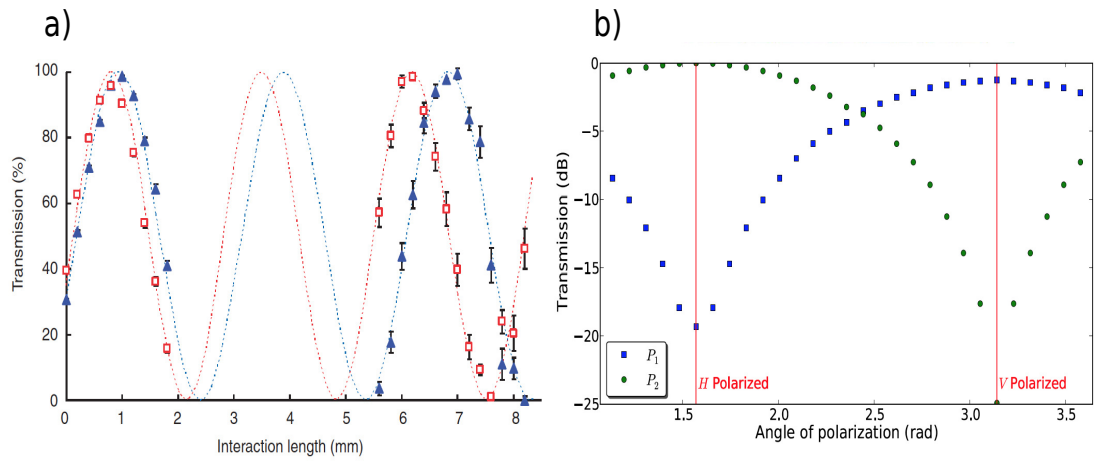
Figure 2.10: Polarising and partially polarising integrated beam splitters. (a) H (squares) and V (triangles) polarisation transmissions of directional couplers with different interaction lengths, based on slightly birefringent waveguides. First, the 0 - 2 mm interaction length range was investigated to evaluate the beating length difference between the two polarisations; the interval of interest to obtain the required PPBS region was estimated to be in the 5.6 - 8.2 mm range, which was consequently explored. Error bars indicate fabrication reproducibility [66]. (b) Integrated polarising beam splitter. Output power and mode profile as a function of the angle of polarisation at 1484 nm, for the bar ($P_1$, green circle) and cross ($P_2$, blue square) [68].
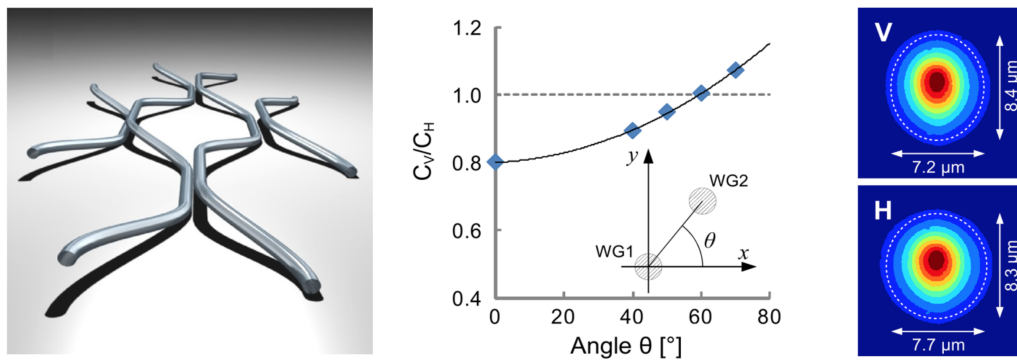


Figure 2.11: A network of polarisation insensitive directional couplers (left panel). In the central graph ratio between the vertical and horizontal coupling coefficients in function of the tilt angle is shown. In the right panel H and V spatial field profiles is shown [69].

54
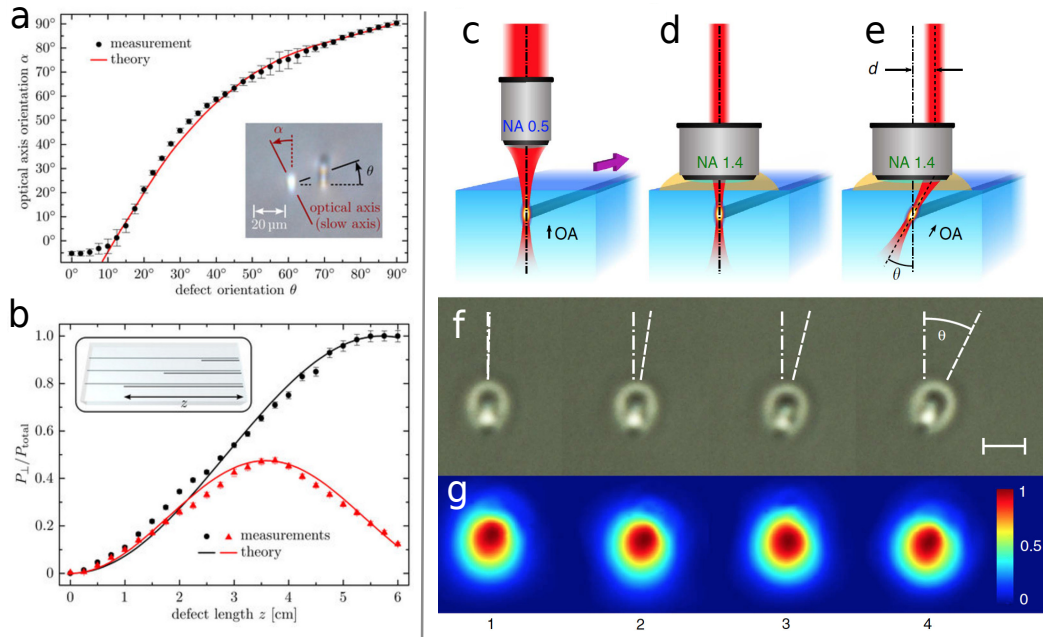
Figure 2.12: FLM written tilted waveplates. Right panel: (a) optical axis rotation in function of the defect position. (b) Tuning the defect length to achieve an arbitrary waveplate. Black refers to 45° optical axis. Red refers to 22.5° optical axis [70]. Left panel: (c) The traditional writing scheme adopting a focusing objective with moderate NA; the symmetry of the writing layout creates birefringent waveguides with the optical axis (OA) aligned as the writing beam direction. (d) Equivalent waveguides can be created by using a high-NA oil-immersion objective. (e) Offsetting the writing beam before the objective results in waveguide writing with an inclined laser beam; the resulting waveguide has an optical axis tilted by an angle $\theta$ that depends on the amount of offset d of the writing beam on the objective axis. (f) End-view microscope images of waveguides (labelled 1 to 4) showing a progressive rotation of the cross-section as the offset d of the writing beam is increased. Scale bar, 5 $\mu$m. (g) Near-field profiles of the waveguide modes at different rotation angles [71].

# Chapter 3

# Experimental Setup

## 3.1 Waveguide fabrication setup

All the waveguides presented in this thesis were fabricated using the same experimental setup, reported in Figure 3.1. Femtosecond laser pulses at 1030 nm wavelength with an adjustable repetition rate between few KHz up to 1.1 MHz are generated by a Yb-based cavity-dumped mode-locked oscillator [72]. The pulses are then delivered by a set of dielectric mirrors to the microscope objective, which focuses the beam in the substrate. The substrate is mounted on a three-dimensional linear motion system, controlled by appropriate software. The correct focusing of the beam on the substrate can be monitored by a CCD camera (not shown in the figure) which collect the substrate back-reflected light. The average laser beam power can be controlled by a Glan-Thompson polariser (PBS) preceded by a half waveplate. Optionally, two movable mirrors can deviate the beam toward a Second Harmonic Generation (SHG) setup, allowing the user to choose between two writing wavelengths: the fundamental at 1030 nm wavelength and its second harmonic at 515 nm. On-demand fast laser blocking and opening (ON-OFF time ~10 ms) is achieved by mean of a mechanical shutter (SH05, Thorlabs).
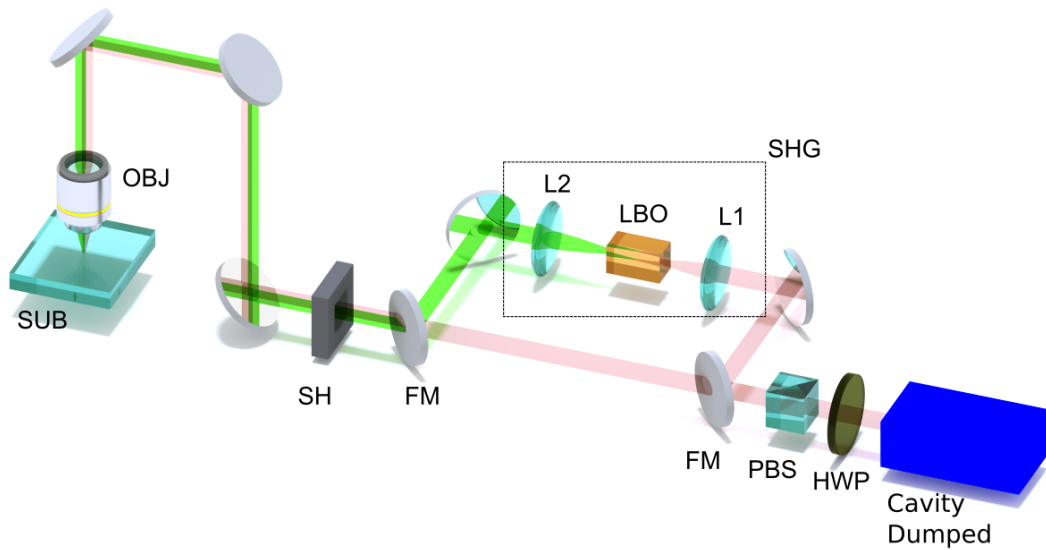
Figure 3.1: Schematic of the fabrication setup. A femtosecond laser beam at 1030 nm (Yb-based cavity-dumped mode-locked oscillator) is delivered to a three-dimensional high-precision translation stage, where the substrate under processing (SUB) is glued. The laser beam is focused on the substrate by mean of the microscope objective (OBJ). A Glan-Thompson polariser (PBS) and a half wave-plate (HWP) allow changing the laser power while a mechanical shutter (SH), synchronised with the motion system, permits a fast laser switching. Two flip mirrors (FM) permit to deviate the laser beam to a second harmonic generation stage (SHG) allowing to perform the fabrication process at 515 nm wavelength. Here, the beam is focused by a 15 cm focal lens (L1) into a temperature controlled Lithium Triborate (LBO) crystal, and the generated light is collimated by a 30 cm focal lens (L2) [73].

### 3.1.1 The laser source

The femtosecond laser source that is used for writing all the waveguides that are presented in this thesis is a cavity-dumped mode-locked oscillator [72]. The laser source provides pulses with 350 fs time duration and maximum energy of 1 $\mu$J. The active material of the laser is $KY(WO_4)_2$ (potassium yttrium tungstate) crystal, doped with Ytterbium at 5% concentration. The wavelength of the laser emission is 1030 nm. An InGaAs laser diode bar is used for the pumping at 980 nm wavelength and with optical pump power on the order of 15 W.

The passive mode-locking regime is achieved with a SESAM (SEmiconductor Saturable Absorber Mirror) which is adopted as an end mirror of the laser cavity. The stretched total cavity length of 8.9 m was folded using several mirrors, allowing a laser footprint of about 90 cm x 50 cm.

Pulse extraction (cavity dumping) is performed using a Pockels cell combined with a Thin Film Polariser (TFP). An external driver is synchronised with the mode-locking pulses that travel in the cavity and control the Pockels cell with a high voltage signal. Due to the polarisation rotation induced by the Pockels cell (proportional to the applied voltage), part of the pulse energy is reflected by the TFP toward the laser output.

The amplitude and the frequency of the external driver signal are tuneable parameters, allowing the user to control the amplitude and repetition rate of the femtosecond pulse. The voltage signal amplitude and frequency can be adjusted between 0 and 2.2 kV and from few KHz up to 1.1 MHz respectively.

### 3.1.2 The motion system

The fabrication of the waveguides is achieved by moving the substrate while maintaining fixed the laser focal spot. The substrate translation is achieved with three-dimensional computer-controlled motion system (Aerotech FIBERGlide 3D) on which the substrate is glued. The motion system consists of three independent linear translation stages, each lies on an air bearing and is driven by brushless linear electric motors. The stages are computer-controlled with G-code language, and their position is constantly monitored by optical encoders with 1 nm resolution, enabling an active control of the movements with an error below 100 nm.

## 3.2 Device characterisation setup

Once the devices fabrication is completed, the devices must be tested and characterised. The experimental setup for waveguide characterisation is described in this section.

### 3.2.1 Observation with optical microscope

The first step to perform after the fabrication is waveguide inspection using an optical microscope (Nikon ME600). This microscope is also equipped with Differential Interference Contrast (DIC) technology, which permits an enhanced vision of small refractive index contrast by exploiting the interference phenomena.

By observing the sample from the top surface, it is possible to verify the devices geometry, dimensions, and whether there are interruptions or defects in the waveguide writing process. The cross section of the waveguides can also be examined by observing the sample from the side.

### 3.2.2 Devices coupling with classical light

The guiding and confinement properties of the waveguides and the proper functioning of the various devices can be tested by launching light at the desired wavelength, using a fibre or an objective, followed by collecting and measuring the output modes.

The laser source that is used for this aim is a tunable laser with a wavelength range from 1450 nm to 1600 nm with a fibre output port (Santec MLS-2000). However, 1550 nm is the wavelength that is used for most measurements presented in this thesis.

Light launching into the waveguides can be done either by objective (Figure 3.2a) or fibre (Figure 3.2b). In the first case, the objective focuses the laser beam to have the beam waist coincident with the waveguide input; the numerical aperture of the objective employed should be of the same order of that of the waveguide ($\sim 0.10$). In the second case, a standard single-mode fibre is brought close to the waveguide facet (butt coupling). In both cases, the aim is to obtain the optimum overlap between the optical mode of the input light and the optical
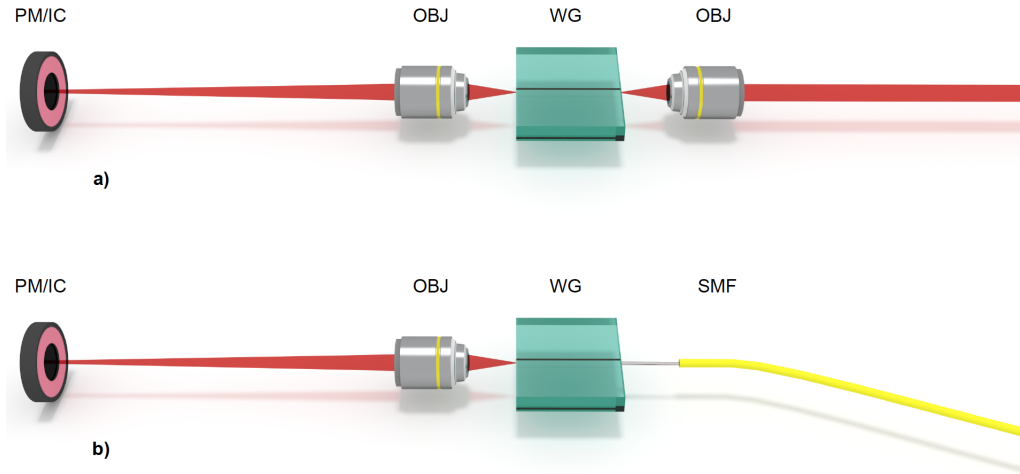
Figure 3.2: Waveguide light coupling configurations. a) Objective coupling configuration: the incoming laser beam is focused by a microscope objective (OBJ) onto the waveguide (WG) input facet. The output is collected by another microscope objective and imaged either on a power meter head (PM) or an imaging camera (IC). b) Fibre-butt coupling configuration: in this case, light is coupled to the device using single mode optical fibre (SMF) [73].

mode of the waveguide.

The fibre or the objective that are used for coupling the light into the waveguide are mounted on three-axis micropositioners (Melles-Griot NanoMAX) with 50nm resolution on each axis. The sample with the optical devices is fixed on four-axis micropositioners (Thorlabs MBT 402), two of the four axes allow the linear translation in the two directions perpendicular to the incoming laser beam, while the other two axes allow the independent adjustment of two sample tilts.

Another objective is used to project the image of the end facet on a Power Meter (PM) (Nova II, Ophir) or Imaging Camera (IM) (Spiricon SP620U). The numerical aperture of this projection objective should be higher than the numerical aperture of the waveguides, guaranteeing the collection of all the light from the waveguide output.

### 3.2.3 Mode profile

Another important property for waveguide characterisation is their mode profile $E(x, y)$. Assuming that we have a monomodal waveguide, which is the case for all relevant waveguides in this thesis, then we can construct the electric field profile $|\vec{E}(x, y)|$ starting from the spatial intensity profile $I(x, y)$ using the simple formula:

$$\left| \vec{E}(x, y) \right| = C \sqrt{I(x, y)}, \tag{3.1}$$

where C is a constant. In our case, the constant C is not relevant since we are interested in the normalised profile, and the absolute value is not a problem since theory guarantees the absence of any sign inversion in the electric field profile of the fundamental mode.

To characterise the mode size, a calibration procedure is needed: First, light is injected in the waveguide from a single mode fibre and the output mode image is acquire (Figure 3.3a). Second, the sample is removed without moving the projection objective, the camera, thus maintaining the same magnification ratio. Third, the fibre is brought close to the projection objective until it is properly focused on the camera and the image of the fibre mode is acquired (Figure 3.3c). Fourth, since the fibre mode size is known, it is possible to obtain the correspondence between the pixel size in the waveguide mode image and the real size of the mode.

### 3.2.4 Device losses characterisation

The attenuation of the propagating light is one of the most important figures of merit of an integrated optical device. The so-called Insertion Losses (IL) are defined as the total losses induced by the device with respect to the case of absence of the device itself, they are given by:

$$IL_{dB} = 10 \cdot log_{10} \left( \frac{P_{in}}{P_{out}} \right), \tag{3.2}$$
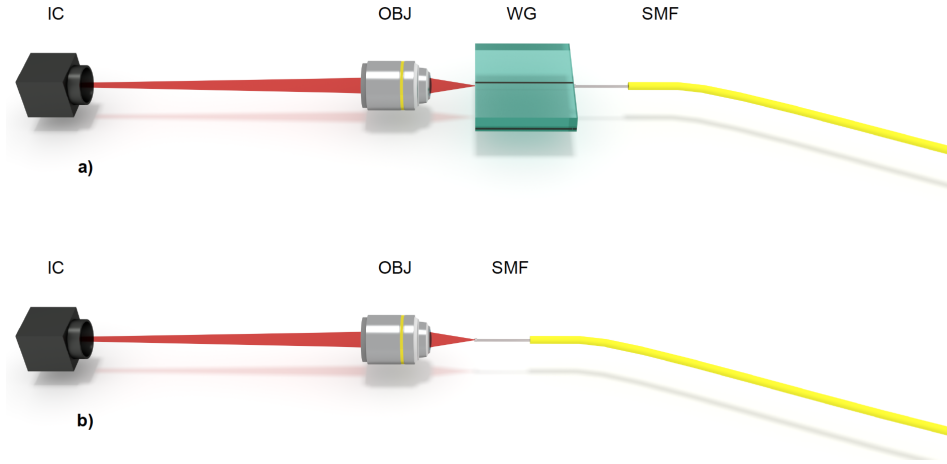
Figure 3.3: Mode shape/size characterisation. (a) the near field profile of the waveguide (WG) mode is acquired with the imaging camera (IC). Information about the mode shape, but not its absolute size, is obtained. (b) the chip is removed and the near field of the single mode fibre (SMF) mode, that has known dimensions, is acquired for calibration [73].

where $P_{out}$ is the output power from the device to be characterised and $P_{in}$ is the injected power.

The characterisation setup is the same as the mode profile acquisition setup (fibre coupling is used), with the only difference that the output is not projected on a camera but on a power meter head. The device IL can be divided into four different contributions: Propagation Loss (PL), Bending Loss (BL), Fresnel Loss (FL) and Coupling Loss (CL).

The coupling losses are caused by the mismatch between the device guided mode $E_{wg}(x, y)$ and the fibre mode that is injected in its input $E_f(x, y)$. They are mainly given by the overlap integral between the two field distributions, expressed in dB:

$$CL_{dB} = -10 \cdot \log_{10} T_c, \tag{3.3}$$

where $T_c$ is the overlap integral given by:

$$T_c = \frac{|\iint E_{wg} E_f dx dy|^2}{\iint |E_{wg}|^2 dx dy \cdot \iint |E_f|^2 dx dy}. \tag{3.4}$$

$T_C$ can be numerically evaluated once the field profiles of the fibre and the waveguide have been acquired with the method previously described.

At the device input and output facets, Fresnel reflections take place due to the refractive index mismatch between glass and air. The Fresnel Losses (FL) account for those reflection and it can be estimated by the following formula:

$$FL_{dB} = -10 \cdot \log_{10} \left[ 1 - \left( \frac{n_2 - n_1}{n_2 + n_1} \right)^2 \right], \tag{3.5}$$

where $n_1$ and $n_2$ are the refractive indices of glass and air respectively. For fused silica where $n_1 = 1.45$, Fresnel losses of $\sim 0.18$ dB occur at both facets.

As mentioned in Section 2.1.1.2, the light undergoes an exponential attenuation when propagating in a real waveguide. Therefore:

$$P(l) = P(0)e^{-\alpha l}, \tag{3.6}$$

where $P(0)$ is the power coupled at the beginning of the waveguide, $\alpha$ is the attenuation coefficient and $l$ is the length of the device. The Propagation Losses (PL) accounts for this exponential attenuation and it is commonly expressed in dB/cm, thus $PL_{dB/cm}$ is given by:

$$PL_{dB/cm} = \frac{10}{l} \cdot \log_{10} \left( \frac{P(0)}{P(l)} \right), \tag{3.7}$$

and by using Eq. 3.6 and Eq. 3.7, it is possible to connect the propagation losses PL to the attenuation coefficient $\alpha$ :

$$P_{dB/cm} = 10 \cdot \log_{10} e \cdot \alpha_{cm^{-1}} \approx 4.3 \cdot \alpha_{cm^{-1}} \tag{3.8}$$

The propagation losses are caused mainly the waveguide walls roughness; any small inhomogeneity in the core refractive index profile is seen as a discontinuity which, as discussed in Section 2.1.1.2, can couple some power from the guided modes to the radiative modes. Scattering defects and absorption centres in the waveguide are seen as other contributors for the PL. A deep and quantitive description of the propagation losses in optical dielectric waveguide is given by Melati et al. [74].

Any waveguide bend presents further losses related to the bend itself, and those are the Bending Losses (BL). It was found, both theoretically [75] and experimentally that the bending losses increase exponentially with decreasing radius of curvature R:

$$BL_{dB/cm} = C_1 \cdot e^{-C_2 \cdot R},\qquad(3.9)$$

where C1 and C2 are constants that depend only on the waveguide size and the guided mode profiles.

To summarise, the IL can be decomposed into four kinds of losses:

$$IL_{dB} = l \cdot PL_{dB/cm} + l_c \cdot BL_{dB/cm} + 2FL_{dB} + CL_{dB},\qquad(3.10)$$

where $l_c$ is the total length of the curved light path and the factor 2 in front of FL takes into account that Fresnel reflections occur both at the input and the output facets.

PL are difficult to measure directly. To obtain the PL: first straight waveguides are fabricated. Second IL and CL are measured as mentioned above, and the approximate value of 0.18 dB for facet is used for the FL. Third, keeping in mind that $l_c = 0$ for straight waveguides, PL can be simply calculated since it is the only unknown in Eq. 3.10. To evaluate BL as a function of the radius of curvature, with the same fabrication parameters and almost the same total length of the waveguide, we can fabricate straight waveguides and bent waveguides with different radiuses of curvature. The BL are then simply obtained as the difference between the IL of the bent waveguides and the IL of the straight waveguides.

### 3.2.5  Polarisation behaviour analysis

The setup to characterise the polarisation behaviour is reported in Figure 3.4. The polarisation of the input laser light is set by mean of a polarising beam splitter (PBS) placed before the input objective. This is followed by a half- (HWP) and a quarter-waveplate (QWP) giving rise to the preparation block where any input polarisation state can be prepared. Occasionally, it is necessary to introduce a polarisation analysis block which can perform a projective polarisation measurement on the circuit output light. For this aim, a mirror replica of the input
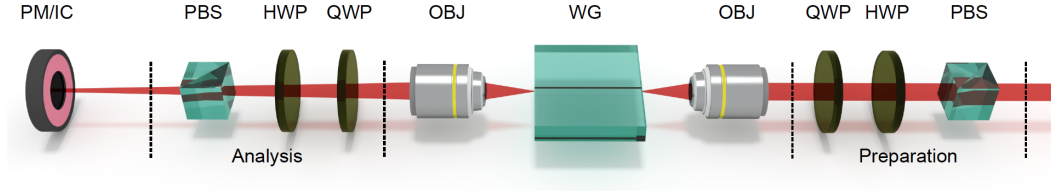
Figure 3.4: Polarisation behaviour analysis. A polarising beam splitter (PBS) together with a half- (HWP) and quarter-waveplates (QWP) are used to generate an arbitrary polarisation input state (preparation block). The same elements are used for the projection of the output light on an arbitrary polarisation bases (analysis block) [73].

preparation block elements is also introduced at the output as seen in Figure 3.4.

**Waveguide birefringence measurement** The polarisation sate of light is described by the Stokes vector:

$$\vec{S} = \begin{bmatrix} S_0 \\ S_1 \\ S_2 \\ S_4 \end{bmatrix} = \begin{bmatrix} 1 \\ (I_H - I_V)/I \\ (I_D - I_A)/I \\ (I_R - I_L)/I \end{bmatrix}. \tag{3.11}$$

The components $S_i$ of the Stokes vector are called Stokes parameters of the beam, $I$ stands for the total light intensity and the quantities $I_{H/V}$, $I_{D/A}$ and $I_{R/L}$ are the intensities obtained by projecting the beam on the Vertical/Horizontal, Diagonal/ Antidiagonal and Right/Left handed circular polarisation bases respectively.

Any optical element can be described by a 4 x 4 matrix, called the Müller matrix **M**, with which the output and input state of light can be related:

$$\vec{S}_{out} = \boldsymbol{M}\vec{S}_{in}. \tag{3.12}$$

A waveguide segment can be seen as a uni-axial birefringent medium with a fixed axis and with a Müller matrix $\boldsymbol{M}_{wg}$ given by:

$$
\boldsymbol{M} = \begin{bmatrix} 1 & 0 & 0 & 0 \\ 0 & \cos^2 2\delta + \sin^2 2\delta \cos\phi & \sin 2\delta \cos 2\phi(1-cos\phi) & \sin 2\delta \sin\phi \\ 0 & \sin 2\delta \cos 2\phi(1-cos\phi) & \sin^2 2\delta + \cos^2 2\delta \cos\phi & \cos 2\delta \sin\phi \\ 0 & \sin 2\delta \sin\phi & -\cos 2\delta \sin\phi & \cos\phi \end{bmatrix} , \quad (3.13)
$$

where $\delta$ is the inclination of the optical axis with respect to the horizontal direction and $\phi$ is the phase difference accumulated in the medium between the components of light along the ordinary and the extraordinary directions, that in turn is proportional to the medium birefringence and length.

Using the preparation block from Figure 3.4, different polarisation states of light with known Stokes vectors can be injected in the waveguide, and the corresponding Stokes vectors of the light in the output can be determined by using the analysis block. $M_{wg}$ is then determined by a numerical fitting, and the experimental values $\delta_{exp}$ and $\phi_{exp}$ are retrieved; i.e, the polarisation behaviour of the optical element is obtained.

# Chapter 4

# On-chip quantum teleportation module: the idea

The objective of this thesis work is to develop an integrated optics solution for quantum teleportation at telecom wavelength. This work is part of a collaboration project between Dr Osellame's femtosecond Laser micromachining group at IFN-CNR in Milan, and Dr Sciarrino's quantum optics group at Sapienza University in Rome. The work in this thesis mainly focuses on the design and fabrication of the integrated optics components realised by Femtosecond Laser Micromachining (FLM), as well as on their characterisation with classical light.

In Section 4.1, we start by giving a motivation for the project. In Section 4.2 the teleportation scheme is described in detail. Finally, keeping in mind the final experimental setup with an entanglement source, in Section 4.3 we try to give a benchmark to validate the goodness of the fabricated devices.

## 4.1 Motivation for the work

Quantum teleportation plays a fundamental role in the progress of quantum information science. It represents one of the building blocks for a future quantum communication network, allowing for the transfer of a quantum state between two distant nodes by exploiting an entangled state resource. The development of integrated circuits for quantum teleportation is justified not only by the need of

inherently stable photonics chips but also for the need of miniaturisation for any future use in quantum computers and quantum networks.

Metcalf et al. [26] on-chip quantum teleportation experiment (see Section 1.3) is an important proof-of-principle that quantum teleportation can also be implemented with waveguide architecture. Nevertheless, being based on a three-photon scheme, the experiment has the disadvantage of achieving only 50% teleportation efficiency. Additionally, all the components required for the teleportation scheme were monolithically fabricated in one chip, allowing only for quantum teleportation within the same chip.

Our project aims to take quantum teleportation a further step forward, taking advantage of the following features:

- Integrated optics approach.

- Scheme with 100% teleportation efficiency.

- Working at 1550 nm wavelength, where the high-efficiency window for fibre communication can be exploited.

- Possibility to achieve quantum teleportation between two distant nodes.

For this aim, we first start by designing and fabricating an integrated circuit for quantum teleportation based on the 100% efficient two-photon scheme. More specifically, our integrated chip would implement only the Preparer and Alice's part of the protocol while Bob's part will be carried out with bulk components at a distant location. Once the integrated circuit is ready, the long distance teleportation capability can be tested by generating an entangled photon pair, coupling one photon to our circuit, and sending the other to Bob over a fibre link (see Figure 4.1).

## 4.2    The teleportation scheme

The scheme that we use in our experiment is a variant of the original two-photon (two-particle) scheme that was presented in Section 1.2.5.3. As in the original scheme, two photons are generated in an entangled state; one photon is sent
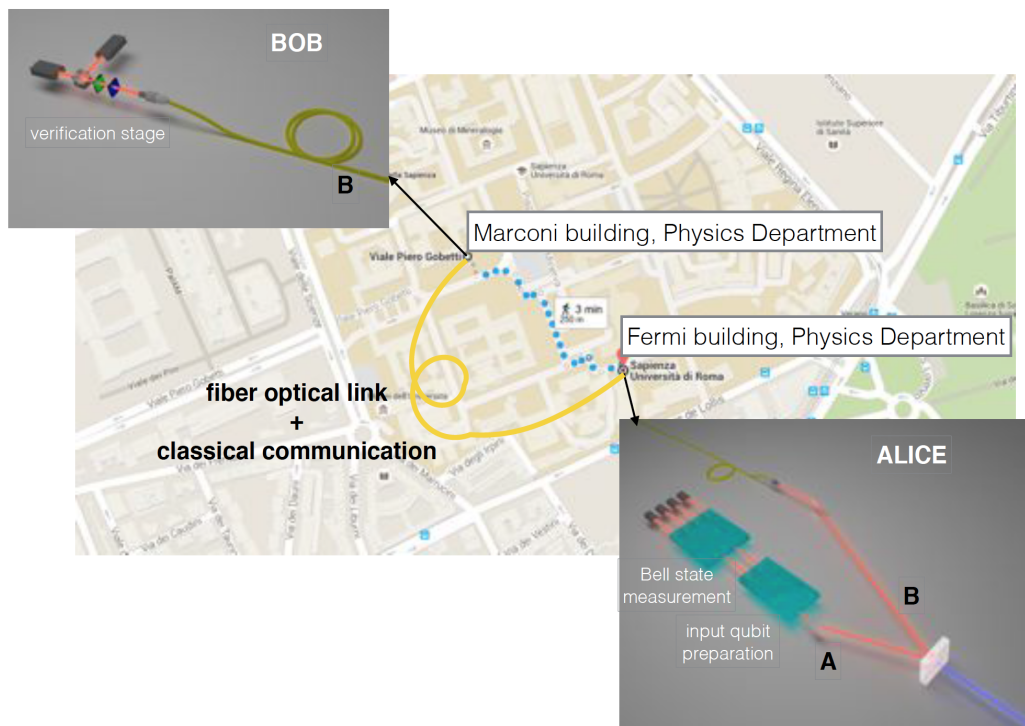
Figure 4.1: Schematic representation of the experiment at Sapienza campus in Rome. Two photons A and B will be generated in a quantum entangled state. Photon A will be sent to the integrated circuits which perform the state preparation and Bell-state projection, while the other photon is transferred to Bob over an optical fibre link. Bob part will be realised with bulk components.

directly to Bob, while the other is sent to Alice through a state preparation stage. The state preparation stage prepares an arbitrary state into an available degree of freedom of Alice's photon. In the original two-photon scheme the path degree of freedom is used for creating the non-local channel, while the arbitrary teleported state is encoded on the polarisation degree of freedom. In contrast, in our scheme, the non-local channel is implemented over the polarisation degree of freedom, while the path degree of freedom is used to encode the arbitrary state. The motivations for such a variant are: first, encoding an arbitrary qubit on the photon path degree of freedom can be easily achieved, in principle, with a tuneable Mach-Zehnder Interferometer (MZI) as will be explained in Section 4.2.1. Second, compared to the original scheme, in our variant scheme fewer optical components are required to implement the BSM as will be explained in Section 4.2.2.

A central idea of the quantum teleportation protocol is that Alice should not know anything about the state that she is teleporting. To highlight this fact, we would like to fabricate two distinct chips: the first chip is called "State Preparation chip" and it contains exclusively the Preparer components. The second chip is called "Path-Polarisation Bell-state measurement" or briefly "BSM" and it contains all the components that Alice needs to perform a BSM. Although this kind of separation is not necessary, in this way not only we draw a clear boundary between the Preparer and Alice, but also we make the problem easier from a technological point of view.

It is worth mentioning that, as the classical two- or three- photon teleportation scheme, our teleportation scheme requires that Bob performs appropriate unitary transformations on his photon after receiving the BSM result from Alice. This would require a fast feedforward techniques which would implement the appropriate unitary transformation at Bob's side, in function of the BSM result, before the arrival of Bob's photon. Alternatively, quantum memories can be used, which would store Bob's photon, giving him the time to implement the appropriate unitary transformation. However, both solutions will be absence in our experimental setup, and the verification of the successful teleportation will be performed statistically as will be described in Section 4.3.

### 4.2.1 State preparation chip

**The idea** The state preparation chip is used to encode any a general qubit state in the photon path degree of freedom. If we indicate by $|1\rangle$ and $|2\rangle$ the two paths in which the photon can propagate, an arbitrarily path-encoded qubit $|\varphi\rangle$ is given by:

$$|\varphi\rangle = \alpha |1\rangle + \beta |2\rangle, \tag{4.1}$$

where $\alpha$ and $\beta$ are the complex probability amplitudes, each with a module and phase term, and can be re-written in the so-called "canonical" parametrisation as:

$$|\varphi\rangle = \sin\frac{\theta}{2} |1\rangle + \cos\frac{\theta}{2} e^{i\phi} |2\rangle, \tag{4.2}$$

where $0 \le \theta \le \pi$ and $0 \le \phi \le 2\pi$.

To implement Eq. 4.2 we simply need a device that splits the classical light by the ratio (measured in power) $\sin^2\frac{\theta}{2} : \cos^2\frac{\theta}{2}$. Indeed, if a single photon is injected in such beam splitter, it will have $\sin^2\frac{\theta}{2}$ probability to exit on one output and $\cos^2\frac{\theta}{2}$ probability to exit on the other. The phase term $\phi$ can be easily implemented by making path 2 longer than path 1, forcing the electric field of the classical light, or the single photon, to accumulate an additional phase term $\phi$ in path 2 with respect to path 1.

An MZI is an obvious solution for such reconfigurable device. As discussed in Section 2.1.4, compared to the directional coupler, the MZI has not only the advantage of being a more robust structure, but it also can be tuned actively by thermally inducing a phase difference between its two arms. Figure 4.2 shows a schematic representation of such MZI based structure. Placing another heater above path 2 in the MZI output will induce the phase term $\phi$.

**Mathematical description** The entangled photon pair is generated with type-II parametric down-conversion. Thus, the initial state of the entangled photon pair is generated in the form:

$$|\psi\rangle_{in} = \frac{1}{\sqrt{2}}(|H\rangle_B |V\rangle_A - |V\rangle_B |H\rangle_A), \tag{4.3}$$
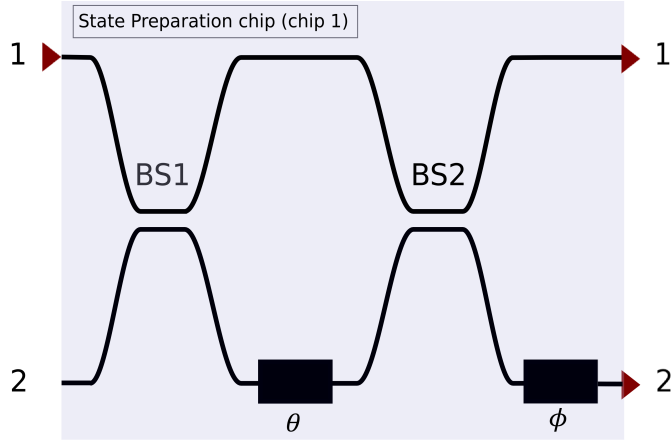
Figure 4.2: Schematic representation of the first chip also called State Preparation chip. This chip represents the Preparer, and it creates an arbitrary qubit in the path degree of freedom of the photon. $\theta$ and $\phi$ are tunable phase shifters. BS1 and BS2 are balanced beam splitters (50/50). The employed input and outputs are indicated with red arrows. Photons will be injected in input 1.

where $|H\rangle$ and $|V\rangle$ indicates the two orthogonal polarisations and the subscripts A and B indicates the two photons: one sent to Alice (A) and the other to Bob (B). The following bracket and matrix notations are used for the path degree of freedom:

$$\text{path } 1 = |1\rangle_S = \begin{bmatrix} 1 \\ 0 \end{bmatrix}, \quad \text{path } 2 = |2\rangle_S = \begin{bmatrix} 0 \\ 1 \end{bmatrix}. \tag{4.4}$$

Ideally, the Preparer encodes the arbitrary state $|\varphi\rangle$ on the path degree of freedom, and the photon polarisation should not influence the state $|\varphi\rangle$. That is the state preparation chip should be completely polarisation insensitive. By considering BS1 and BS2 as ideal 50/50 polarisation insensitive beam splitters, then they can be represented by the following transmission matrixes on the spatial degree of freedom:

$$T_{BS1} = T_{BS2} = \frac{1}{\sqrt{2}} \begin{bmatrix} 1 & i \\ i & 1 \end{bmatrix}, \tag{4.5}$$

while the phase shifters $\theta$ and $\phi$ are given by:

$$T_\theta = \begin{bmatrix} 1 & 0 \\ 0 & e^{i\theta} \end{bmatrix} \quad and \quad T_\phi = \begin{bmatrix} 1 & 0 \\ 0 & e^{i\phi} \end{bmatrix}. \tag{4.6}$$

The transfer function of the first chip, which we indicate with $T_{MZI}$, can then be easily recovered by simple matrix multiplication:

$$T_{MZI} = T_\phi \cdot T_{BS2} \cdot T_\theta \cdot T_{BS1} = ie^{i\frac{\theta}{2}} \begin{bmatrix} -\sin\frac{\theta}{2} & \cos\frac{\theta}{2} \\ e^{i\phi}\cos\frac{\theta}{2} & e^{i\phi}\sin\frac{\theta}{2} \end{bmatrix}. \tag{4.7}$$

The global phase term $ie^{i\frac{\theta}{2}}$ can be dropped, leading to:

$$T_{MZI} = \begin{bmatrix} -\sin\frac{\theta}{2} & \cos\frac{\theta}{2} \\ e^{i\phi}\cos\frac{\theta}{2} & e^{i\phi}\sin\frac{\theta}{2} \end{bmatrix}. \tag{4.8}$$

To have a correct picture of the state evolution, Alice's photon has to be described as part of the two-photon entangled state. Since photon A is injected in path 1 of the MZI, such state can be written as $|\psi\rangle_{in}|1\rangle_S$. At the output of the MZI it becomes:

$$|\psi\rangle_{chip1} = T_{MZI} \cdot |\psi\rangle_{in}|1\rangle_S = T_{MZI} \begin{bmatrix} 1 \\ 0 \end{bmatrix} |\psi\rangle_{in} = \begin{bmatrix} -\sin\frac{\theta}{2} \\ e^{i\phi}\cos\frac{\theta}{2} \end{bmatrix} |\psi\rangle_{in}, \tag{4.9}$$

which by using Eq. 4.3 can also be rewritten as:

$$|\psi\rangle_{chip1} = \frac{1}{\sqrt{2}} \Big[ |H\rangle_B |V\rangle_A \Big( -\sin\frac{\theta}{2}|1\rangle_S + e^{i\phi}\cos\frac{\theta}{2}|2\rangle_S \Big) -$$
$$|V\rangle_B |H\rangle_A \Big( -\sin\frac{\theta}{2}|1\rangle_S + e^{i\phi}\cos\frac{\theta}{2}|2\rangle_S \Big) \Big]. \tag{4.10}$$

We see from Eq. 4.9 that the Preparer is actually encoding, in the path degree of freedom, the state:

$$|\varphi\rangle = -\sin\frac{\theta}{2}|1\rangle_S + e^{i\phi}\cos\frac{\theta}{2}|2\rangle_S, \tag{4.11}$$

which is a generic qubit state for $0 \leq \theta \leq \pi$ and $0 \leq \phi \leq 2\pi$.

At this point, we can define four states that are analogous to the four Bell states introduced in Section 1.1.5; therefore, we call them the Bell-like states:

$$
\begin{aligned}
|\Psi^-\rangle_{AS} &\equiv \frac{1}{\sqrt{2}} \Big( |V\rangle_A |1\rangle_S - i |H\rangle_A |2\rangle_S \Big), \\
|\Psi^+\rangle_{AS} &\equiv \frac{1}{\sqrt{2}} \Big( |V\rangle_A |1\rangle_S + i |H\rangle_A |2\rangle_S \Big), \\
|\Phi^-\rangle_{AS} &\equiv \frac{1}{\sqrt{2}} \Big( |H\rangle_A |1\rangle_S - i |V\rangle_A |2\rangle_S \Big), \\
|\Phi^+\rangle_{AS} &\equiv \frac{1}{\sqrt{2}} \Big( |H\rangle_A |1\rangle_S + i |V\rangle_A |2\rangle_S \Big).
\end{aligned}
\tag{4.12}
$$

By inverting these definitions we obtain the following relations:

$$
\begin{aligned}
|V\rangle_A |1\rangle_S &= \frac{1}{\sqrt{2}} \Big( |\Psi^+\rangle_{AS} + |\Psi^-\rangle_{AS} \Big), \\
|H\rangle_A |2\rangle_S &= -\frac{i}{\sqrt{2}} \Big( |\Psi^+\rangle_{AS} - |\Psi^-\rangle_{AS} \Big), \\
|H\rangle_A |1\rangle_S &= \frac{1}{\sqrt{2}} \Big( |\Phi^+\rangle_{AS} + |\Phi^-\rangle_{AS} \Big), \\
|V\rangle_A |2\rangle_S &= -\frac{i}{\sqrt{2}} \Big( |\Phi^+\rangle_{AS} - |\Phi^-\rangle_{AS} \Big).
\end{aligned}
\tag{4.13}
$$

By substituting these relations in Eq. 4.10 we can rewrite the state $|\Psi\rangle_{chip1}$ in the Bell-like state basis as:

$$
\begin{aligned}
|\Psi\rangle_{chip1} = \frac{1}{2} \Big[ &|\Psi^-\rangle_{AS} \big( -\sin\frac{\theta}{2} |H\rangle_B - ie^{i\phi} \cos\frac{\theta}{2} |V\rangle_B \big) \\
+ &|\Psi^+\rangle_{AS} \big( -\sin\frac{\theta}{2} |H\rangle_B + ie^{i\phi} \cos\frac{\theta}{2} |V\rangle_B \big) \\
+ &|\Phi^-\rangle_{AS} \big( ie^{i\phi} \cos\frac{\theta}{2} |H\rangle_B + \sin\frac{\theta}{2} |V\rangle_B \big) \\
+ &|\Phi^+\rangle_{AS} \big( -ie^{i\phi} \cos\frac{\theta}{2} |H\rangle_B + \sin\frac{\theta}{2} |V\rangle_B \big) \Big].
\end{aligned}
\tag{4.14}
$$

We see that if the global state is projected on one of the states in Eq. 4.12, the qubit teleported to Bob can be transformed into the correct one $(-\sin\frac{\theta}{2} |H\rangle_B + e^{i\phi} \cos\frac{\theta}{2} |V\rangle_B)$ up to a proper unitary transformation. Note that, while the original

state $|\varphi\rangle$ is encoded in the path degree of freedom, the state at Bob end is encoded in the polarisation degree of freedom. The BSM measurement will force Alice's photon to collapse in one of the four Bell-like states. Depending on the result of the BSM, i.e. depending in which Bell-like state the wavefunction has collapsed, a proper unitary transformation will be applied to recover the original state.

## 4.2.2 Path-polarisation Bell state measurement chip

**The idea**   The idea is the same as in the original two-photon scheme (see Section 1.2.5.3); i.e. Alice needs to perform a BSM by entangling the path and polarisation degrees of freedom of her photon. This can be done by first placing a half waveplate (HWP) in one of the two paths. In our experiment, we chose to place the half waveplate in path 2 (see Figure 4.3). Such half waveplate will flip the polarisation of the photon only in path 2, forcing the two orthogonal polarisation in each one of the four Bell-like states (see Eq. 4.12) to become equally polarised. Having the same polarisation, the two probability amplitudes of the photon coming from path 1 and 2 can interfere on the beam splitter (BS3), resulting in an entanglement between the path and polarisation degrees of freedom. Two polarising beam splitter (PBS) will then separate the four Bell-like states on four different single-photo detectors (PD1 to PD4), thus resulting in 100% teleportation efficiency.

**Mathematical description**   The two outputs of the state preparation chip must be coupled to the two inputs of the BSM chip (red coloured in Figure 4.3), which we still indicate with $|1\rangle_S$ and $|2\rangle_S$. To see why the reported structure of this chip performs a BSM, we start from the previously defined four Bell-like
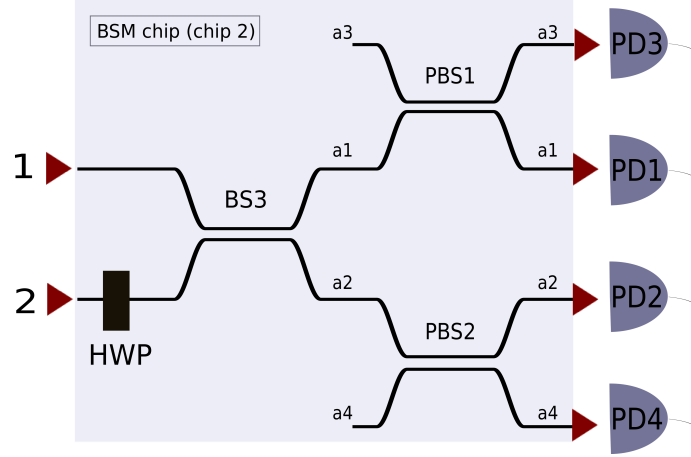
Figure 4.3: Schematic representation of the second chip also BSM chip. This chip allows Alice to perform a BSM on her part of the entangled photon pair. HWP is half waveplate. BS3 is a balanced beam splitter. PBS are polarising beam splitters. PD are single-photon detectors. The inputs and outputs of the chip are indicated with red arrows.

states and propagate them element by element in the BSM chip:

$$
\begin{aligned}
|\Psi^-\rangle_{AS} &\equiv \frac{1}{\sqrt{2}} \left( |V\rangle_A |1\rangle_S - i\,|H\rangle_A |2\rangle_S \right) \xrightarrow{HWP} \frac{1}{\sqrt{2}} |V\rangle_A \left( |1\rangle_S - i\,|2\rangle_S \right) \xrightarrow{BS3} |V\rangle_A |1\rangle_S\,, \\
|\Psi^+\rangle_{AS} &\equiv \frac{1}{\sqrt{2}} \left( |V\rangle_A |1\rangle_S + i\,|H\rangle_A |2\rangle_S \right) \xrightarrow{HWP} \frac{1}{\sqrt{2}} |V\rangle_A \left( |1\rangle_S + i\,|2\rangle_S \right) \xrightarrow{BS3} i\,|V\rangle_A |2\rangle_S\,, \\
|\Phi^-\rangle_{AS} &\equiv \frac{1}{\sqrt{2}} \left( |H\rangle_A |1\rangle_S - i\,|V\rangle_A |2\rangle_S \right) \xrightarrow{HWP} \frac{1}{\sqrt{2}} |H\rangle_A \left( |1\rangle_S - i\,|2\rangle_S \right) \xrightarrow{BS3} |H\rangle_A |1\rangle_S\,, \\
|\Phi^+\rangle_{AS} &\equiv \frac{1}{\sqrt{2}} \left( |H\rangle_A |1\rangle_S + i\,|V\rangle_A |2\rangle_S \right) \xrightarrow{HWP} \frac{1}{\sqrt{2}} |H\rangle_A \left( |1\rangle_S + i\,|2\rangle_S \right) \xrightarrow{BS3} i\,|H\rangle_A |2\rangle_S\,.
\end{aligned}
$$

$$(4.15)$$

Where the following transmission matrixes have been considering in the above states evolution:

$$
T_{HWP} = \begin{bmatrix} 0 & 1 \\ 1 & 0 \end{bmatrix}, \text{ which acts on } |H\rangle_A = \begin{bmatrix} 1 \\ 0 \end{bmatrix}, \text{ and } |V\rangle_A = \begin{bmatrix} 0 \\ 1 \end{bmatrix}. \qquad (4.16)
$$

$$T_{BS3} = \begin{bmatrix} 1 & i \\ i & 1 \end{bmatrix}, \text{ which acts on } |1\rangle_S = \begin{bmatrix} 1 \\ 0 \end{bmatrix}, \text{ and } |2\rangle_S = \begin{bmatrix} 0 \\ 1 \end{bmatrix}. \qquad (4.17)$$

The final step is to apply PBS1 between paths $a_1$ and $a_3$, and to apply PBS2 between paths $a_2$ and $a_4$ (see Figure 4.3), followed by a photodetection with the four single-photons detectors (PD1 to PD4) on the modes $a_1$ to $a_4$:

$$\begin{aligned}
|\Psi^-\rangle_{AS} &\xrightarrow{PBS1} |V\rangle_A |a_1\rangle_S \rightarrow \text{detection with PD1}, \\
|\Psi^+\rangle_{AS} &\xrightarrow{PBS2} |V\rangle_A |a_2\rangle_S \rightarrow \text{detection with PD2}, \\
|\Phi^-\rangle_{AS} &\xrightarrow{PBS1} |H\rangle_A |a_3\rangle_S \rightarrow \text{detection with PD3}, \\
|\Phi^+\rangle_{AS} &\xrightarrow{PBS2} |H\rangle_A |a_4\rangle_S \rightarrow \text{detection with PD4}.
\end{aligned} \qquad (4.18)$$

From these relations, it is possible to see that a click on each single-photon detectors will indicate the detection of one of the four Bell-like states.

Having propagated photon A in the BSM, the final state of the system $|\Psi\rangle_{chip2}$ can be obtained by substituting Eq. 4.18 in Eq. 4.14:

$$\begin{aligned}
|\Psi\rangle_{chip2} = \frac{1}{2} \Big[ \ & |V\rangle_A |a_1\rangle_S \big( -\sin\frac{\theta}{2} |H\rangle_B - i e^{i\phi} \cos\frac{\theta}{2} |V\rangle_B \big) \\
& + i |V\rangle_A |a_2\rangle_S \big( -\sin\frac{\theta}{2} |H\rangle_B + i e^{i\phi} \cos\frac{\theta}{2} |V\rangle_B \big) \\
& + |H\rangle_A |a_3\rangle_S \big( i e^{i\phi} \cos\frac{\theta}{2} |H\rangle_B + \sin\frac{\theta}{2} |V\rangle_B \big) \\
& + i |H\rangle_A |a_4\rangle_S \big( -i e^{i\phi} \cos\frac{\theta}{2} |H\rangle_B + \sin\frac{\theta}{2} |V\rangle_B \big) \Big].
\end{aligned} \qquad (4.19)$$

By observing which PD has clicked, we know in which of the four superimposed states, given in Eq. 4.19, Bob's photon has collapsed. Alice will classically communicate the result of her measurement (which PD has clicked) to Bob, who can implement the correct unitary transformation to recover the state $-\sin\frac{\theta}{2} |H\rangle_B + e^{i\phi} \cos\frac{\theta}{2} |V\rangle_B$. This state has the same coefficients as the original state $|\varphi\rangle$, hence this qubit represents the same information as the original $|\varphi\rangle$ qubit. However, while the original qubit at Alice's part was path encoded, Bob gets a polarisation encoded qubit. This charateristic was not present in the original two-photon (or three-photon) scheme, and it is a feature of our variant scheme.

| Output result in the BSM chip | Bob collapsed state | Unitary transformation to apply to Bob's state |
|:---:|:---:|:---:|
| PD1 | $-\sin\frac{\theta}{2}\left|H\right\rangle_B - ie^{i\phi}\cos\frac{\theta}{2}\left|V\right\rangle_B$ | $\lambda/2$ at $0°$ |
| PD2 | $-\sin\frac{\theta}{2}\left|H\right\rangle_B + ie^{i\phi}\cos\frac{\theta}{2}\left|V\right\rangle_B$ | $\hat{\sigma}_z \cdot \lambda/2$ at $0°$ |
| PD3 | $ie^{i\phi}\cos\frac{\theta}{2}\left|H\right\rangle_B + \sin\frac{\theta}{2}\left|V\right\rangle_B$ | $\hat{\sigma}_y \cdot \lambda/2$ at $0°$ |
| PD4 | $-ie^{i\phi}\cos\frac{\theta}{2}\left|H\right\rangle_B + \sin\frac{\theta}{2}\left|V\right\rangle_B$ | $\hat{\sigma}_x \cdot \lambda/2$ at $0°$ |

Table 4.1: For each outcome of the BSM at Alice's part, the corresponding collapsed state at Bob's part is represented. The unitary transformations that Bob needs to apply to recover the original qubit information ($\left|\varphi\right\rangle$) are also reported.

Table 4.1 reports for each possible outcome of BSM at Alice's stage the correspondent state that is collapsed at Bob's side, and the unitary transformation that Bob has to implement to recover the teleported state. The above transformations are given by:

$$T_{\lambda/2 \text{ at } 0°} = \begin{bmatrix} 1 & 0 \\ 0 & i \end{bmatrix}, \ \hat{\sigma}_x = \begin{bmatrix} 0 & 1 \\ 1 & 0 \end{bmatrix}, \ \hat{\sigma}_y = \begin{bmatrix} 0 & -i \\ i & 0 \end{bmatrix}, \ \hat{\sigma}_z = \begin{bmatrix} 1 & 0 \\ 0 & -1 \end{bmatrix},$$

and are applied on:

$$\left|H\right\rangle_B = \begin{bmatrix} 1 \\ 0 \end{bmatrix}, \ \left|V\right\rangle_B = \begin{bmatrix} 0 \\ 1 \end{bmatrix}.$$

## 4.3  A benchmark for the devices

Up to this point, we have described the ideal components that we would like to have in our quantum teleportation experiment; however, no experiment is perfect, and our fabricated components would inevitably deviate from their ideal

behaviour. This fact requires the search for a certain benchmark to which the quality of the devices can be referred to. This benchmark would be a certain figure that separates the classically explainable results from those results that can not be explained without quantum mechanics. To come out with such a figure, we need to look at the way the final experiment will be conducted.

To demonstrate the quantum teleportation of any arbitrary state, first, we need to demonstrate the teleportation of a certain complete basis on which any arbitrary state can be decomposed [16]. Any two orthogonal states of the form given in Eq. 4.2 with $\phi = 0$, which we call $|\Lambda_+\rangle$ and $|\Lambda_-\rangle$, would do the job. Second, we need to demonstrate the teleportation of a general superposition state of $|\Lambda_\pm\rangle$ with $\phi \neq 0$ [16]. In the following we refer to the teleportation of any general state $|\Lambda\rangle$, which can be $|\Lambda\rangle_+$, $|\Lambda_-\rangle$ or a superposition of $|\Lambda\rangle_+$ and $|\Lambda_-\rangle$ with $\phi \neq 0$.

In Table 4.1 we have described the unitary transformations that Bob needs to apply on his photon in order to recover the original qubit state; however, those transformations would require a fast feedforward techniques or quantum memories that are not present in our final setup. Instead, at Bob's side, we would have a verification stage consistent of polarisation rotators (waveplates) and a PBS. The Preparer tells the Verifier that he wants to prepare the state $|\Lambda\rangle$, and the Verifier sets his components in order to have the state $|\Lambda\rangle$ on one PBS output, detected with photodetector $PD_{//}$, and its orthogonal state $|\Lambda_\perp\rangle$ on the other PBS output, detected with photodetector $PD_\perp$. To do this, the Verifier has to assume a BSM result. Thus, to verify the teleportation of the state $|\Lambda\rangle$, the Verifier should have four different component arrangements, which we indicate with $A_n$, corresponding to the four different BSM results $a_n$ where n = 1, 2, 3 and 4. At this point, we must consider only those cases where Alice's BSM result $a_n$ coincides with the Verifier arrangement $A_n$, and study the threefold coincidence rates $P(a_n \cap A_n \cap PD_{//})$ for n = 1, 2, 3 and 4. These threefold coincidence rates represent the probability that Alice and Bob have the same qubit when the protocol is completed. Ideally, it should be one; however, in the real experiment, it will be less than one. Indeed, in the real experiment, Bob will obtain the same qubit as Alice with a certain *fidelity* given by the threefold coincidence rates. The bigger are the experiment non-idealities, the lower are the fidelities of the teleported qubits; however, these fidelities can not be too low because there is a certain value of the fidelity below

which the results of the experiment can be explained by a classical model. D. Boschi et al. [18] and Massar et al. [27] have shown that in such setup, the best fidelity that the Verifier can obtain without the non-local channel (thus can be explained with a classical model) is 0.75. Therefore, our benchmark is given by:

$$P(a_n \cap A_n \cap PD_{//}) = 0.75 \tag{4.20}$$

The bigger is the teleportation fidelity $P(a_n \cap A_n \cap PD_{//})$ from the benchmark value of 0.75, the more robust is our demonstration of quantum teleportation.

# Chapter 5

# State preparation chip

This chapter deals with the design and fabrication of the state preparation chip (Figure 4.2). The requirements on this chip are as follow: first, it needs to implement any arbitrary path-encoded state given by Eq. 4.2. Second, it needs to be polarisation insensitive; i.e. it needs to encode the same qubit state on the photon path regardless of the photon polarisation. Finally, the chip needs to have reasonable length and losses, and to couple well with fibre optics and the BSM chip.

In Section 5.1 we deal with the design and fabrication of the MZI structure. In Section 5.2 we deal with the development and fabrication of the resistive heaters layer. Finally, in Section 5.3 we try to predict the effects of the MZI non-idealities on the teleportation experiment.

## 5.1 Development of the Mach-Zehnder interferometer

The development of any integrated optics structure with FLM technique requires a series of preliminary fabrications to determine the optimum fabrication parameters and the adequate device geometry for the specific application. For instance, in Section 5.1.1.1 the fabrication parameters were investigated by fabricating several straight waveguides with different irradiation parameters. The process was repeated at various inscription depth, allowing us to find a good tradeoff between

losses and thermo-optical modulation. Designing the MZI geometry in Section 5.1.1.2 required: first, the fabrication of bent waveguides to find an adequate radius of curvature R for the coupler bend. Second, the fabrication of coupled straight waveguides to determine the interaction distance d. Third, the fabrication of planar couplers to find the interaction length L, and finally, trying to render the design polarisation insensitive by adopting a 3D geometry.

Sometimes problems related to the specific design may emerge; for instance, the glass non-perfectly planar surface presented additional losses problem on our shallow structures, and a depth compensation approach was used in Section 5.1.2.2. The final device was finally fabricated as described in Section 5.1.2.3.

## 5.1.1 Preliminary fabrications

### 5.1.1.1 Fabrication parameters and inscription depth

To fabricate our waveguides, we used the setup that was presented in Figure 3.1. The substrate that we used was Aluminium-Borosilicate glass (Eagle 2000, Corning Inc.), while laser focusing in the substrate was performed by 50x 0.6 NA objective. The transversal writing geometry was always used, due to its advantages that were discussed in Section 2.3.2.2. Following previous optimisations in our group, the cavity-dumped laser (see Section 3.1.1) was set at 1 MHz pulse repetition rate for the irradiation process.

The MZI structure can be fabricated at any chosen depth inside the 1 mm thick substrate of borosilicate glass. To choose an appropriate depth of fabrication, two determining factors were taken into account; namely, losses and thermo-optic effect. On one hand, the structure must be deep enough to avoid additional propagation losses due to the surface roughness and material stress near the surface. On the other hand, the structure must be shallow enough to permit a thermo-optically induced phase modulation without the need for an excessive device lengths, or an excessive, potentially damaging, power dissipation in the resistive heaters. To study the tradeoff between losses and thermo-optic effect, we studied four different inscription depths; namely, the 25, 35, 70 and 170 $\mu m$ inscription depths.

A fare waveguide losses comparison between the different inscription depths
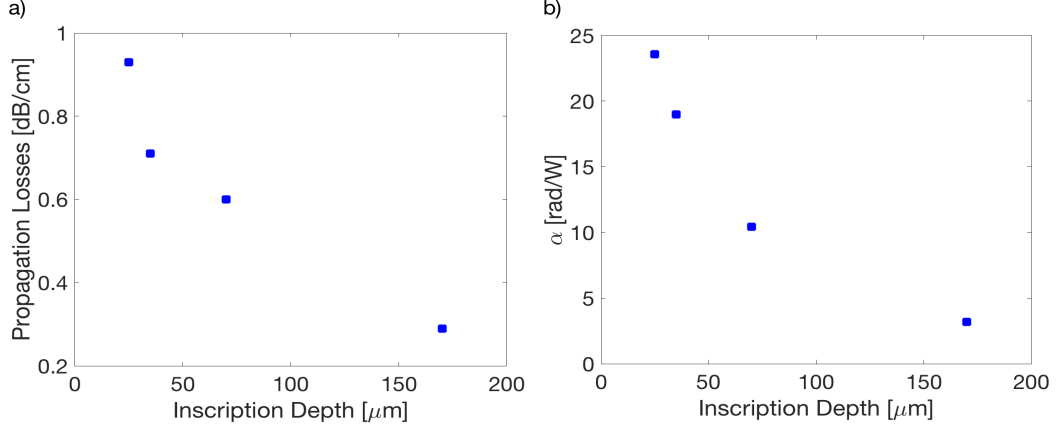
Figure 5.1: Straight waveguides at different inscription depths. (a) The best found PL in function of inscription depth. (b) The expected geometrical coefficient $\alpha$ in function of inscription depth. To obtain the expected $\alpha$, we considered the thermal model given in [64] and in Eq. 5.1 with $L_{wire} = L_{arm}$, heater placed exactly above one MZI arm, and $\rho_1 - \rho_2 = 127$ $\mu$m.

requires a preliminary study to determine the optimum fabrication parameters for each depth. This was done by exploring various inscription speeds and powers for each depth. In particular, we investigated the 20 and 40 mm/s inscription speeds, and energies per pulse from 250 up to 400 nJ by steps of 10 nJ. The optimum propagation losses for single-mode waveguides at each depth were compared and reported in Figure 5.1a.

The thermo-optically induced phase $\theta$ between the two arms of the MZI is given by $\theta = \alpha$P, where P is the power dissipated in the resistive heater and $\alpha$ is a geometry dependent parameter (measured in rad/W). To retrieve $\alpha$ for various inscription depths, we used a thermal model that was originally developed by Flamini et al. [64]. This model considers a wire-like heater with a length $L_{wire}$, two MZI arm of equal length $L_{arm}$ and distances $\rho_1$ and $\rho_2$ from the heater. The geometrical coefficient $\alpha$ is approximately given by:

$$\alpha = \frac{2n_T}{\lambda}\frac{1}{k}\frac{L_{arm}}{L_{wire}}ln\frac{\rho_1}{\rho_2}, \tag{5.1}$$

where $n_T = 1 \cdot 10^{-5}$ K$^{-1}$ is the thermo-optical coefficient, $\lambda = 1550$ nm is the wavelength, and $k = 0.9$ Wm$^{-1}$K$^{-1}$ is the thermal conductivity of the borosilicate

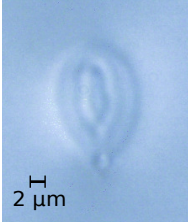| Fabrication parameters | | |
|---|---|---|
| Laser system | Yb:KYW cav. dump. | |
| Wavelength | 1030 nm | |
| Repetition rate | 1 MHz | |
| Pulse energy | 320 nJ | |
| Translation speed | 40 mm/s | |
| Objective | 0.6 NA | |

Table 5.1: Waveguide writing parameters used for building the MZI. Microscope image of the waveguide cross-section is also shown.

substrate. In our case, we take $L_{wire} = L_{arm}$; i.e., we consider the resistive heater placed exactly above one MZI arm, and we fix the horizontal distance between the two waveguides to 127 $\mu$m. Figure 5.1b shows the resulting $\alpha$ values given by Eq. 5.1 for each inscription depth under consideration.

As expected, the lowest PL were obtained for the deepest waveguides, while the highest thermo-optical modulation was obtained for the shallowest waveguides. The best CL for each inscription depth was always around 0.2 dB.

Finally, the 35 $\mu$m inscription depth was chosen, justified by the fact that the 25 $\mu$m inscription presented significant PL increase, while the 70 $\mu$m inscription depth presented a significant decrease in the $\alpha$ coefficient, but not so significant decrease in PL. The optimum fabrication parameters for our chosen 35 $\mu$m inscription depth are reported in Table 5.1. The waveguides fabricated with these optimum parameters yield PL $\sim$ 0.7 dB/cm and CL $\sim$ 0.25 dB. The mode size was about 12 x 14 $\mu$m$^2$, to be compared with the fibre mode size of 10.4 x 10.4 $\mu$m$^2$.

### 5.1.1.2 Coupler Geometry

To achieve polarisation insensitivity, we adopted the solution proposed by Sansoni et al. [69] that was shown in Figure 2.11. In their study, Sansoni et al. have demonstrated a polarisation insensitive femtosecond laser written 3D couplers, where the plane of the two coupled waveguides was tilted by an angle $\theta$. Such polarisation insensitivity can be achieved because the mode sizes of the vertical and horizontal polarisations are different. Thus there may exist a certain angle $\theta$ where the overlap integral of the two polarisations is equal, leading to equal coupling coefficients. The idea here is to achieve a polarisation insensitive MZI,

84

by building it from such polarisation insensitive 3D couplers.

To develop the 3D coupler, we need to determine five dependent parameters: the waveguide separation at the input and output, the radius of curvature R of the S-bends, the coupling distance d, the coupling region length L and the angle $\theta$. To facilitate the 3D coupler development procedure we consider the following: in a first order approximation, we can consider that the coupling between the two waveguides does not change much with the angle $\theta$; this because the distance between the two waveguides does not alter much as a function of $\theta$. Under such approximation, we can start by optimising a 2D coupler by determining its parameters. Once this is done, we can optimise the 3D coupler starting from the previously found 2D coupler parameters.

**2D coupler**   Designing a planar coupler means that we need to determine the waveguide separation at the input and output, the radius of curvature R of the S-bends, the coupling distance d, and the coupling region length L.

The waveguide separation at the input and output is determined by the final quantum teleportation experimental setup, where single photons are injected and collected with fibres separated by 127 $\mu$m.

The radius of curvature is set by a tradeoff between the bending losses BL and the total device length. To study the BL, several bends with different radiuses of curvature were fabricated; namely, the 105, 90, 75, 60 and 45 mm radiuses of curvature. For $R \geqslant 60$ mm, BL were below 0.25 dB/cm, but they increased significantly above 1 dB/cm for R smaller than 45 mm. We chose R equal to 60 mm justified by the fact that it gave a good tradeoff between losses and bend length.

To determine the coupling distance d, the following tradeoff must be considered: small d would mean bigger coupling coefficient; therefore, short couplers. However, too small d would mean that the writing of one waveguide would also influence the other, resulting probably in asymmetrical waveguides with $\beta_1 \neq \beta_2$, and the coupler fringes visibility would be compromised (see Figure 2.3b). We investigated several coupled waveguides with different coupling distances from 8 up to 14 $\mu$m. from a top-view observation with the optical microscope it is possible to distinguish the core, cladding, and the overlap of the waveguides (see Figure 5.2).
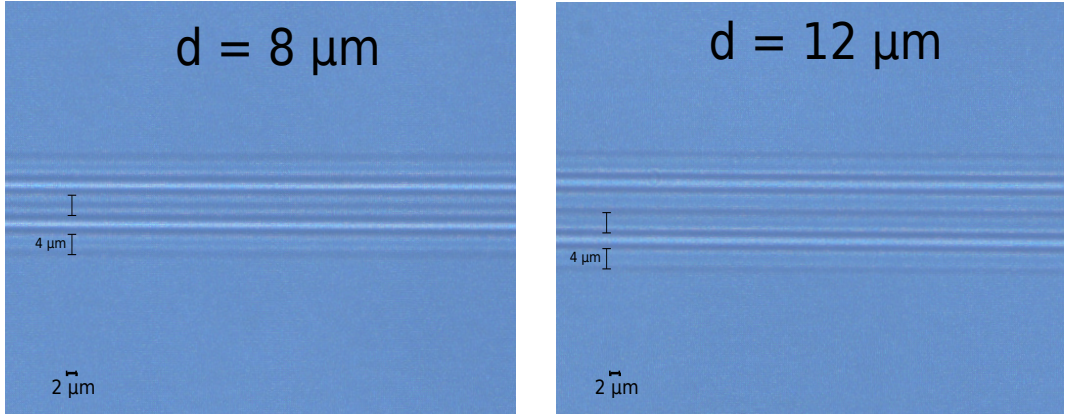
Figure 5.2: Top-view of two coupled waveguides. In the figure on the left, the coupling distance is 8 $\mu$m, and a big overlap between the claddings is obvious. In the figure on the right, the coupling distance is 12 $\mu$m, and the two claddings are barely touching.

We chose the $d = 12$ $\mu$m justified by the fact that it was the coupling distance where the two cladding of the waveguides were barely starting to overlap.

To find the shortest coupling length that gives a balanced coupler $L_{50/50}$, we did a "length-scan approach" by fabricating several couplers, progressively increasing the coupling length L. The devices are characterised, and the splitting ratios as a function of L are plotted and fitted with the coupler equations as reported in Figure 5.3a. $L_{50/50} = 1.5$ mm was then extrapolated from the fitting.

**3D Coupler** Having designed a balanced planar coupler, the next step is to render it polarisation insensitive by introducing a 3D geometry. For this aim, we use the same R, d and $L_{50/50}$ from the planar design, and introduce various angles $\theta$ (see Figure 2.11). For each angle $\theta$, we characterise the splitting ratios of both the vertical and horizontal polarisations. Figure 5.3b reports the ratio between the vertical and horizontal coupling coefficients as a function of the tilt angle $\theta$. The polarisation insensitivity is predicted to be around $\theta = 68°$ where the ratio is almost unitary. At $L_{50/50}$, the difference between the vertical and horizontal transmissions ($T_V - T_H$) was 10% in the case of a planar coupler, and it decreased to 4% for a 3D coupler with a tilt angle $\theta$ of 68°. Having changed the
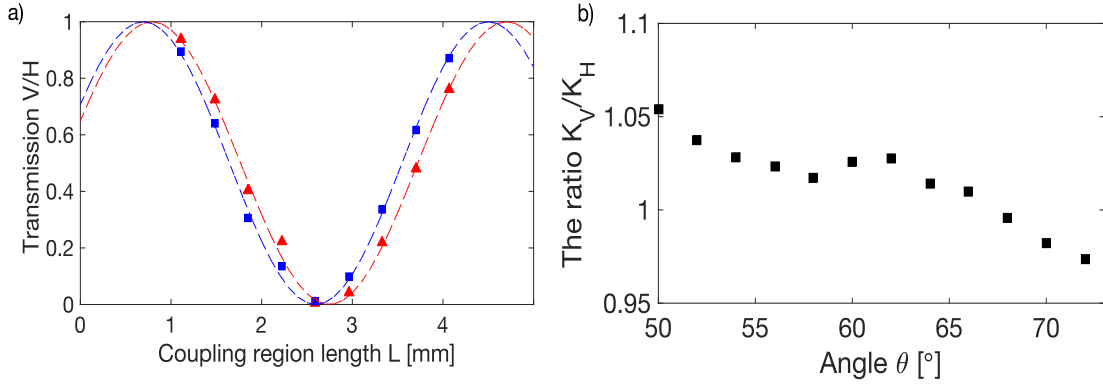
Figure 5.3: (a) Planar couplers with different coupling lengths L. The vertical (red) and horizontal (blue) polarisations are reported. The squares and triangles represent actual couplers, while the dashed lines represent the fitting with the coupler equation. From the fitting, it is possible to predict the length of the balanced coupler $L_{50/50}$ at about 1.5 mm. (b) Scanning the angle of a 3D coupler to find the best polarisation insensitivity. We observe minima in the polarisation sensitivity around 68°.

coupler geometry from 2D to 3D, keeping the same parameters, the $L_{50/50}$ changes slightly. By performing another length scan approach with the 3D couplers, the new $L_{50/50}$ was found to be as 1.6mm.

## 5.1.2 MZI fabrication

### 5.1.2.1 MZI geometry

A schematic representation of the MZI chip that we want to fabricate was reported in Figure 4.2. What determines the MZI geometry is its two couplers, which we already developed in the previous section, and its arms. We have two pairs of arms: the ones between the two couplers and the ones at the output, which we also call the $\theta$ and the $\phi$ arms respectively. The arms separation is taken as our standard 127 $\mu$m separation. The $\phi$ arms and the $\theta$ arms are fabricated at the same depth, and their lengths are taken as 5 mm and 10 mm respectively. The reason for this choice is determined by the resistive heaters and will be explained in Section 5.2.1. Considering the two couplers and the two pairs of arms, the overall MZI length is 35 mm.

87
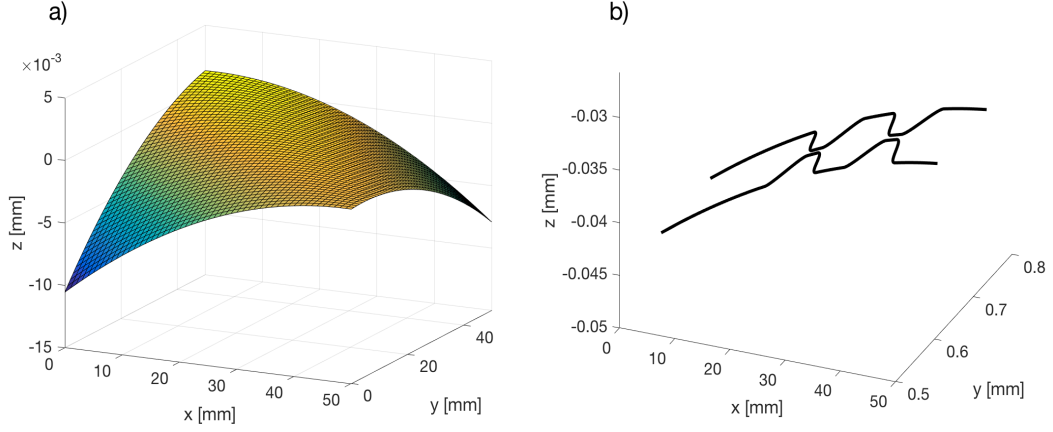
Figure 5.4: (a) An example of a surface curvature of 50 x 50 mm² Eagle 2000 substrate glass. (b) A depth correction applied on a planar MZI structure forcing it to follow the surface curvature of the glass.

### 5.1.2.2 Compensating for surface curvature

To fabricate the 35 mm-long MZI structure, we used the available 50 x 50 mm² Eagle 2000 substrate. Waveguides written on such a large substrate appeared to have increased losses with respect to ones written on smaller substrates. These additional losses were attributed to possible disturbances on the MZI shallow structure induced by the surface curvatures. By reducing the power of the laser beam used for the fabrication, we can observe the glass surface by collecting the back-reflected light without inducing material modification. By finding the optimum focus on the glass surface in various mesh points along x and y, the surface curvature was extrapolated. We observed depth variation in the surface curvature up to 15 $\mu$m. To correct for such surface curvature, we fitted the surface curvature with a polynomial expression of second degree (see Figure 5.4a) and used this model to correct the depth coordinate (z) of the fabricated devices. In this way, the fabricated devices were forced to follow the surface curvature. Figure 5.4b reports an example of such surface correction applied on a planar MZI structure.

| chosen MZI devices | | | | | |
|---|---|---|---|---|---|
| Device number | Interaction length L | Device structure | Splitting ratio V | Splitting ratio H | Insertion losses IL |
| 1 | 1.580 mm | dummy coupler | 52/48 | 0.54/0.46 | 5 dB |
| | | MZI | 0.05/0.95 | 0.05/0.95 | 6.5 dB |
| 2 | 1.608 mm | dummy coupler | 51/49 | 0.49/0.51 | 5.2 dB |
| | | MZI | 0.04/0.96 | 0.04/0.96 | 6.7 dB |

Table 5.2: The characterisation of two MZI devices that showed best performance, out from the 11 devices that were fabricated in a length scan approach.

### 5.1.2.3 MZI devices

Once we have all the parameters from the design phase, the final MZI structure can be fabricated. To compensate for process variability, we performed a further length-scan approach; i.e. we fabricated several MZI devices that differ one from the other by small interaction length L variation around the previously found $L_{50/50}$. In this way, any process variations will be translated in $L_{50/50}$ variation. There is no way to know if the single coupler in the MZI structure is actually 50/50 or not. To overcome this limitation, the strategy adopted is to fabricate a dummy coupler near each MZI with the same L as the actual couplers inside the MZI. By neglecting the fabrication process statistical variations that occur between the MZI and the neighbouring dummy coupler, we can assume that the dummy coupler behaves exactly like the couplers inside the MZI. Once a good 50/50 dummy coupler is found, the corresponding MZI is characterised. If this MZI is actually made from two 50/50 couplers, and the passive phase difference $\theta_0$ between the first two arms is almost zero, then all the power in the MZI output would be on the cross port (see Eq. 2.15).

11 MZI were fabricated, scanning the L from 1.58 up to 1.86 mm. The characteristics of the best two devices (L= 1.580 and 1.608 mm) are reported in Table 5.2.

| Resistances parameters | | |
| --- | --- | --- |
| | $R_\theta$ | $R_\phi$ |
| Width | $200\mu m$ | $200\mu m$ |
| Thickness | 50nm | 50nm |
| Length | 5mm | 7mm |
| Experimental resistance | $44\Omega$ | $72\Omega$ |

Table 5.3: The resistors parameters of the Mach-Zehnder interferometer resistive heaters.

## 5.2  Active control with heaters

Having fabricated and characterised the passive MZI devices, the structure is made reconfigurable by depositing and patterning metallic resistors on the sample surface. The resistors will thermo-optically modulate the refractive index of the waveguides underneath, leading to relative phase accumulation between the MZI arms.

### 5.2.1  Resistors pattern design

The heaters are realised with a gold layer, while the bondings are performed with a polymeric conductive paste. A big resistance value is desirable since it means that most of the power would be dissipated in the resistors and only small fraction in the fragile polymeric bondings and the wires. For this aim, a long and narrow rectangular resistor above the MZI arm is desired. A long resistor would also mean less power per unit of area to achieve the same $\alpha$ (Eq. 5.1), thus avoiding possible resistors damage due to excessive heating. Nevertheless, we do not want too long heaters, because this would mean long MZI arm, and consequently a significant increase in IL due to the increase in waveguide length. Additionally, the resistor width should not be too narrow to avoid possible undesired interruption in the resistive layer. We chose a width of 200 $\mu$m, and 5 mm and 7 mm lengths for the $\theta$ and $\phi$ resistances respectively. The $\phi$ heater was made a slightly longer because it needs to induce more phase shift compared to the $\theta$ heater. The resistors parameters are reported in Table 5.3.

A 50 nm gold layer was deposited on the substrate surface using a sputter coater (Cressington 108auto). The resistors pattern was defined by laser ablation,

which was done by focusing on the sample surface the same femtosecond laser beam used for waveguide inscription. The translation speed used for ablation was 1 mm/s, while the energy per laser pulse was 80 nJ. To define the resistors pattern and guarantee electrical isolation between the contacts, each isolating line was fabricated by five successive ablation lines, each offset by 500 nm.

Figure 5.5 shows a top-view schematic of the heaters design. The black lines are the two MZI realised at 35 $\mu$m underneath the surface. The yellow colour represents the surface deposited gold. The white lines are the ablation lines that are needed to define the resistors $R_\theta$ and $R_\phi$ and the electrical pads A, B and C.

Instead of controlling each MZI separately, which would require six independent electrical pads/contacts, we decided to connect the resistors in parallel ($R_{\theta 1}//R_{\theta 2}$ and $R_{\phi 1}//R_{\phi 2}$). In this way, we can control both structures with only three electrical contacts A, B and C. The contacts are realised by bonding a copper wire with an electrically conductive polymeric paste. This bonding paste is fragile; therefore, we decided to replicate each contact, creating a backup contact in case of contact failure. The red circles represent the position where the wire bonding is done.

By using Eq. 5.1, it is possible to simulate the resistors position that will give the maximum $\alpha$. It turns out that the optimum position to place the resistors is not directly above the MZI arms, but in a slightly shifted position away from the two arms as seen in Figure 5.5.

## 5.2.2 Characterisation of the active phase shifters

Figure 5.6 shows a simulation of the MZI splitting ratios, where the MZI was made from two non-ideal couplers with splitting ratios equal for those of the dummy coupler in device 1 from Table 5.2. The MZI is not affected much by the fact that its two couplers are not perfectly balanced; indeed, as also discussed in Section 2.1.4, the MZI shows a robustness to variation in its couplers splitting ratios. The MZI behaviour depends mainly on the relative phase $\theta$ that is accumulated in the arms. Given this, to recover the relative $\theta$ phase, we can use the ideal MZI
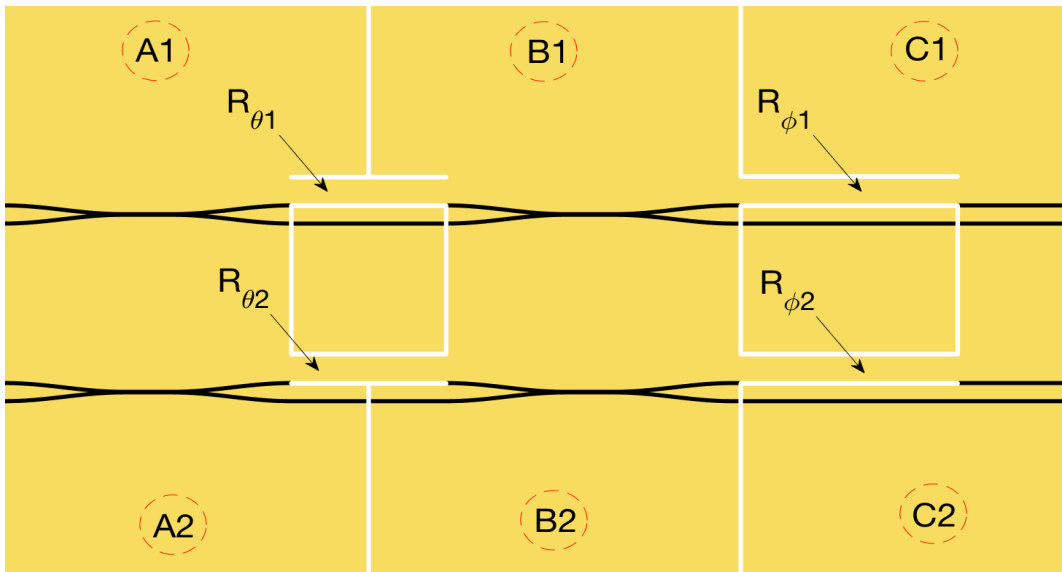
Figure 5.5: Top-view schematic of the glass with the fabricated MZI structures. The glass footprint is 2.5 x 3.7 cm². The black lines represent the two chosen MZI, which were fabricated at 35 $\mu$m bellow the glass surface. The yellow colour represents the 50 nm sputtered gold layer. The white lines represent the ablation pattern, which drives four resistors R that work as heaters, and three electrical pads A, B and C. The red circles present the place where the electrical bonding are done. On each electrical pad, two bondings (the subscripts 1 and 2) were done, achieving a backup wire in case the fragile polymeric bonding is damaged.

Figure 5.6: Non-ideal MZI simulation. A simulation of the splitting ratio on the transmission port of a MZI built from two non-ideal couplers with splitting ratios of 52/48 and 0.54/0.46 for the vertical and horizontal polarisations respectively. Red and blue represent the vertical and horizontal polarisations respectively.

equations given by:

$$
\begin{aligned}
R &= \sin^2\left(\theta/2\right), \\
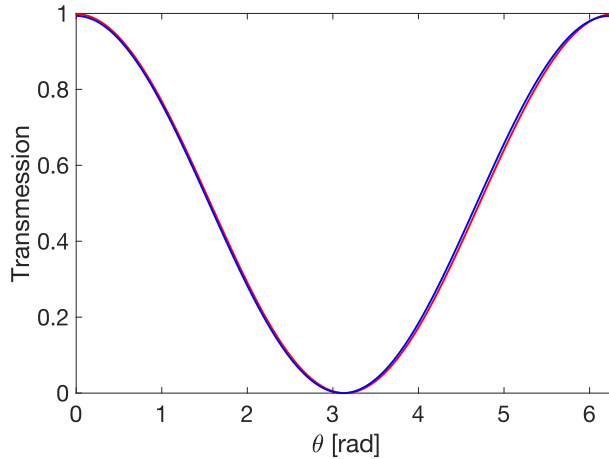T &= \cos^2\left(\theta/2\right).
\end{aligned}
\tag{5.2}
$$

The relative phase $\theta$ as a function of the dissipated power on $R_\theta$ is reported in Figure 5.7a. We can see that by dissipating from 0 up to 0.55 W about 2.5 rad phase accumulation is achieved. The induced phase per unit of power is almost the same value of 4.4 rad/W for the two polarisations. A similar behaviour as the one in Figure 5.7a was obtained for both MZI realisations from Table 5.2. By simulating non-ideal MZIs, the behaviour in Figure 5.7a can be replicated only if we introduce different initial relative phases $\theta_0$ for the two polarisations. More precisely, it is necessary to introduce a $\theta_{V0} - \theta_{H0}$ of about 0.2 rad. An equal initial relative phase $\theta_0$ for the two polarisations can be obtained if the MZI arms have the same birefringence, but different geometrical length due to fabrications tolerances. While different initial relative phases $\theta_0$ for the two polarisations means that there is a difference in the birefringence of the two arms. Considering $\theta_{V0} - \theta_{H0} = 0.2$ rad, the arms geometrical length and our working
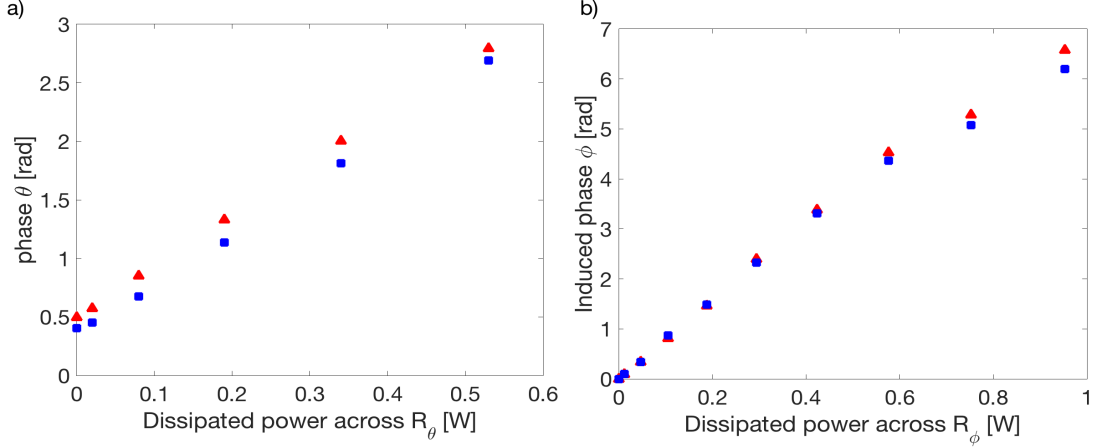
Figure 5.7: The phase in function of the power dissipated on the $\theta$ resistor (a), and the induced phase by the $\phi$ resistor (b). Vertical and horizontal polarisations are represented with red and blue circles respectively.

wavelength of 1550 nm, such difference in the birefringence is estimated to be about $1 \cdot 10^{-5}$. This value needs to be compared with our waveguides birefringence values which are on the order of $10^{-5}$. The origin of such difference in the MZI arms birefringence can be attributed to the fact that some part of the MZI arms is made from the couplers bends, which were fabricated at different depth in a 3D fashion. Such depth dependent birefringence value is not strange; indeed, optimising the fabrication depth in Section 5.1.1.1, we have observed that the waveguides characteristics were depth dependent.

To characterise the induced $\phi$ phase, a Young interference (double-slit) experiment was performed, where the two slits are replaced by the two MZI outputs. To characterise the relative induced phase $\phi$ for each dissipated power on $R_\phi$, it is enough to acquire the far-field interference profile by a CCD camera and perform an FFT algorithm on it to retrieve the relative phases between the images. An example of such interference profile is reported in Figure 5.8. The induced phases for the two polarisations is almost equal, except at relatively high power where $\Delta\phi = \phi_V - \phi_H$ is about 0.4 rad. Such difference between the two polarisations at relatively high power may be due to different thermo-optical coefficients at high temperature.
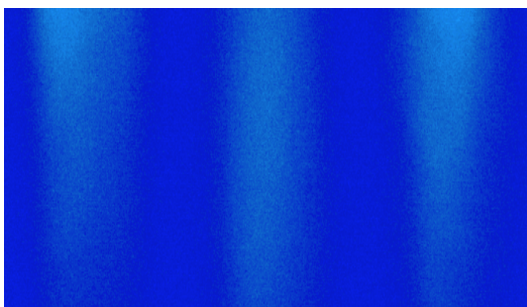
Figure 5.8: An example of an interference pattern acquired on the CCD camera in a Young interference experiment that was used to retrieve the induced phase $\phi$ at the MZI output.

Fitting linearly the experimental data in Figure 5.7, the experimental $\alpha$ coefficient can be obtained as the slope of the fittings. The obtained $\alpha$ coefficients for the $\theta$ and $\phi$ resistances were 4.4 rad/W and 7.85 rad/W respectively. These values differ from the predicted value of 18 rad/W that was obtained by using Eq. 5.1. We attributed this difference due to the fact that Eq. 5.1 is merely an approximative model, and to possible misalignments between the resistors and the MZI arms.

## 5.3 Quantum teleportation experiment with non-ideal MZI

Ideally, the state preparation chip should prepare the same path-encoded state regardless of the incoming photon polarisation. We tried to minimise the polarisation dependency of the MZI structure; nevertheless, some polarisation dependency is still present. In the following, we try to understand the effect of such non-ideal MZI on the quantum teleportation experiment.

The break of degeneracy between the two orthogonal polarisations, results in two MZI matrixes, one for each polarisation:

$$
T_{MZI}^V = \begin{bmatrix} -\sin\frac{\theta_V}{2} & \cos\frac{\theta_V}{2} \\ e^{i\phi_V}\cos\frac{\theta_V}{2} & e^{i\phi_V}\sin\frac{\theta_V}{2} \end{bmatrix}, \quad T_{MZI}^H = \begin{bmatrix} -\sin\frac{\theta_H}{2} & \cos\frac{\theta_H}{2} \\ e^{i\phi_H}\cos\frac{\theta_H}{2} & e^{i\phi_H}\sin\frac{\theta_H}{2} \end{bmatrix}. \quad (5.3)
$$

Following what was done to retrieve Eq. 4.10, the state at the output of the first chip can be written as:

$$|\psi\rangle_{chip1}^{non-ideal} = \frac{1}{\sqrt{2}} \Big[ |H\rangle_B |V\rangle_A \Big( -\sin\frac{\theta_V}{2} |1\rangle_S + e^{i\phi_V}\cos\frac{\theta_V}{2} |2\rangle_S \Big) -$$
$$|V\rangle_B |H\rangle_A \Big( -\sin\frac{\theta_H}{2} |1\rangle_S + e^{i\phi_H}\cos\frac{\theta_H}{2} |2\rangle_S \Big) \Big]. \tag{5.4}$$

In analogue to Eq. 4.10 we can say that the Preparer ideally would like to prepare the state:

$$|\varphi\rangle_A^{ideal} = -\sin\frac{\theta}{2} |1\rangle_S + e^{i\phi}\cos\frac{\theta}{2} |2\rangle_S, \tag{5.5}$$

instead, he will be preparing one of the following two states:

$$\begin{cases} |\varphi\rangle_{A1}^{non-ideal} = -\sin\frac{\theta_V}{2} |1\rangle_S + e^{i\phi_V}\cos\frac{\theta_V}{2} |2\rangle_S, & \text{if Alice's photon is V.} \\ |\varphi\rangle_{A2}^{non-ideal} = -\sin\frac{\theta_H}{2} |1\rangle_S + e^{i\phi_H}\cos\frac{\theta_H}{2} |2\rangle_S, & \text{if Alice's photon is H.} \end{cases} \tag{5.6}$$

Note that the Preparer can not know which one of the above two state he has prepared because the polarisation of photon A is in an entanglement state and its polarisation is not defined.

In analogy to Eq. 4.14, Eq. 5.4 can be re-written as:

$$\begin{aligned} |\Psi\rangle_{chip1} = \frac{1}{2} \Big[ &|\mathbf{\Psi}^-\rangle_{AS}\Big( -\sin\frac{\theta_V}{2} |H\rangle_B - ie^{i\phi_H}\cos\frac{\theta_H}{2} |V\rangle_B \Big) \\ &+ |\mathbf{\Psi}^+\rangle_{AS}\Big( -\sin\frac{\theta_V}{2} |H\rangle_B + ie^{i\phi_H}\cos\frac{\theta_H}{2} |V\rangle_B \Big) \\ &+ |\mathbf{\Phi}^-\rangle_{AS}\Big( ie^{i\phi_V}\cos\frac{\theta_V}{2} |H\rangle_B + \sin\frac{\theta_H}{2} |V\rangle_B \Big) \\ &+ |\mathbf{\Phi}^+\rangle_{AS}\Big( -ie^{i\phi_V}\cos\frac{\theta_V}{2} |H\rangle_B + \sin\frac{\theta_H}{2} |V\rangle_B \Big) \Big]. \end{aligned} \tag{5.7}$$

From Eq. 5.7 we see that, up to proper unitary transformation, the qubit teleported to Bob taking into account the non-ideal MZI is:

$$\begin{cases} |\varphi\rangle_{B1}^{non-ideal} = \Big( -\sin\frac{\theta_V}{2} |H\rangle_B + e^{i\phi_H}\cos\frac{\theta_H}{2} |V\rangle_B \Big)\frac{1}{\sqrt{\sin^2\frac{\theta_V}{2}+\cos^2\frac{\theta_H}{2}}}, & \text{if } |\Psi^\pm\rangle_{AS} \text{ is detected.} \\ |\varphi\rangle_{B2}^{non-ideal} = \Big( -\sin\frac{\theta_H}{2} |H\rangle_B + e^{i\phi_V}\cos\frac{\theta_V}{2} |V\rangle_B \Big)\frac{1}{\sqrt{\sin^2\frac{\theta_H}{2}+\cos^2\frac{\theta_V}{2}}}, & \text{if } |\Phi^\pm\rangle_{AS} \text{ is detected.} \end{cases} \tag{5.8}$$
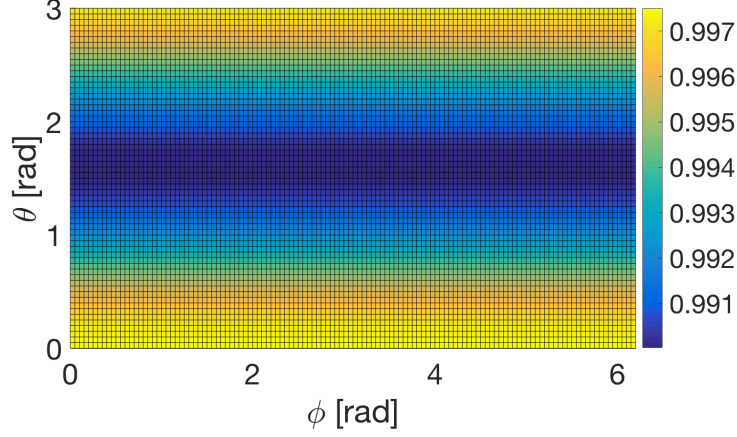
Figure 5.9: Simulation of the teleportation fidelity for non-ideal MZI with the worst values of $\Delta\theta = \theta_V - \theta_H = 0.2$ rad and $\Delta\phi = \phi_V - \phi_H = 0.4$ rad. The obtained teleportation fidelity is always above 0.99.

The Preparer and the Verifier will think only in term of $\theta$ and $\phi$, thus preparing and projecting on ideal states $|\varphi_A^{ideal}\rangle$ and $|\varphi_B^{ideal}\rangle$. We consider the case where for each combination of dissipated powers on the MZI resistors, the Preparer will be creating the ideal state $|\varphi_A^{ideal}\rangle$ with $\theta = \frac{\theta_V + \theta_H}{2}$ and $\phi = \frac{\phi_V + \phi_H}{2}$. The Verifier would be projecting on $|\varphi_B^{ideal}\rangle = |\varphi_A^{ideal}\rangle$, and the real quantum teleportation fidelity is given by:

$$P = |\langle\varphi_B^{ideal}||\varphi_B^{non-ideal}\rangle|^2. \tag{5.9}$$

we can simulate Eq. 5.9 with $\theta_{V/H} = \theta \pm \frac{\Delta\theta}{2}$ and $\phi_{V/H} = \phi \pm \frac{\Delta\phi}{2}$ where $0 \leqslant \theta \leqslant \pi$, $0 \leqslant \phi \leqslant 2\pi$ and $\Delta\theta$ and $\Delta\phi$ are taken as the worst case from Figure 5.7; namely, $\Delta\theta = 0.2$ rad and $\Delta\phi = 0.4$ rad. Such simulation is reported in Figure 5.9, according to which the teleportation fidelity remains above 0.99.

# Chapter 6

# Path-polarisation Bell state measurement chip

This chapter deals with the realisation of the 50/50 beam splitter (BS3) and the polarising beam splitters (PBS1 and PBS2) in the Bell-State Measurement (BSM) chip (see Figure 4.3). The polarisation sensitivity should be maximised in the half waveplate (HWP) and the polarising beam splitters (PBS1 and PBS2); while minimised in the balanced beam splitter (BS3). Such opposite requirements are both made possible with femtosecond laser writting technique, by correctly tailoring the devices geometry and fabrication parameters.

The fabrication of the HWP is based on the technique that was developed by Corrielli et al. [71] and explained in Section 2.4.2. Such technique requires the use of an objective with very high NA, which can be achieved only with oil-immersion objectives. Inscribing the BSM chip entirely with such objective would significantly complicate the fabrication process. We choose to divide the BSM chip into two separate chips; one for the HWP fabricated with an oil-immersion objective, and a second for BS3 and the PBSs, which are fabricated with a dry 50x 0.6NA objective. A schematic representation of the resulting BSM chip is given in Figure 6.1.

Section 6.1 is dedicated to the development and realisation of the PBS. In Section 6.2 we develop a novel approach for obtaining a polarisation insensitive beam splitter which is also used to make BS3. Section 6.3 deals with integrating
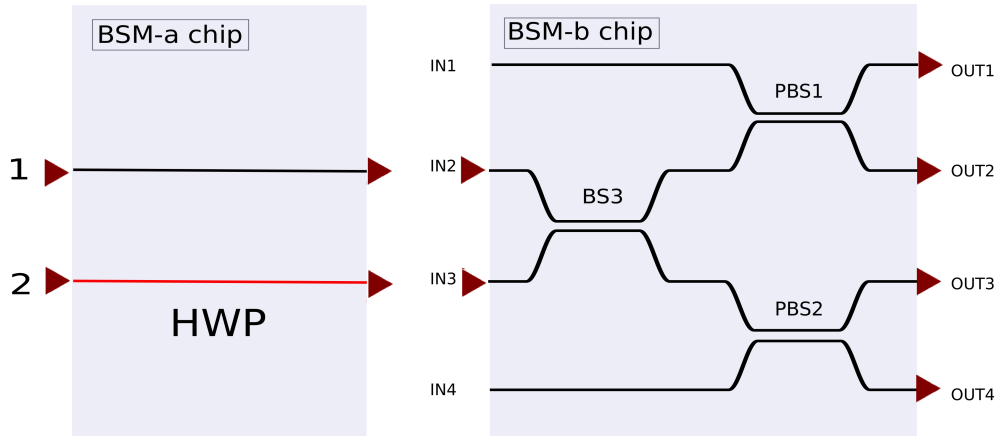
Figure 6.1: The BSM chip from Figure 4.3 is split into two chips permitting an easier fabrication approach. BSM-a chip contains a straight waveguide in path 1 (black line), and an integrated half waveplate (HWP) in path 2 (red line). BSM-b chip contains the polarisation insensitive beam splitter (BS3), and the two polarising beam splitters (PBS1 and PBS2). IN1 and IN4 are not used in the final quantum teleportation experiment; nevertheless, they permit an independent access to the PBS, useful in the device characterisation phase.

BS3 and the PBSs on one chip, and finally, Section 6.4 deals with the effects of our non-ideal components on the quantum teleportation experiment.

## 6.1 The polarising beam splitter (PBS)

### 6.1.1 How to build a PBS

By fitting the splitting ratios as a function of the coupling length $L$ with the directional coupler equations (Eq. 2.8), the relevant parameters of the directional coupler are retrieved. These parameters are the contribution of the bent segments, represented by $L_{eff}$, and the coupling coefficient $k$. They are generally different for the two orthogonal polarisations V and H due to waveguide birefringent (see Section 2.4.1). In particular, different coupling coefficients $k_V$ and $k_H$ mean that the period of the power bouncing between the two waveguides is different. Thus, there should be a certain interaction lengths $L$ where the beating of the two polarisations is in anti-phase with a good approximation. We call such length

99

by $L_{PBS}$ because at $L = L_{PBS}$ it is possible to separate the two polarisations completely; one on the cross, and the other on the bar, therefore achieving a PBS effect.

The condition to obtain a PBS can be obtained from Eq. 2.8 and Eq. 2.11. If we consider the transmission port, then this condition is given by:

$$\begin{cases} T_V = \sin^2\left(k_V \cdot L_{PBS}\right) = 1 \\ T_H = \sin^2\left(k_H \cdot L_{PBS}\right) = 0 \end{cases} \quad or \quad \begin{cases} T_V = \sin^2(k_V \cdot L_{PBS}) = 0 \\ T_H = \sin^2(k_H \cdot L_{PBS}) = 1 \end{cases} \tag{6.1}$$

Elaborating Eq. 6.1, $L_{PBS}$ can be obtained as:

$$L_{PBS} = \frac{\pi}{2|k_V - k_H|}. \tag{6.2}$$

### 6.1.2 A figure of merit for the PBS

An ideal PBS would satisfy Eq. 6.1, thus, separating the two polarisations completely. However, as the case for any real device, an exact experimental fulfilment of such mathematical condition is virtually impossible. To measure the degree of deviation of a real PBS from the ideal PBS, we introduce the following parameter:

$$\begin{aligned} ER_T &= \left|10 \cdot log_{10}\left(\frac{T_V}{T_H}\right)\right| = \left|T_{V\ dB} - T_{H\ dB}\right|, \\ ER_R &= \left|10 \cdot log_{10}\left(\frac{R_V}{R_H}\right)\right| = \left|R_{V\ dB} - R_{H\ dB}\right|, \end{aligned} \tag{6.3}$$

where $ER_T$ and $ER_R$ represents the extinction ratios expressed in dB on the transmission (cross) and reflection (bar) ports respectively.

### 6.1.3 Development of the PBS

To develop the PBS, we start by a series of theoretical considerations that will give us a guideline on what to look for in order to achieve a good PBS. This is followed by a first phase of preliminary fabrications of straight waveguides to determine the optimal fabrication parameters. Those parameters are then used in

a second phase of preliminary fabrications aiming to optimise the PBS geometry, leading finally to the fabrication of the PBS itself.

### 6.1.3.1 Preliminary considerations

**The coupling length** The coupling length $L$ influences the device robustness. This affirmation can be shown in the follow: considering two coupled waveguides, any fluctuations in the fabrication parameters or the geometry is translated in $k$ fluctuations. The influence of $k$ variation on the splitting ratio can be studied by deriving the splitting ratios with respect to $k$. For instance, If we consider the splitting ratio on the transmission port $T$, then:

$$\frac{\partial T}{\partial k} = L \sin(2kL). \tag{6.4}$$

The PBS conditions given in Eq. 6.1 implies that $\sin(2kL) = 0$, thus $\frac{\partial T}{\partial k}$ is zero. However, fabricating a coupler that satisfies such condition exactly is virtually impossible. Therefore, in a real case, $\frac{\partial T}{\partial k} \neq 0$ and the coupler sensitivity to $k$ variation increases with the coupling length $L$. Accordingly, a short coupling distance is desired not only because it implies fewer insertion losses, but also because it results in a superior robustness to fabrication tolerances. From Eq. 6.2 we see that to obtain a shorter coupler, we need to maximise the difference between the two coupling coefficients.

**The coupling distance** To determine the coupling distance $d$, a first consideration is its effect on the design robustness. The coupling distance determines the coupling coefficient. It was found, also experimentally [76] that the coupling coefficient depends exponentially on the coupling distance; i.e. we can write:

$$k = C_1 \cdot e^{-d \cdot C_2} \tag{6.5}$$

To understand how $k$ fluctuations depend on $d$, we need to investigate the relative variation of $k$ with respect to $d$:

$$\frac{1}{k}\frac{\partial k}{\partial d} = -C_2. \tag{6.6}$$

This equation does not depend on $d$; thus the effect of fabrication errors is always the same for any $d$.

A second consideration to be taken into account when choosing $d$ is its effect on the extinction ratios given in Eq. 6.3. If $d$ is too small, then the writing of one waveguide may influence the other, creating two asymmetrical waveguides with different propagation constants $\beta_1$ and $\beta_2$. In such conditions, the power beating is that of an asymmetrical coupler given in Eq. 2.9. From those expressions, it is possible to appreciate that for the asymmetrical coupler the transmission splitting ratios can reach 0 but not 1, while the reflection splitting ratios can reach 1 but not 0. Such behaviour was also depicted in Figure 2.3b. Being defined as a ratio, what matters to the ER is the achievement of the 0; therefore, such asymmetrical behaviour will lead to a significant reduction in ER especially on the reflection port. For these reasons, a good PBS would require us to avoid such asymmetry by avoiding waveguide overlapping in the coupling region.

The last consideration that needs to be taken into account is the dependence of the PBS length $L_{PBS}$ on the waveguide separation. As shown in the last paragraph, a shorter coupling length is desirable because it will give a more robust structure. Therefore, according to Eq. 6.2 we need to find the coupling distance $d$ that gives the biggest $|k_V - k_H|$. This means we need to recover the $C_1$ and $C_2$ coefficients in Eq. 6.5 for the V and H polarisation. While solving such a problem in lithographic optical circuits can also be achieved with simulations, in the case of FLM waveguides the refractive index profile is too complex to be reliably simulated. Thus, the most effective way to study the $|k_V - k_H|$ dependence on $d$ is to investigate it experimentally as done in Section 6.1.3.3.

### 6.1.3.2 Optimising the fabrication parameters

The substrate, focusing optics, laser pulses wavelength and repetition rate are kept the same as for the MZI described in Section 5.1.1.1, as also reported in Table 6.1. In the present case, the most relevant parameters to take into account for the optimisation are losses. Therefore we chose the 170 $\mu$m inscription depth since it gave low propagation and coupling losses from the previous characterisation in the MZI section (see Figure 5.1a). At this depth, an exploration of the remaining

fabrication parameters, namely, inscription power and speed, was done by investigating three inscription speeds: 10, 20 and 40 mm/s, and inscription powers from 250 up to 400 mW by steps of 10 mW. Figure 6.2a reports the measured PL as a function of the explored fabrication parameters for single-mode waveguides. The combination 370 mW and 40 mm/s gave the lowest PL.

The modes in our FLM written waveguides are elliptical, we indicate by x and y the mode sizes in the direction parallel and perpendicular to the inscribing laser beam respectively. It is interesting to check for differences in the mode sizes between the vertical (V) and horizontal (H) polarisations that are obtained with each one of our investigated inscription parameters. This is because a significant difference between the V and H mode sizes will mean a significant difference in the overlap integral, which in turn mean bigger $|k_V - k_H|$ value and thus shorter and more robust couplers. In particular, Figure 6.2b shows the ratios $x_V/x_H$ and $y_V/y_H$ as a function of the inscription parameters, where the subscripts V and H stand for the vertical and horizontal polarisations respectively. High ratios can be appreciated with the combination 320 mW and 40 mm/s, which indicate that such combination may have big $|k_V - k_H|$.

Thus, we have one combination which is favourable in term of losses, and another in term of design robustness. Both combinations were studied. The parameters of fabrication are summarised in Table 6.1. The combination with 370 mW inscription power gave straight waveguides with PL of ∼0.3 dB/cm, mode size for the vertical and horizontal polarisations of 15.5 x 15.7 $\mu$m$^2$ and 15.1 x 15.6 $\mu$m$^2$ respectively, and average CL of ∼0.37 dB. The combination with 320 mW inscription power gave straight waveguides with PL of ∼0.45 dB/cm, mode size for the vertical and horizontal polarisations of 16.3 x 16.7 $\mu$m$^2$ and 14.7 x 14.6 $\mu$m$^2$ respectively, and average CL of ∼0.5 dB.

### 6.1.3.3 Optimising the geometry

The distance between the waveguides at the device input and output is taken as 127 $\mu$m to couple with the previous chip and to match the standard pitch of fibre arrays. The optimisation of the rest of the geometrical parameters is described in this section.
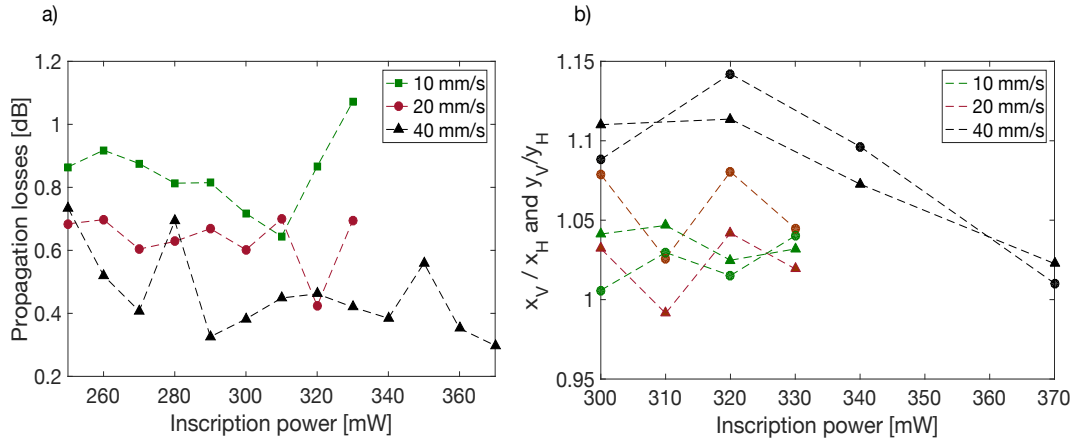
Figure 6.2: Determining the inscription power and speed. (a) Propagation losses. (b) The ratio $x_V/x_H$ (circles) and $y_V/y_H$ (rectangles).

| Fabrication parameters | |
| --- | --- |
| Laser system | Yb:KYW cav. dump. |
| Wavelength | 1030 nm |
| Repetition rate | 1 MHz |
| Pulse energy | 370 nJ and 320 nJ |
| Translation speed | 40 mm/s |
| Objective | 0.6 NA |

Table 6.1: Waveguide writing parameters used for building the PBS. We used to combinations that differ one from the other only by the pulse energy.

**The S-bend radius of curvature**   To determine the directional coupler S-bend radius of curvature, using the above-determined fabrication parameters; we characterised bending losses for 120, 90, 60 and 45 mm radiuses of curvature. R = 90 mm was chosen since it gave a reasonable tradeoff between bend length and bend losses. The obtained BL were $\sim 0.4$ dB/cm.

**The coupling distance**   Using the above-determined fabrication parameters different coupling distances were investigated; namely, the 9.5, 11, 12.5 and 14 $\mu$m coupling distances. For each $d$, we scanned several coupling lengths in the 0-$L_{end}$ range, where $L_{end}$ was chosen in a way to give at least one beating in the splitting ratios curves, permitting a good fitting with the coupler equation. From the fitting, the coupling coefficients for the V and H polarisation were extracted and plotted in Figure 6.3a. The experimental data in Figure 6.3a were fitted with the exponential expression given in Eq. 6.5. Such fitting has highlighted the existence of an inversion in the coupling coefficient: at $d = 10$ $\mu$m the quantity $k_H - k_V$ was equal to zero, but it became positive and negative at bigger and smaller $d$ respectively. Figure 6.5b reports the expected value of $|k_V - k_H|$ at any given $d$. One may think that it is convenient to choose a very small $d$ in order to achieve a superior coupler in terms of robustness by minimising $L_{PBS}$ (see Eq. 6.2). Nevertheless, a top-view observation with the optical microscope has shown the existence of a significant overlap in the two coupled waveguides claddings for $d$ bellow 11 $\mu$m. Such overlap would cause waveguides asymmetry, putting at risk our high ER requirement. In the light of this results, good compromise between robustness and ER is expected to be at the local maxima around 14 $\mu$m.

**The coupling length**   Eq. 6.2 was a useful tool that permitted us to understand what is needed to be done to achieve a short, thus robust PBS; however, this equation does not account for the bends effect; thus it can give us only an approximative value of $L_{PBS}$. To find $L_{PBS}$ precisely, we need to fabricate several short couplers, increasing their coupling length $L$ progressively, and fitting and plotting their obtained splitting ratios as a function of $L$. Such fitting can then be used to predict $L$ at which the two polarisations are in anti-phase; i.e. where a PBS effect is obtained. Such procedure is also represented graphically in
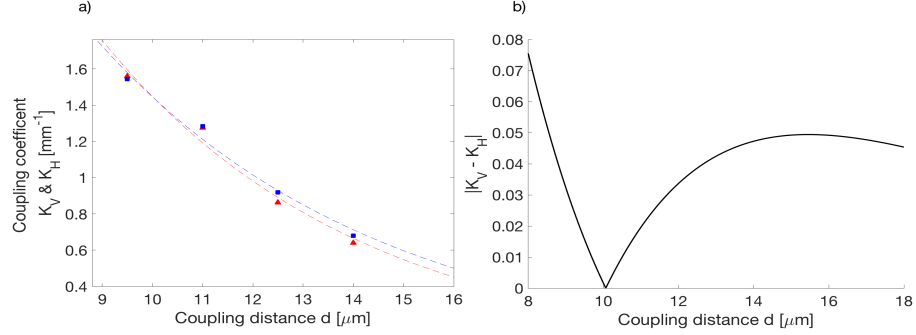
Figure 6.3: Optimising the coupling distance $d$ for the PBS. (a) The vertical (red) and horizontal (blue) coupling coefficients in function of $d$. (b) The absolute value of the difference between the coupling coefficients of the two polarisations obtained from the fitting in (a). The diverging value for small $d$ indicates a small $L_{PBS}$; however, due to waveguides overlap, the coupler would be asymmetrical leading to ER reduction. A good tradeoff between $L_{PBS}$ and ER is guaranteed for bigger $d$ around the local maxima.
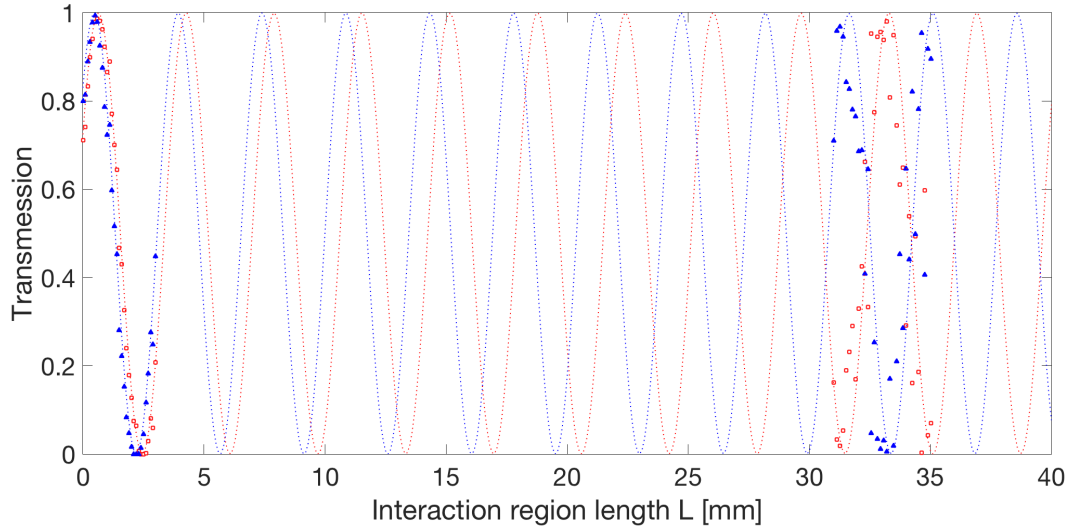


Figure 6.4: Polarisation beam splitters fabrication. H (blue) and V (red) polarisation transmission of the directional coupler with $d = 12.5$ $\mu$m and different coupling lengths. First, the 0-3 mm coupling length range was investigated to evaluate the beating length difference between the two polarisations; the interval of interest to obtain the required PBS was estimated to be somewhere around 33 mm. An exploration of the coupling length range around 33 mm by fabricating couplers in the range 31-35 mm.

Figure 6.4, where several short couplers were fabricated in the 0-3 mm coupling length range. By fitting the experimental data with Eq. 2.11, the interval of interest to obtain the PBS is predicted to be around 33 mm. The procedure in in Figure 6.4 was repeated for $d = 12.5$ $\mu$m and 14 $\mu$m, and for both inscription powers from Table 6.1. $d = 12.5$ $\mu$m gave a slightly shorter $L_{PBS}$ than $d = 14$ $\mu$m. This is not in contradiction with the previous paragraph, indeed considering the experimental data and not the fitting, $|k_H - k_V|$ was bigger for $d = 12.5$ $\mu$m. While by changing the inscription power, we found that 320 mW gave slightly shorter couplers (28 mm) than the 370 mW inscription power (33 mm); nevertheless, it also gave more losses. This is in agreement with our discussion in Section 6.1.3.2. The slightly smaller $L_{PBS}$ with 320 mW did not justify the extra losses, thus, in the end, we chose the combination of $d = 12.5$ $\mu$m and inscription power of 370 mW. The graph in Figure 6.4 refers to these parameters.

#### 6.1.3.4  PBS fabrication

To fabricate the PBSs, we fix all the parameters to the values that were found during the optimisation phase, apart from the coupling region length $L$ which is varied in the range of 31-35 mm around the predicted $L_{PBS} = 33$ mm. Indeed, fixing all the other parameters apart from $L$, the fabrication tolerances will result in a slight $L_{PBS}$ variation. The splitting ratios where plotted over the predicted curve from the short couplers fabrication (Figure 6.4). The experimental data followed the theoretical line, and several PBSs were obtained. The fluctuation of the long coupler around the theoretical line was much bigger than in the case of short couplers, in agreement with our previous argument about the decrease in robustness at longer $L$.

### 6.1.4  Devices characterisation

#### 6.1.4.1  PBS characterisation method

At first, we characterised our PBSs with the V and H polarisations, where V and H were taken in the optical table frame of reference (optical table basis). The biggest obtained ER with such method was 14 dB. In literature, there is only one

demonstration of FLM written PBS, and it is due to Fernandes et al. [68] (see Section 2.4.2). The best-obtained ER in Fernandes's work was 24 dB.

To understand the causes of our reduced ER, we start by assuming that our PBS is an uniaxial birefringent device. In this way, the supermodes of the coupled region should be polarised along the V and H directions, which we call the basis of the PBS. Given the behaviour of this basis on the output, or in other words the splitting ratios, we can recover the splitting ratios of any general polarisation by decomposing it on the PBS basis. The reduced ER can be explained if we also assume that the device basis is rotated with respect to the optical table basis (see Figure 6.5a). This can happen for example if, due to sample holder limitation, we can not perfectly align the vertical and horizontal axes of the elliptical waveguide cross-section, with the axes of the optical table. To understand how such basis rotation may cause ER reduction, we refer to Figure 6.5b which shows what will happen if the V polarisation in the optical table basis is injected in a long coupler. In such long coupler, the polarisation sensitivity is maximised, and the two components of the coupler basis will exit on different ports. The behaviour of the injected polarisation (in black) is easily recovered by decomposing it on the PBS basis (in red), resulting in the presence of a significant component on both outputs of the PBS. To satisfy as much as we can the PBS condition given in Eq. 6.1, the injected light polarisation need to be aligned with one component in the PBS basis, thus achieving the highest ER.

It is worth noting that this argument about the differences between the device and the optical table basis was not an issue in the short couplers. Indeed, as Figure 6.5c shows, in a short coupler the polarisation sensitivity is small, and the two orthogonal components in the device basis (in red) will have almost the same splitting ratios on the device output (Figure 6.5c reports the special case of 100/0 splitting ratio). Thus we will get almost the same splitting ratios as the one obtained by H and V for any arbitrary polarised light that is injected in the device input.

To prove that our assumptions are correct, and as a result, a better ER can be achieved, we need to characterise the PBSs with V and H that are taken in the PBS basis. Finding such PBS basis is easy; using the HWP, it is enough to rotate the polarisation direction of the injected light until we find a minimum in

the measured power on the output port that should suppress that polarisation. Having done this, we need to verify that a further 90° rotation, i.e. the second component in the PBS basis, will also give a minimum on the other output port. This was the case for all our couplers.

Figure 6.6 reports the transmission and reflection for an arbitrary linearly polarised light near the H (0°) and V (90°) components in the PBS basis. Such graph clearly shows an ER degrading when the injected polarisation is not well aligned with the PBS basis. Additionally, this graph also shows a lower ER on the reflection arm; this can be explained due to the presence of residual asymmetry which hinders the splitting ratio on the reflection arm from reaching zero (see Figure 2.3).
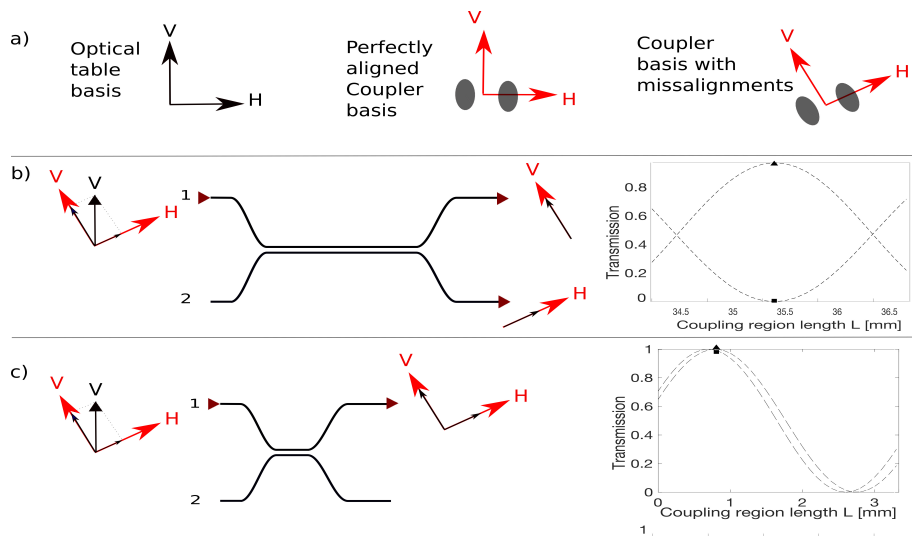


Figure 6.5: (a) The optical table basis (black) and the coupler basis (red). A cross-sectional view of the two coupled waveguides is given. If the sample is well aligned, the optical table basis and the coupler basis coincide. If the sample is misaligned then the two basis are different. (b)/(c) A top-view of a long/short coupler. Such couplers have a big/small polarisation sensitivity; therefore, if, for example, we take a coupler in the point shown in the graph, the two components V and H in the proper coupler basis exit on two different arms/on the same arm. To recover the behaviour of any arbitrary polarised light injected in the coupler input, the injected light must be decomposed onto the coupler basis. In the long coupler, a high ER can be achieved only if the injected light is aligned with one of the two components in the coupler basis.

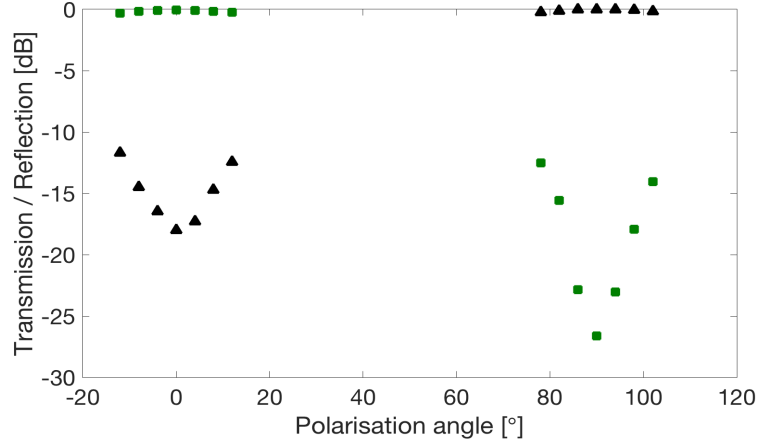Figure 6.6: Characterising the PBS with arbitrary linearly polarised light. Transmission (green squares) and reflection (black triangle) are reported. The 0° and 90° defines the H and V in the coupler basis respectively.

#### 6.1.4.2 ER measurement

Figure 6.7 shows the obtained reflections and transmissions in dB. The best-obtained ER is 17 dB on the reflection port and 26 dB on the transmission port. The transmission port gave a higher ER, which we attributed to the presence of a residual coupler asymmetry, regardless the fact that the chosen $d = 12.5$ $\mu$m gave fully separated waveguides. It is worth mentioning that our results are in agreement with the results of Ref. [68] where ER of 19 dB and 24 dB were obtained on the reflection and transmission port respectively.

A spectral characterisation was also performed on the best performing device and reported in Figure 6.8. While the ER at 1550 nm is 26 dB, it becomes 29 dB at 1553 nm. The ER stays above 20 dB for wavelengths in the range 1545-1560 nm, demonstrating a wide-band behaviour of our PBS devices.

### 6.1.5 Modelling the PBS variability

We have attributed the worse reproducibility in the long couplers with respect to the short ones due to higher sensitivity to $k$ which increases linearly with $L$ (see Eq. 6.4). The coupling coefficient fluctuations are induced mainly by the noise
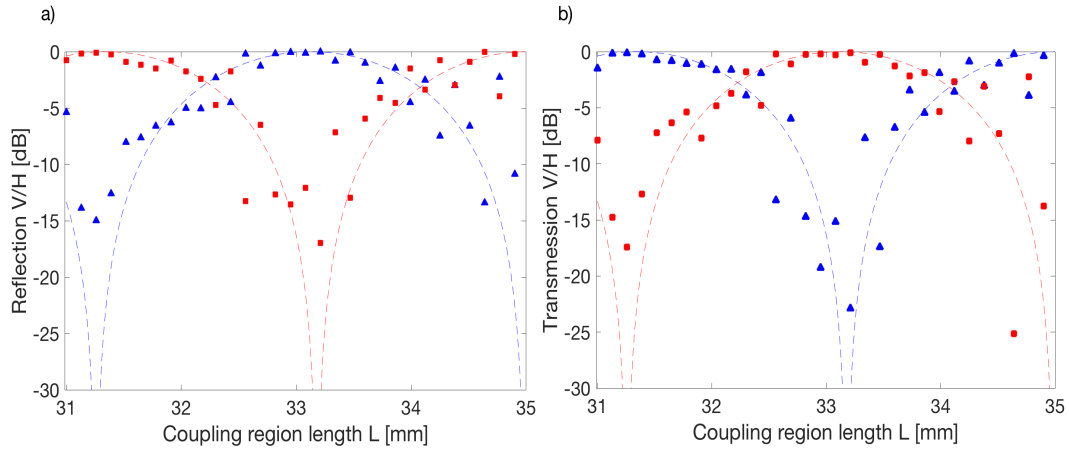
Figure 6.7: Characterisation of the long couplers. The transmission (a) and reflection (b) for V (red) and H (blue) polarisations are shown. The best ER in reflection was 17 dB, while 26 dB in transmission. This can be explained due to the presence of a residual coupler asymmetry intrinsic to the FLM writing process itself.
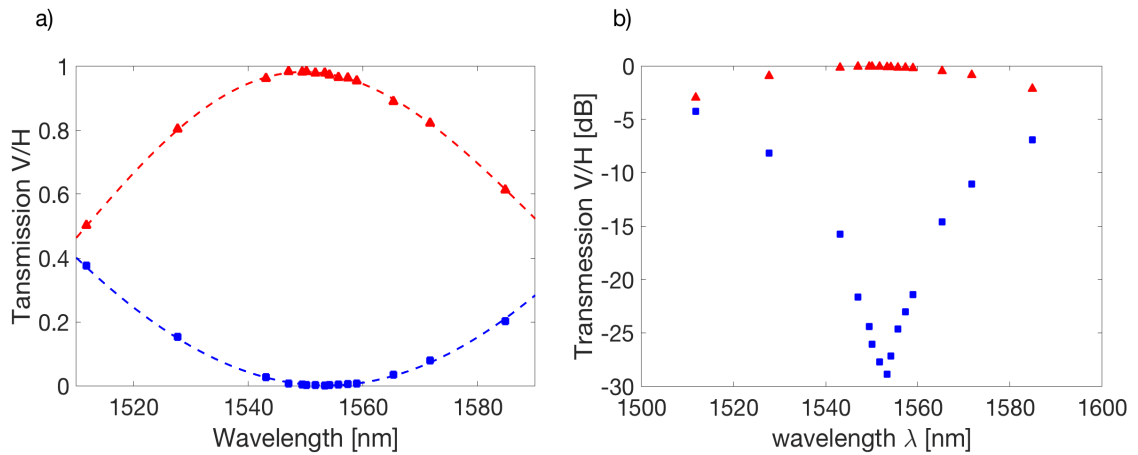


Figure 6.8: A spectral characterisation of the V (red) and H (blue) polarisations in a linear scale (a) and dB (b). The coupler ER was 26 dB at 1550 nm, which became 29 dB at 1553 nm. The ER stayed above 20 dB for wavelengths in the 1545-1560 nm range, demonstrating a wide bandwidth behaviour of our PBS devices.

111

in the laser power, which induces fluctuations in the propagation constant $\beta$. Our objective in this section is to simulate the laser power fluctuations effect on the coupler behaviour, by developing a simulation model based on coupled mode theory. Such model should be interpreted only as a way to get some insight of the noise influence on the splitting ratios, and on possible solutions to mitigate such noise effects.

Laser power fluctuations during waveguide writing may results in different refractive index modification along the waveguide, thus resulting in $\beta$ fluctuations. A laser power fluctuation on a time scale given by t (the autocorrelation time) will be translated in a waveguide $\beta$ fluctuation over a segment of length $\Delta L$. We assume a constant $\beta$ for each segment $\Delta L$, given by a fixed part $\bar{\beta}$, plus a stochastic part $\Delta\beta$. i.e. we divide the waveguide in $N$ segments, each of a length $\Delta L$ and a propagation constant $\beta$ given by:

$$\beta = \bar{\beta} + \Delta\beta_n, \text{ for n = 1, 2,...N} \tag{6.7}$$

FLM written directional couplers consist of two waveguides that are written in a serial manner, thus, assuming a short enough noise correlation time t, the noise distributions in the two waveguides are uncorrelated. We divide the coupler into small double-waveguide segments of length $\Delta L$, and propagation constants $\beta_1$ and $\beta_2$ given by:

$$\beta_1 = \bar{\beta} + \Delta\beta_{n1}, \text{ for n1 = 1, 2,...N}$$
$$\beta_2 = \bar{\beta} + \Delta\beta_{n2}, \text{ for n2 = 1, 2,...N} \tag{6.8}$$

The transmission matrix of two coupled waveguides with $\beta_1$ and $\beta_2$ is given in Eq. 2.5; each segment $\Delta L$ can be described by a transmission matrix $T_{\Delta L}$. The overall coupler transmission matrix is given by cascading the transmission matrixes of all the segments. In such a model, the free parameters are the segment length $\Delta L$; i.e. the time over which the laser power is assumed constant, and the noise model that determines $\Delta\beta_n$. For simplicity, we consider only a noise model in which $\Delta\beta_n$ is taken from a Gaussian distributed with a standard deviation $\sigma_\beta$. To relate $\Delta L$ and $\sigma_\beta$ to the noise spectrum, we use the Wiener-Khinchin theorem (see [77] for example) which tell us that $\Delta L$ determines the noise bandwidth,

while $\sigma_\beta^2$ determines the total noise power.

In Figure 6.9 we report several noise simulations, where the noise bandwidth was kept constant ($\Delta L = 0.1$ mm), but the total noise power was increased progressively by increasing $\sigma_\beta$ which was taken as 0.02, 0.2 and 2 mm$^{-1}$ in panel (a), (b) and (c) of Figure 6.9 respectively. In each graph, we report three simulation runs. The simulation in Figure 6.9b is similar to our experimental results, thus giving a hint that the laser power fluctuations may be the cause for our PBSs poor reproducibility.

With the help of this model, we can propose possible strategies for improving the PBS performance. For example, if using the same fabrication setup we write the two coupled waveguide in a parallel manner by splitting the laser beam in two, then the fluctuations $\Delta\beta_{n1}$ and $\Delta\beta_{n2}$ would be completely correlated. In a first order approximation, we can take $\Delta\beta_{n1}$ equal to $\Delta\beta_{n2}$. If we repeat the worst case simulation from Figure 6.9, i.e. the simulation in Figure 6.9c, but now using $\Delta\beta_{n1} = \Delta\beta_{n2}$, we get the same ideal splitting ratios behaviour for all runs (similar to the one in Figure 6.9a). This shows that parallel waveguide writing may be a valid strategy for noise effect mitigation. The possibility to fabricate optical devices with such parallel writing with femtosecond laser technique was first reported by Pospiech et al. [78].

## 6.2 The polarisation insensitive beam splitter

In this section we deal with the realisation of the second component in BSM-b chip; i.e., the polarisation insensitive Beam Splitter (BS) which is indicated as BS3 in Figure 6.1. The requirements for this component are; to be balanced (50/50) for both the V and H polarisations, to have a mode profile that permits a good coupling with the previous chip (BSM-a chip), while maintaining reasonable losses.

The insensitive BS was also developed for the Mach-Zehnder interferometer in Section 5.1. That beam splitter was based on a 3D geometry originally developed by Sansoni et al. [69]. However, here we will present a new geometry that as we will see in Section 6.2.3 results more advantageous than the 3D geometry.
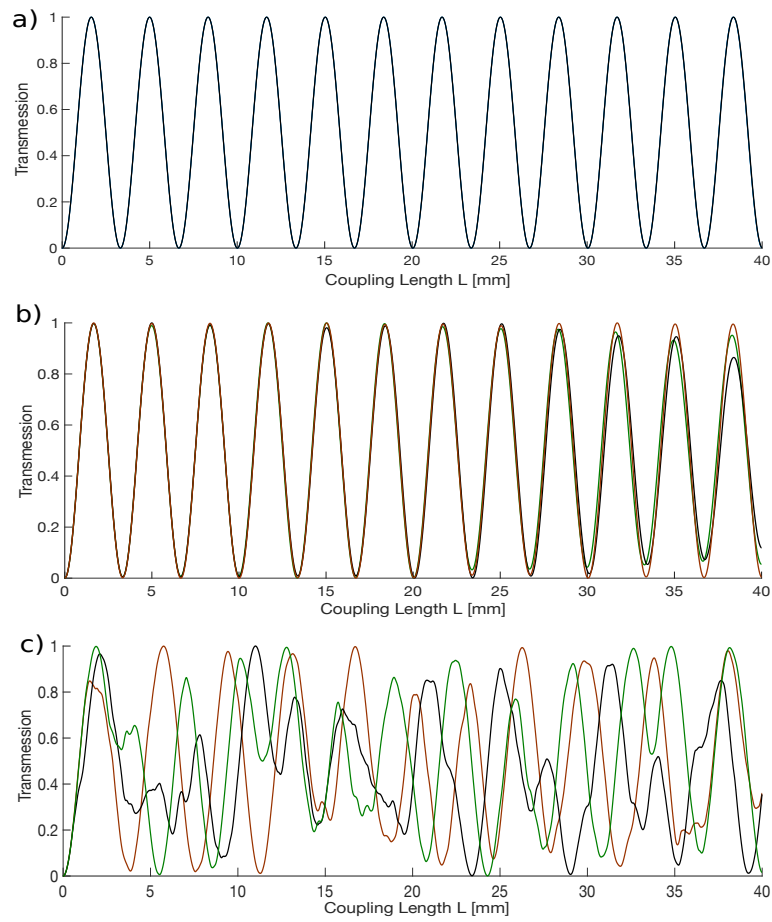
Figure 6.9: PBS noise simulation. Three runs of noise simulations with $d = 12.5$ $\mu$m, $\Delta L = 0.1$ mm. $\sigma_\beta$ is varied from $0.02$ mm$^{-1}$ in (a) to $0.2$ mm$^{-1}$ in (b), and finally $2$ mm$^{-1}$ in (c).

### 6.2.1 The 2D polarisation insensitive beam splitter: the idea

While optimising the PBS coupling distance in Section 6.1.3.3, we have found a sign inversion in the difference between the coupling coefficients of the two orthogonal polarisations $k_H - k_V$ (see Figure 6.3). The idea behind our new polarisation insensitive BS is thus the following: Figure 6.3 shows that $k_H < k_V$ for small $d$, while $k_H > k_V$ for big d; thus, there should be a $d$, which we call $d_{ins}$, for which $k_H = k_V$. In such point, both polarisations behave equally, and polarisation insensitivity is achieved.

In a real coupler, if we work with $d = d_{ins}$, in the coupling region the splitting ratios of the two polarisations will beat with the same period; however they will be shifted one from the other due to the residual coupling that happens in the bends where $k_H \neq k_V$. Nevertheless, a real coupler can still be made polarisation insensitive if we work with $d < d_{ins}$, and choose the right coupling length $L$ that will exactly compensate the bends effect where $d > d_{ins}$. Various combinations of $d$ and $L$ will give such polarisation insensitive effect; however they will differ in the splitting ratios that they achieve at the coupler output. Thus, in our specific case, we need to find the right $d$ and $L$ combination that gives us a 50/50 polarisation insensitive beam splitter. Note that our new idea involves only the proper tailoring of the geometrical parameters in a standard 2D coupler. We call this new coupler the 2D polarisation insensitive BS to distinguish it from the previously realised 3D polarisation insensitive BS.

### 6.2.2 Fabrication details

The polarisation insensitive BS will be integrated into one chip with the two PBSs; thus all three components will be written with the same fabrication parameters given in Table 6.1 (with the 370 mW inscription power). We also use the same S-bend radius of curvature and input/output waveguides separation of 90 mm and 127 $\mu$m respectively. Thus the only parameters that we need to optimise, and that determines a polarisation insensitive BS behaviour rather than PBS behaviour are $d$ and $L$.

The first thing to do is to verify with higher experimental accuracy the

| Examples of experimentally realised polarisation insensitive 50/50 beam splitters | | | |
|---|---|---|---|
| Device | $T_V$ | $T_H$ | $|T_V - T_H|$ |
| 1 | 0.5005 | 0.5007 | 0.0002 |
| 2 | 0.5103 | 0.5102 | 0.0001 |

Table 6.2: Example of two 50/50 polarisation insensitive beam splitters realised with our new 2D approach.

$k_V - k_H$ sign inversion on which our idea is based. For this aim, we investigated coupling distances in the range of 7-9 $\mu$m by steps of 0.5 $\mu$m. The procedure to obtain the coupling coefficients was explained in Section 6.1.3.3. The resulting $k$ are shown in Figure 6.10. Having obtained $k_V$ bigger than $k_H$ for small $d$, we confirm our previous conclusion about the existence of a sign inversion in $k_V - k_H$. The data in Figure 6.10 does not fit well the exponential fitting obtained from the data in Figure 6.3a. This is not surprising since the exponential fitting is valid only under the approximation of two weakly coupled modes which probably is broken for too close waveguides.

To find the right combination of $d$ and $L$ that will give us a balanced polarisation insensitive BS, we need to plot and fit the obtained splitting ratios as a function of $L$ (Figure 6.11). From the fittings, the difference between the transmission of the two polarisations at 50/50 is extracted and reported in the graphs. In particular, we predicted the existence of an excellent balaced polarisation insensitive BS if the combination $d = 8$ $\mu$m and $L = 0.86$ mm is used. This prediction was confirmed by a second fabrication with $d = 8$ $\mu$m and varying $L$ in a small range around 0.86 mm. Table 6.2 reports an example of two polarisation insensitive BS realised with such method, the polarisation sensitivity was almost zero.

## 6.2.3 Discussion

We have developed a new way to fabricate polarisation insensitive couplers with FLM technique. Our new plane couplers are based on the existence of a sign inversion in the quantity $k_V - k_H$ when the coupling distance is changed. Such inversion means that in a real coupler, there should be a $d$ and $L$ combinations for
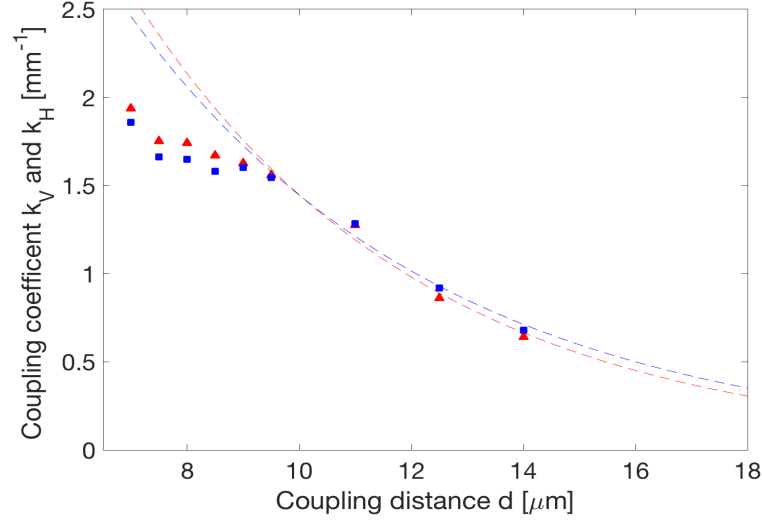
Figure 6.10: The coupling coefficients for the V (red) and H (blue) polarisations in function of the coupling distance $d$. Around $d = 10$ $\mu$m the two polarisations have the same k. For bigger $d$, the H polarisations couple more, while for smaller $d$ the V polarisation couple more. The exponential fitting was done on the experimental data at big $d$ and is valid only under the approximation of weakly coupled Gaussian modes. Such approximation is broken at small $d$.



Figure 6.11: Finding the geometrical parameters $d$ and $L$ for the polarisation insensitive balanced beam splitter. The transmission for V (red) and H (blue) is reported. The data is fitted, and the difference between the transmission of the two polarisations at 50/50 is calculated. The combination $d = 8$ $\mu$m and $L = 0.86$ mm promised the existence of an excellent polarisation insensitive BS.

117

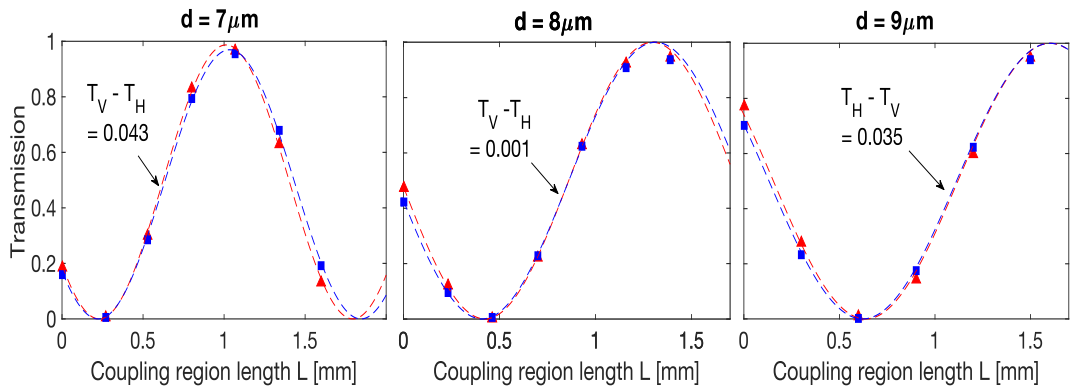which the effective $k$ of the entire structure (bends + coupling region) is the same for the two polarisations; thus a polarisation insensitivity is achieved. This was confirmed experimentally and tailored to our need of 50/50 beam splitter obtaining a remarkable polarisation insensitivity, with difference between the splitting ratios of the V and H polarisations that go down to $10^{-4}$.

**Advantage of the 2D structure**  An interesting advantage of our 2D polarisation insensitive BS over the previously fabricated 3D polarisation insensitive BS is shown in Figure 6.12. This figure shows the polarisation sensitivity of the 2D (black triangles) and 3D (green rectangles) coupler when the injected V and H polarisations are rotated with an angle $\alpha$. We indicate the new rotated linear polarisation with $V'$ and $H'$. The polarisation sensitivity is expressed as the ratio between the splitting ratios of the $V'$ and $H'$ polarisations at the coupler outputs $(T_{V'}/T_{H'})$. The 2D couplers demonstrate a good polarisation insensitive behaviour for any two orthogonal linear polarisations; while the polarisation insensitive of the 3D couplers degrades when the rotated $V'$ and $H'$ states are considered. This is saying that our 2D coupler can be seen as a uniaxial birefringent device, with a V and H components that form the coupler basis, in a similar fashion to what was seen in Figure 6.5a. Generally, the 2D coupler has different splitting ratios for the two orthogonal components in the coupler basis; however, a right $d$ and $L$ combination can force the two components to behave equally at the device output; thus achieving polarisation insensitivity. Since the two components of the basis have the same splitting ratios, any arbitrary polarised light will also give the same splitting ratio; thus polarisation insensitivity is valid for any $V'$ and $H'$. The same can not be said for the 3D polarisation insensitive BS were the behaviour on the output depends on the input state of polarisation.

To explain the origin of the above results, we first discuss Heilmann et al. [70] work which was also presented in Section 2.4.2. In this work, the authors were able to rotate the optical axis of an uniaxial FLM written straight waveguides by fabricating a second adjacent waveguide. In particular, if the two adjacent waveguides are fabricated in the same depth and only the waveguides separation is changes, the optical axis will always stay the same. The optical axis rotation can be achieved when the two waveguides are fabricated in different depths. Such

behaviour was also presented in Figure 2.12a, where instead of fabricating the second waveguide, the authors decided to fabricate a defect line to avoid a light coupling between two adjacent waveguides which was not required in their work. Our 2D polarisation insensitive coupler is constructed from two waveguides that are fabricated at the same depth. Thus it should have only one optical axis, or in other words, the coupler should be an uniaxial birefringence device. In the 3D coupler, on the other hand, the relative depth between the two waveguides changes continuously. Thus, also the optical axis changes continuously along the structure, and the device can not be seen as uniaxial birefringence device.

**Origin of the $k_V - k_H$ sign inversion**   Generally, the coupling coefficients $k_V$ and $k_H$ can be obtained by calculating the overlap integral in function of the distance $d$ using two different mode shapes for the V and H polarisations. However, one could show that this approach can not explain the existence of a sign inversion in the quantity $k_V - k_H$, which can be explained only if the mode shapes change as a function of $d$. Such $d$ dependant mode shapes is probably originated from the fact that the writing of one waveguide will also influence the other, resulting in a $d$ dependant material modification. This is in agreement with Fernandes et al. [79] study, where the writing of one waveguide altered the birefringence of an adjacent waveguide, in particular, the birefringence modification changed as a function of the waveguides separation.

## 6.3   BSM-b chip fabrication

### 6.3.1   Fabrication strategy

Having developed the PBS and the polarisation insensitive BS, we can proceed with BSM-b chip fabrication. The schematic of BSM-b chip is reported in Figure 6.1. One PBS input is connected to the polarisation insensitive BS output, while the second input is not connected to anything; thus permitting an independent access to the PBS device itself which may be useful for the characterisation phase.

In the light of Eq. 6.4, and as our experimental experience demonstrate, the polarisation insensitive BS is much more a repeatable structure than the PBS
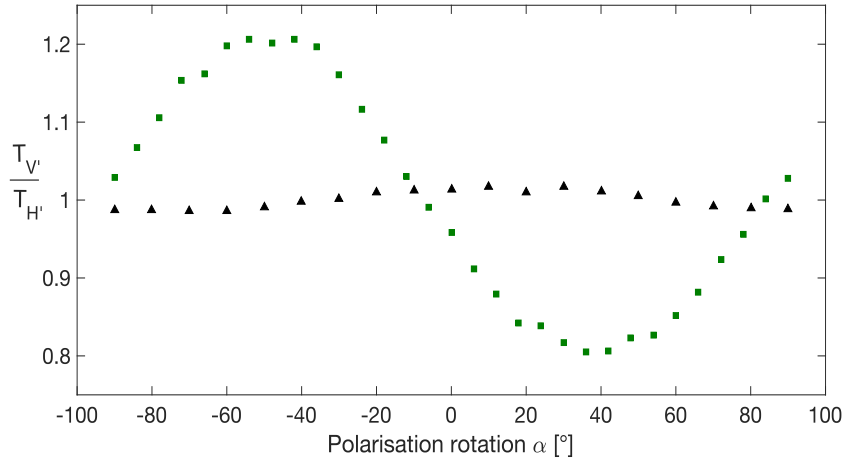
Figure 6.12: Characterisation of the polarisation insensitive couplers with an arbitrary polarised light. Black triangles represent our 2D coupler. Green rectangles represents a coupler that was fabricated in a 3D geometry following Sansoni et al. [69] approach. The 2D coupler presented a superior polarisation insensitivity behaviour when an arbitrary polarised light is concerned.

because it is much shorter (0.86 mm compared with 35 mm). For this reason, we decided to adopt the following fabrication strategy: we use all the fabrication and geometrical parameters that were found in the optimisation process described before, apart from the PBS coupling length $L$, which is varied around the previously found $L_{PBS}$. i.e. we adopted the latter as a single fabrication parameter to compensate for the tolerances of the fabrication process. The polarisation insensitive BS, on the other hand, is not affected much by the fabrication tolerances; thus it does not require a similar treatment.

Using this approach, 30 devices were fabricated scanning the $L$ range of $32 - 34$ mm (centred around the previously found $L_{PBS} = 33$ mm). Their characterisation and the obtained results are given in the next section.

## 6.3.2 Devices characterisation and results

Referring to Figure 6.1, we can see that each PBS can be characterised separately by injecting light into its independent input; i.e. IN1 and IN4 for PBS1 and PBS2 respectively. The PBSs are characterised in their proper bases system as

| Examples of experimental realisations of BSM-b chip | | | | | | | | | | |
|---|---|---|---|---|---|---|---|---|---|---|
| | PBS1 | | | PBS2 | | | BS3 | | | |
| realisation | | | | | | | IN2 | | IN3 | |
| | $ER_T$ | $ER_R$ | $T_V/R_H$ | $ER_T$ | $ER_R$ | $T_V/R_H$ | $T_V/T_H$ | $\lvert T_V - T_H \rvert$ | $T_V/T_H$ | $\lvert T_V - T_H \rvert$ |
| 1 | 13 | 15 | 0.97/0.95 | 27 | 9 | 0.86/1.00 | 0.49/0.50 | 0.0115 | 0.51/0.50 | 0.0034 |
| 2 | 13 | 16 | 0.97/0.95 | 19 | 12 | 0.94/0.99 | 0.50/0.50 | 0.0003 | 0.50/0.49 | 0.0049 |
| 3 | 17 | 12 | 0.93/0.98 | 13 | 15 | 0.97/0.95 | 0.48/0.48 | 0.0014 | 0.49/0.51 | 0.0235 |

Table 6.3: Characterisation of three BSM-b chip realisations that were considered acceptable.

mentioned in Section 6.1.4.1. It is important to verify that the two PBSs have the same polarisation basis, so the maximum potential of both PBSs can be exploited simultaneously. This was the case for all the fabricated devices. To characterise the polarisation insensitive BS, it is enough to inject the V and H polarisations in IN2 and IN3 and observe all the four outputs.

Out of 30 fabricated replicas, the characterisations of the three best performing chips are reported in Table 6.3. It is worth mentioning that while almost all the polarisation insensitive BS were performing fine, the probability of having two good PBSs in the same chip was small due to fabrication tolerances and its effect on the PBS. The devices in Table 6.3 were chosen because they yield an averagely good behaviour for the two PBSs conjunctively.

## 6.4 Quantum teleportation experiment with non-ideal BSM-b chip

In a similar fashion to what was done with the state preparation chip (Section 5.3), in this section, we consider the PBS and the polarisation insensitive BS non-idealities and try to predict their effect on the quantum teleportation fidelity. In particular, we try to predict the fidelities of the three best performing chips that were reported in Table 6.3. The polarisation insensitive BS separates the four Bell-like states by sending two Bell-like states to PBS1, and another two to PBS2. Thus, two Bell-like states pass in each PBS, whose job is to further separate them by sending one Bell-like state on each PBS output. From this discussion, it is rather clear that the non-idealities of the polarisation insensitive BS and the PBSs can be considered separately by calculating the corresponding

fidelities. The overall fidelity can then be obtained by a simple multiplication.

We start by considering an ideal polarisation insensitive BS but non-ideal PBS. As described in Section 4.2.2, two ideal PBSs (ER $= \infty$) would separate completely the four Bell-like states; i.e. there is a univocal correspondence between the single-photons detector clicks and the projection onto Bell-like states. Following this description, the effect of the non-ideal PBS is rather obvious, each click on the single-photon detectors PD$_1$ to PD$_4$ will give a certain probability of Bell-state detection given by the PBS splitting ratio. Thus, the teleportation fidelity due to non-ideal PBS can be directly obtained from the PBS splitting ratios. For instance, PBS1 in realisation 1 from Table 6.3 had $T_V/R_H = 0.97/0.95$, and since this PBS separates the $|\Psi^-\rangle_{AS}$ and $|\Phi^-\rangle_{AS}$ (Eq. 4.18), then considering only the PBS non-ideality, the teleportation fidelities for $|\Psi^-\rangle_{AS}$ and $|\Phi^-\rangle_{AS}$ are reduced to 0.97 and 0.95 respectively.

To understand the effect of the polarisation insensitive BS non-idealities on the experiment, we can consider an ideal PBS, but non-ideal polarisation insensitive BS. An ideal polarisation insensitive BS would send the $|\Psi^-\rangle_{AS}$ and $|\Phi^-\rangle_{AS}$ to PBS1, while $|\Psi^+\rangle_{AS}$ and $|\Phi^+\rangle_{AS}$ to PBS2. If instead a non-ideal polarisation insensitive BS is used, it will send each Bell-like state to both PBSs. To calculate the effect on the teleportation fidelities, we need to repeat the calculation in Eq. 4.15 with two (one for each polarisation) non-ideal transmission matrixes for the polarisation insensitive BS (BS3). By propagating the Bell-like states using these matrixes in an analogue manner to what was done in Eq. 4.15, at each output, we will obtain a certain probability amplitude of having a certain Bell-like state, the square of which represent the teleportation fidelity.

The overall fidelities due to non-ideal BSM-b chip can be obtained by multiplying the fidelities that we calculated for the non-ideal PBS and the non-ideal polarisation insensitive BS separately. Table 6.4 reports the fidelities for all three realisations that were given in Table 6.3.

| Quantum teleportation fidelities due to non-ideal BSM-b chip | | |
|---|---|---|
| **BSM result** | **BSM-b chip realisation** | |
| | 1 | 2 | 3 |
| $\left|\Psi^{-}\right\rangle_{AS}$ | 0.970 | 0.951 | 0.988 |
| $\left|\Phi^{-}\right\rangle_{AS}$ | 0.969 | 0.960 | 0.961 |
| $\left|\Psi^{+}\right\rangle_{AS}$ | 0.980 | 0.999 | 0.941 |
| $\left|\Phi^{-}\right\rangle_{AS}$ | 0.877 | 0.952 | 0.940 |

Table 6.4: Teleportation fidelities due to non-ideal components for the three BSM-b chip realisations given in Table 6.3.

# Conclusions

The aim of this work was to develop the integrated optical components for on-chip quantum teleportation module that works at the telecom wavelength. The module was divided into two main parts: the first part is the state preparation chip where an arbitrary path-encoded qubit is prepared. This qubit is then passed to a second part of the module which represents the sender, Alice, who needs to perform a Bell-State Measurement (BSM). The division of our module in two parts has highlighted the fact that, as quantum teleportation protocol dictates, the sender does not have to know the state of the qubit that he is sending.

The state preparation chip was realised with a thermally controlled Mach-Zehnder Interferometer (MZI). We built the MZI from two polarisation insensitive 3D couplers, thus allowing to prepare the same path-encoded qubit regardless of the photon polarisation. Nevertheless, a small polarisation dependency was still present; however, by considering such polarisation dependency, In the worst, the teleportation fidelity was reduced from the ideal value of 1, down to the still very high value of 0.99.

We developed a femtosecond laser written polarising beam splitter that works in the telecom wavelength. Our PBSs achieved extinction ratios up to 30 dB, and wide bandwidth behaviour with ER above 20 dB for $\Delta\lambda = 15$ nm. We tried to increase the PBS robustness to the fabrication tolerances by minimising its coupling length $L$. This was achieved by finding the right coupling distance $d$ that gives the biggest difference in the coupling coefficients between the two polarisations, but without causing ER reduction due to waveguide overlap that will cause coupler asymmetry. A simulation of the fabrication noise effect on the PBS was performed and gave an insight into possible ways to improve the PBS variability.

In addition, we developed a new way to obtain a polarisation insensitive beam splitters by exploiting the sign inversion in the difference between the vertical and horizontal coupling coefficients in a 2D geometry. Using this method, we fabricated balance polarisation insensitive beam splitters, with equal splitting ratios between the two polarisations down to $10^{-4}$. Such 2D couplers have also demonstrated polarisation insensitivity for any arbitrary polarisation injected in the device.

We finally combined the polarisation insensitive beam splitter with two PBS, to form part of the chip that would perform the BSM needed for the teleportation protocol. Here, fabrication tolerances make it hard to obtain top performances for the three components in the same chip. Therefore, we modelled the effect of the non-ideality of this chip for the sake of teleportation fidelity, and we discovered that the PBS is a critical component for the quantum experiment.

Future development would be to complete the Bell-State measurement chip by developing and fabricating an integrated half waveplate in the telecom wavelength. Such waveplates can be fabricated by following Corrielli et al. [71] approach, where the optical axis of the straight waveguides was tilted by tilting the inscribing laser beam. Once the Bell-State measurement chip is completed, the quantum teleportation experiment can then be implemented aiming for a demonstration of the quantum teleportation potentiality as a future quantum communication protocol.

# References

[1] Charles H Bennett, Gilles Brassard, Claude Crépeau, Richard Jozsa, Asher Peres, and William K Wootters. Teleporting an unknown quantum state via dual classical and einstein-podolsky-rosen channels. *Physical review letters*, 70(13):1895, 1993. v, 1, 11, 13, 17

[2] Stefano Pirandola, Jens Eisert, Christian Weedbrook, Akira Furusawa, and Samuel L Braunstein. Advances in quantum teleportation. *Nature photonics*, 9(10):641–652, 2015. v, 1

[3] R. P. Feynman. *The Feynman lectures on physics*. Addison–Wesley, 1964. 4

[4] Albert Einstein, Boris Podolsky, and Nathan Rosen. Can quantum-mechanical description of physical reality be considered complete? *Physical review*, 47(10):777, 1935. 6

[5] Anton Zeilinger, Herbert J Bernstein, and Michael A Horne. Information transfer with two-state two-particle quantum systems. *Journal of Modern Optics*, 41(12):2375–2384, 1994. 8

[6] John S Bell. On the einstein podolsky rosen paradox, 1964. 8

[7] Richard P Feynman. Simulating physics with computers. *International journal of theoretical physics*, 21(6):467–488, 1982. 10

[8] N David Mermin. *Quantum computer science: an introduction*. Cambridge University Press, 2007. 10

[9] Peter W Shor. Polynomial-time algorithms for prime factorization and discrete logarithms on a quantum computer. *SIAM review*, 41(2):303–332, 1999. 10

[10] Lov K Grover. Quantum mechanics helps in searching for a needle in a haystack. *Physical review letters*, 79(2):325, 1997. 10

[11] Nicolas Gisin, Grégoire Ribordy, Wolfgang Tittel, and Hugo Zbinden. Quantum cryptography. *Reviews of modern physics*, 74(1):145, 2002. 11

[12] Charles H Bennett. Quantum cryptography: Public key distribution and coin tossing. In *International Conference on Computer System and Signal Processing, IEEE, 1984*, pages 175–179, 1984. 11

[13] H Jeff Kimble. The quantum internet. *Nature*, 453(7198):1023–1030, 2008. 11

[14] David Kielpinski, Chris Monroe, and David J Wineland. Architecture for a large-scale ion-trap quantum computer. *Nature*, 417(6890):709–711, 2002. 11

[15] Mark Fox. *Quantum optics: an introduction*, volume 15. OUP Oxford, 2006. 11, 13, 14

[16] Dik Bouwmeester, Jian-Wei Pan, Klaus Mattle, Manfred Eibl, Harald Weinfurter, and Anton Zeilinger. Experimental quantum teleportation. *Nature*, 390(6660):575–579, 1997. 18, 20, 21, 79

[17] Sandu Popescu. An optical method for teleportation. URL http://lanl.arxiv.org/abs/quant-ph/9501020. 18, 22

[18] Danilo Boschi, Salvatore Branca, Francesco De Martini, Lucien Hardy, and Sandu Popescu. Experimental realization of teleporting an unknown pure quantum state via dual classical and einstein-podolsky-rosen channels. *Physical Review Letters*, 80(6):1121, 1998. 18, 22, 80

[19] D. Bouwmeester, A.K. Ekert, and A. Zeilinger. *The Physics of Quantum Information: Quantum Cryptography, Quantum Teleportation, Quantum Computation.* Springer Berlin Heidelberg, 2013. ISBN 9783662042090. URL https://books.google.it/books?id=Qu7wCAAAQBAJ. 23

[20] CK Hong, ZY Ou, and Leonard Mandel. Measurement of subpicosecond time intervals between two photons by interference. *Physical Review Letters*, 59(18):2044, 1987. 26

[21] Sébastien Tanzilli, Hugues De Riedmatten, Hugo Zbinden, Paolo Baldi, M De Micheli, DB Ostrowsky, Nicolas Gisin, et al. Highly efficient photon-pair source using periodically poled lithium niobate waveguide. *Electronics Letters*, 37(1):26–28, 2001. 27

[22] Xavier Fernandez-Gonzalvo, Giacomo Corrielli, Boris Albrecht, Marcel li Grimau, Matteo Cristiani, and Hugues de Riedmatten. Quantum frequency conversion of quantum memory compatible photons to telecommunication wavelengths. *Optics express*, 21(17):19473–19487, 2013. 27

[23] Alberto Politi, Martin J Cryan, John G Rarity, Siyuan Yu, and Jeremy L O'Brien. Silica-on-silicon waveguide quantum circuits. *Science*, 320(5876): 646–649, 2008. 27

[24] Jeremy O'Brien, Brian Patton, Masahide Sasaki, and Jelena Vučković. Focus on integrated quantum optics. *New Journal of Physics*, 15(3):035016, 2013. 27

[25] Brian J Smith, Dmytro Kundys, Nicholas Thomas-Peter, PGR Smith, and IA Walmsley. Phase-controlled integrated photonic quantum circuits. *Optics Express*, 17(16):13516–13525, 2009. 27

[26] Benjamin J Metcalf, Justin B Spring, Peter C Humphreys, Nicholas Thomas-Peter, Marco Barbieri, W Steven Kolthammer, Xian-Min Jin, Nathan K Langford, Dmytro Kundys, James C Gates, et al. Quantum teleportation on a photonic chip. *Nature Photonics*, 8(10):770–774, 2014. 27, 68

[27] Serge Massar and Sandu Popescu. Optimal extraction of information from finite quantum ensembles. *Physical review letters*, 74(8):1259, 1995. 27, 80

[28] Stewart E. Miller. Integrated optics: An introduction. *Bell System Technical Journal*, 48(7):2059–2069, 1969. ISSN 1538-7305. doi: 10.1002/j.1538-7305. 1969.tb01165.x. URL http://dx.doi.org/10.1002/j.1538-7305.1969. tb01165.x. 28

[29] H Kogelnik and T Tamir. Guided-wave optoelectronics. *Springer, Berlin*, page 7, 1990. 32

[30] Jörg Hübner, S Guldberg-Kjaer, M Dyngaard, Y Shen, CL Thomsen, S Balslev, C Jensen, D Zauner, and Thomas Feuchter. Planar er-and yb-doped amplifiers and lasers. *Applied Physics B*, 73(5-6):435–438, 2001. 38

[31] A. Ogura. Method of fabricating soi substrate, March 30 1999. URL https: //www.google.com/patents/US5888297. US Patent 5,888,297. 39

[32] Giovanni Gilardi and Meint K Smit. Generic inp-based integration technology: Present and prospects (invited review). *Progress In Electromagnetics Research*, 147:23–35, 2014. 39

[33] Meint Smit, Xaveer Leijtens, Huub Ambrosius, Erwin Bente, Jos Van der Tol, Barry Smalbrugge, Tjibbe De Vries, Erik-Jan Geluk, Jeroen Bolk, Rene Van Veldhoven, et al. An introduction to inp-based generic integration technology. *Semiconductor Science and Technology*, 29(8):083001, 2014. 39

[34] M Svalgaard, CV Poulsen, A Bjarklev, and Ole Poulsen. Direct uv writing of buried singlemode channel waveguides in ge-doped silica films. *Electronics Letters*, 30(17):1401–1403, 1994. 40

[35] D Du, X Liu, G Korn, J Squier, and G Mourou. Laser-induced breakdown by impact ionization in sio2 with pulse widths from 7 ns to 150 fs. *Applied physics letters*, 64(23):3071–3073, 1994. 40, 43

[36] PP Pronko, SK Dutta, J Squier, JV Rudd, D Du, and G Mourou. Machining of sub-micron holes using a femtosecond laser at 800 nm. *Optics communications*, 114(1):106–110, 1995. 40

[37] K Miura Davis, K Miura, Naoki Sugimoto, and Kazuyuki Hirao. Writing waveguides in glass with a femtosecond laser. *Optics letters*, 21(21):1729–1731, 1996. 40, 47

[38] B C Stuart, M D Feit, S Herman, AM Rubenchik, BW Shore, and MD Perry. Nanosecond-to-femtosecond laser-induced breakdown in dielectrics. *Physical Review B*, 53(4):1749, 1996. 41

[39] Roberto Osellame, Giulio Cerullo, and Roberta Ramponi. *Femtosecond Laser Micromachining: Photonic and Microfluidic Devices in Transparent Materials*, volume 123. Springer Science &amp; Business Media, 2012. 42

[40] Chris B Schaffer, Andre Brodeur, and Eric Mazur. Laser-induced breakdown and damage in bulk transparent materials induced by tightly focused femtosecond laser pulses. *Measurement Science and Technology*, 12(11):1784, 2001. 42, 44

[41] Kazuyoshi Itoh, Wataru Watanabe, Stefan Nolte, and Chris B Schaffer. Ultrafast processes for bulk modification of transparent materials. *MRS bulletin*, 31(08):620–625, 2006. 43

[42] EN Glezer, M Milosavljevic, L Huang, RJ Finlay, T-H Her, J Paul Callan, and Eric Mazur. Three-dimensional optical storage inside transparent materials. *Optics Letters*, 21(24):2023–2025, 1996. 43

[43] S Juodkazis, S Matsuo, H Misawa, V Mizeikis, A Marcinkevicius, H-B Sun, Y Tokuda, M Takahashi, T Yoko, and J Nishii. Application of femtosecond laser pulses for microfabrication of transparent media. *Applied surface science*, 197:705–709, 2002. 43

[44] Chris B Schaffer, André Brodeur, José F García, and Eric Mazur. Micromachining bulk glass by use of femtosecond laser pulses with nanojoule energy. *Optics letters*, 26(2):93–95, 2001. 43, 46

[45] Alexander M Streltsov and Nicholas F Borrelli. Study of femtosecond-laser-written waveguides in glasses. *JOSA B*, 19(10):2496–2504, 2002. 43

[46] T Toney Fernandez, P Haro-González, B Sotillo, M Hernandez, Daniel Jaque, P Fernandez, Concepción Domingo, Jan Siegel, and J Solis. Ion migration assisted inscription of high refractive index contrast waveguides by femtosecond laser pulses in phosphate glass. *Optics letters*, 38(24):5248–5251, 2013. 43

[47] Masaaki Sakakura, Masahiro Shimizu, Yasuhiko Shimotsuma, Kiyotaka Miura, and Kazuyuki Hirao. Temperature distribution and modification mechanism inside glass with heat accumulation during 250khz irradiation of femtosecond laser pulses. *Applied Physics Letters*, 93(23):231112, 2008. 43

[48] A Marcinkevičius, V Mizeikis, S Juodkazis, S Matsuo, and H Misawa. Effect of refractive index-mismatch on laser microfabrication in silica glass. *Applied Physics A*, 76(2):257–260, 2003. 44

[49] Cyril Mauclair, Alexandre Mermillod-Blondin, Nicolas Huot, Eric Audouard, and Razvan Stoian. Ultrafast laser writing of homogeneous longitudinal waveguides in glasses using dynamic wavefront correction. *Optics express*, 16(8):5481–5492, 2008. 45

[50] G Cerullo, R Osellame, S Taccheo, M Marangoni, D Polli, R Ramponi, P Laporta, and S De Silvestri. Femtosecond micromachining of symmetric waveguides at 1.5 $\mu$m by astigmatic beam focusing. *Optics letters*, 27 (21):1938–1940, 2002. 45

[51] Wataru Watanabe, Yumiko Note, and Kazuyoshi Itoh. Fabrication of multimode interference waveguides in glass by use of a femtosecond laser. *Optics letters*, 30(21):2888–2890, 2005. 45

[52] Petra Paie. *Femtosecond laser micromachining of optofluidics glass chips for biophotonic applications.* PhD thesis, Italy, 2016. 45

[53] Shane M Eaton, Haibin Zhang, Mi Li Ng, Jianzhao Li, Wei-Jen Chen, Stephen Ho, and Peter R Herman. Transition from thermal diffusion to heat accumulation in high repetition rate femtosecond laser writing of buried optical waveguides. *Optics express*, 16(13):9443–9458, 2008. 46, 47

[54] Shane Eaton, Haibin Zhang, Peter Herman, Fumiyo Yoshino, Lawrence Shah, James Bovatsek, and Alan Arai. Heat accumulation effects in femtosecond laser-written waveguides with variable repetition rate. *Optics Express*, 13 (12):4708–4716, 2005. 46

[55] Chris B Schaffer, José F García, and Eric Mazur. Bulk heating of transparent materials using a high-repetition-rate femtosecond laser. *Applied Physics A*, 76(3):351–354, 2003. 46

[56] SM Eaton, H Zhang, ML Ng, S Ho, and PR Herman. Optimization of repetition rate, pulse duration, and polarization for femtosecond-laser-writing of waveguides in borosilicate and fused silica glasses. In *2007 European Conference on Lasers and Electro-Optics and the International Quantum Electronics Conference*, 2007. 47

[57] Weijia Yang, Peter G Kazansky, Yasuhiko Shimotsuma, Masaaki Sakakura, Kiyotaka Miura, and Kazuyuki Hirao. Ultrashort-pulse laser calligraphy. *Applied Physics Letters*, 93(17):171109, 2008. 47

[58] Alexander M Streltsov and Nicholas F Borrelli. Fabrication and analysis of a directional coupler written in glass by nanojoule femtosecond laser pulses. *Optics Letters*, 26(1):42–43, 2001. 47

[59] R Osellame, V Maselli, N Chiodo, D Polli, R Martinez Vazquez, R Ramponi, and G Cerullo. Fabrication of 3d photonic devices at 1.55 $\mu$m wavelength by femtosecond ti: Sapphire oscillator. *Electronics Letters*, 41(6):1, 2005. 47, 48

[60] Kenya Suzuki, Vikas Sharma, James G Fujimoto, Erich P Ippen, and Yusuke Nasu. Characterization of symmetric [3× 3] directional couplers fabricated by direct writing with a femtosecond laser oscillator. *Optics express*, 14(6): 2335–2343, 2006. 47, 48

[61] Shame M Eaton, W Chen, L Zhang, H Zhang, R Iyer, JS Aitchison, and PR Herman. Telecom-band directional coupler written with femtosecond fiber laser. *IEEE photonics technology letters*, 18(17-20):2174–2176, 2006. 48

[62] Kaoru Minoshima, Andrew Kowalevicz, Erich Ippen, and James Fujimoto. Fabrication of coupled mode photonic devices in glass by nonlinear femtosecond laser materials processing. *Optics Express*, 10(15):645–652, 2002. 48, 50

[63] Guangyu Li, Kim A Winick, Ali A Said, Mark Dugan, and Philippe Bado. Waveguide electro-optic modulator in fused silica fabricated by femtosecond laser direct writing and thermal poling. *Optics letters*, 31(6):739–741, 2006. 49, 50

[64] Fulvio Flamini, Lorenzo Magrini, Adil S Rab, Nicolò Spagnolo, Vincenzo D'Ambrosio, Paolo Mataloni, Fabio Sciarrino, Tommaso Zandrini, Andrea Crespi, Roberta Ramponi, et al. Thermally-reconfigurable quantum photonic circuits at telecom wavelength by femtosecond laser micromachining. *arXiv preprint arXiv:1512.04330*, 2015. 49, 50, 83

[65] VR Bhardwaj, PB Corkum, DM Rayner, C Hnatovsky, E Simova, and RS Taylor. Stress in femtosecond-laser-written waveguides in fused silica. *Optics letters*, 29(12):1312–1314, 2004. 51

[66] Andrea Crespi, Roberta Ramponi, Roberto Osellame, Linda Sansoni, Irene Bongioanni, Fabio Sciarrino, Giuseppe Vallone, and Paolo Mataloni. Integrated photonic quantum gates for polarization qubits. *Nature communications*, 2:566, 2011. 51, 54

[67] RS Taylor, C Hnatovsky, E Simova, PP Rajeev, DM Rayner, and PB Corkum. Femtosecond laser erasing and rewriting of self-organized planar nanocracks in fused silica glass. *Optics letters*, 32(19):2888–2890, 2007. 52

[68] Luís A Fernandes, Jason R Grenier, Peter R Herman, J Stewart Aitchison, and Paulo VS Marques. Femtosecond laser fabrication of birefringent directional couplers as polarization beam splitters in fused silica. *Optics express*, 19(13):11992–11999, 2011. 52, 54, 108, 110

[69] Linda Sansoni, Fabio Sciarrino, Giuseppe Vallone, Paolo Mataloni, Andrea Crespi, Roberta Ramponi, and Roberto Osellame. Two-particle bosonic-

fermionic quantum walk via integrated photonics. *Physical review letters*, 108(1):010502, 2012. 52, 54, 84, 113, 120

[70] René Heilmann, Markus Gräfe, Stefan Nolte, and Alexander Szameit. Arbitrary photonic wave plate operations on chip: Realizing hadamard, pauli-x, and rotation gates for polarisation qubits. *Scientific reports*, 4, 2014. 52, 55, 118

[71] Giacomo Corrielli, Andrea Crespi, Riccardo Geremia, Roberta Ramponi, Linda Sansoni, Andrea Santinelli, Paolo Mataloni, Fabio Sciarrino, and Roberto Osellame. Rotated waveplates in integrated waveguide optics. *Nature communications*, 5, 2014. 53, 55, 98, 125

[72] Alexander Killi, Andy Steinmann, Jochen Dörring, Uwe Morgner, Max J. Lederer, Daniel Kopf, and Carsten Fallnich. High-peak-power pulses from a cavity-dumped yb:ky(wo4)2 oscillator. *Opt. Lett.*, 30(14):1891–1893, Jul 2005. doi: 10.1364/OL.30.001891. URL http://ol.osa.org/abstract.cfm?URI=ol-30-14-1891. 56, 58

[73] GIACOMO CORRIELLI. *Integrated photonic circuits by femtosecond laser writing for qubit manipulation, quantum cryptography and quantum-optical analogies*. PhD thesis, Italy, 2015. 57, 60, 62, 65

[74] Daniele Melati, Andrea Melloni, and Francesco Morichetti. Real photonic waveguides: guiding light through imperfections. *Advances in Optics and Photonics*, 6(2):156–224, 2014. 63

[75] D Gloge. Bending loss in multimode fibers with graded and ungraded core index. *Applied optics*, 11(11):2506–2513, 1972. 64

[76] Andrea Crespi, Roberto Osellame, Roberta Ramponi, Daniel J Brod, Ernesto F Galvao, Nicolò Spagnolo, Chiara Vitelli, Enrico Maiorino, Paolo Mataloni, and Fabio Sciarrino. Integrated multimode interferometers with arbitrary designs for photonic boson sampling. *Nature Photonics*, 7(7):545–549, 2013. 101

[77] S. Engelberg. *Random Signals and Noise: A Mathematical Introduction.* Taylor &amp; Francis, 2006. ISBN 9780849375545. 112

[78] Matthias Pospiech, Moritz Emons, Andy Steinmann, Guido Palmer, Roberto Osellame, Nicola Bellini, Giulio Cerullo, and Uwe Morgner. Double waveguide couplers produced by simultaneous femtosecond writing. *Optics express*, 17(5):3555–3563, 2009. 113

[79] Luís A Fernandes, Jason R Grenier, Peter R Herman, J Stewart Aitchison, and Paulo VS Marques. Femtosecond laser writing of waveguide retarders in fused silica for polarization control in optical circuits. *Optics express*, 19 (19):18294–18301, 2011. 119